

# Integrating optics and microfluidics to automatically identify algae species

**Citation for published version (APA):**

Schaap, A. M. (2015). *Integrating optics and microfluidics to automatically identify algae species*. [Phd Thesis 1 (Research TU/e / Graduation TU/e), Mechanical Engineering]. Technische Universiteit Eindhoven.

**Document status and date:**

Published: 01/01/2015

**Document Version:**

Publisher's PDF, also known as Version of Record (includes final page, issue and volume numbers)

**Please check the document version of this publication:**

- A submitted manuscript is the version of the article upon submission and before peer-review. There can be important differences between the submitted version and the official published version of record. People interested in the research are advised to contact the author for the final version of the publication, or visit the DOI to the publisher's website.
- The final author version and the galley proof are versions of the publication after peer review.
- The final published version features the final layout of the paper including the volume, issue and page numbers.

[Link to publication](#)

**General rights**

Copyright and moral rights for the publications made accessible in the public portal are retained by the authors and/or other copyright owners and it is a condition of accessing publications that users recognise and abide by the legal requirements associated with these rights.

- Users may download and print one copy of any publication from the public portal for the purpose of private study or research.
- You may not further distribute the material or use it for any profit-making activity or commercial gain
- You may freely distribute the URL identifying the publication in the public portal.

If the publication is distributed under the terms of Article 25fa of the Dutch Copyright Act, indicated by the "Taverne" license above, please follow below link for the End User Agreement:

[www.tue.nl/taverne](http://www.tue.nl/taverne)

**Take down policy**

If you believe that this document breaches copyright please contact us at:

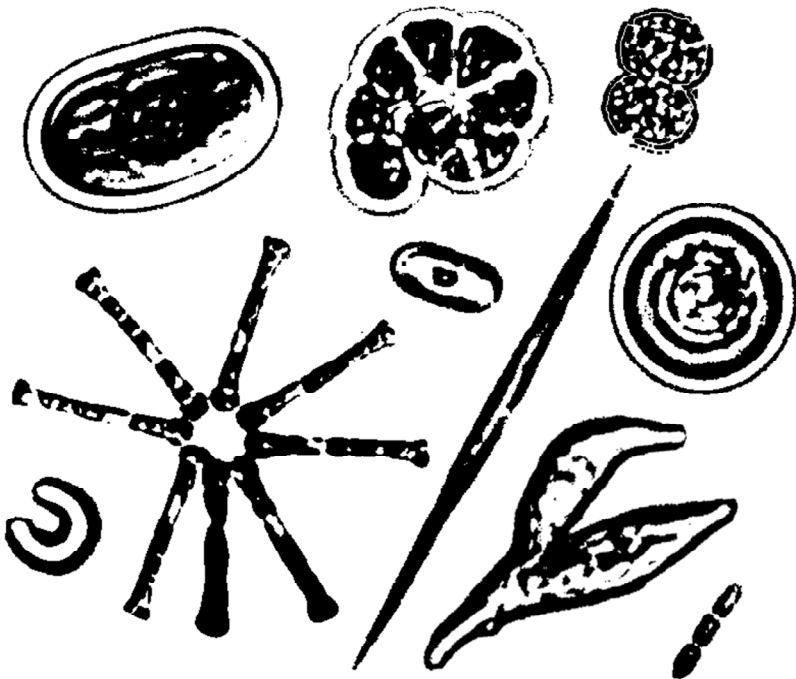
[openaccess@tue.nl](mailto:openaccess@tue.nl)

providing details and we will investigate your claim.



Integrating optics & microfluidics  
to automatically identify algae species

Integrating optics and microfluidics  
to automatically identify algae species



Integrating optics and microfluidics to automatically identify algae species

Copyright © 2015 Allison Schaap

Technische Universiteit Eindhoven

A catalogue record is available from the Eindhoven University of Technology Library

ISBN: 978-90-386-3841-6

Printed by: Ipskamp Drukkers, Enschede, The Netherlands

This research has been financially supported by the Department of Mechanical Engineering at the Eindhoven University of Technology and by the 7<sup>th</sup> Framework Programme project “Femtoprint”.

# **Integrating optics and microfluidics to automatically identify algae species**

PROEFSCHRIFT

ter verkrijging van de graad van doctor aan de Technische Universiteit Eindhoven,  
op gezag van de rector magnificus prof.dr.ir. F.P.T. Baaijens,  
voor een commissie aangewezen door het College voor Promoties,  
in het openbaar te verdedigen op woensdag 20 mei 2015 om 16:00 uur

door

Allison Marie Schaap

geboren te New Westminster, Canada

Dit proefschrift is goedgekeurd door de promotoren en de samenstelling van de promotiecommissie is als volgt:

voorzitter: prof.dr.ir. A.A. van Steenhoven

1<sup>e</sup> promotor: prof.dr.ir. J.M.J. den Toonder

co-supervisor: Dr. Yves Bellouard (TU Eindhoven / EPFL)

leden: Dr. Hatice Altug (École Polytechnique Fédérale de Lausanne)  
Dr. Thomas Rorhlack (Norwegian University of Life Sciences)  
Dr. David Sinton (University of Toronto)  
prof.dr.ir. P.D. Anderson

adviseur: PD Dr.-Ing. Timo Mappes (Karlsruhe Institute of Technology & Carl Zeiss AG)

# Contents

Societal summary .....	viii
------------------------	------

## 1. Introduction: Algae meet microfluidics.....1

1.1	Introduction .....	2
1.2	Algae basics .....	2
1.2.1	Monitoring algae species dynamics .....	4
1.2.2	Economic impacts of algae growth.....	6
1.3	Performance requirements for algae identification technology.....	7
1.3.1	Typical algae distributions .....	7
1.3.2	Performance requirements .....	9
1.4	Traditional algae identification methods .....	11
1.4.1	Laboratory-based identification processes .....	11
1.4.2	Field-deployable identification technologies.....	13
1.4.3	Remote techniques .....	13
1.5	Algae on lab on a chip devices.....	14
1.5.1	Lab on a chip.....	14
1.5.2	Algae in lab on a chip devices.....	14
1.6	Conclusions and relation to thesis .....	17

## 2. Fabrication, modelling, and characterization of the optical algae identification system .....19

2.1	Introduction .....	20
2.2	Microfabrication with a femtosecond laser.....	20
2.2.1	Examples of femtosecond laser fabrication.....	21
2.3	System principle and experimental setup .....	23
2.3.1	System design.....	23
2.3.2	Beam characterization.....	24
2.3.3	Experimental procedure .....	25
2.3.4	Samples .....	27
2.4	System characterization and initial results.....	28
2.4.1	Sample data.....	28
2.4.2	Characterization and optimization experiments.....	28
2.4.3	Self-alignment of high aspect ratio particles .....	33
2.4.4	Microsphere and algae size correlations .....	34
2.4.5	Overview of classification strategy.....	35
2.5	Optical modelling.....	36
2.5.1	Mathematical and geometrical basis.....	36
2.5.2	Model steps and geometric simplifications .....	38

2.5.3	Sample results.....	39
2.5.4	Algae modelling .....	44
2.6	Conclusions .....	47
<b>3. Pattern recognition, results, and analysis of the optical algae</b>		
	<b>identification system .....</b>	<b>49</b>
3.1	Introduction .....	50
3.2	Pattern recognition methods.....	51
3.2.1	Discriminant analysis.....	51
3.2.2	Neural networks.....	52
3.3	Results: Neural networks vs. discriminant analysis.....	53
3.3.1	Test 1: Sizes of microspheres.....	53
3.3.2	Test 2: <i>Cyanotheca</i> & detritus.....	55
3.3.3	Test 3: five mixed algae species .....	56
3.4	Neural network optimization.....	58
3.4.1	Training algorithm.....	58
3.4.2	Number of hidden neurons.....	60
3.4.3	Performance function and regularization parameter .....	60
3.4.4	Trade-off between certainty and samples identified .....	61
3.4.5	Best classification results .....	63
3.5	Discussion .....	64
3.6	Conclusions .....	66
<b>4. Sorting algae with optical and fluidic forces .....</b>		
<b>69</b>		
4.1	Motivation: Phylogenetics vs phenetics.....	70
4.1.1	Phenetic classification schemes .....	70
4.2	Passive particle sorting methods .....	73
4.2.1	Sorting particles with optical forces .....	73
4.2.2	Sorting particles with inertial microfluidics.....	75
4.2.3	Combining or competing optical & fluidic forces.....	78
4.3	Optofluidic sorting experiments .....	79
4.3.1	Principle .....	79
4.3.2	Modelling the combined optofluidic forces.....	79
4.3.3	Simulation results.....	83
4.3.4	Experimental setup.....	85
4.3.5	Microchannels .....	86
4.3.6	Experimental results of optofluidic separation.....	86
4.4	Size-separation with fluidic forces.....	89
4.4.1	Experimental .....	89
4.4.2	Data analysis .....	91
4.4.3	Results .....	92



4.5 Discussion and conclusions .....	96
<b>5. Conclusions &amp; outlook.....</b>	<b>99</b>
<b>References .....</b>	<b>104</b>
<b>Summary .....</b>	<b>112</b>
<b>Samenvatting.....</b>	<b>114</b>
<b>Acknowledgements .....</b>	<b>116</b>
<b>List of publications.....</b>	<b>117</b>
<b>About the author .....</b>	<b>119</b>

# Societal summary

Algae are present in nearly every body of water on the surface of the earth. These microscopic organisms produce over half of the oxygen on earth, and are vital to life on the planet. However, algae can also cause significant and expensive environmental damage when their local ecosystem is thrown out of balance by, for example, the addition of pollutants to the water. Counting and identifying the species of algae in water can help with understanding this complex process, as well as being useful for monitoring the safety of drinking water, measuring developing algae blooms, and protecting aquacultures. However, the technology for achieving this is lacking.

The PhD work presented here tackles this problem by integrating tools from two different fields: optics and microfluidics. We use a femtosecond laser to machine a piece of glass to include a microchannel to transport water with algae and a waveguide which can transmit light. This chip, together with a laser and a simple optical detector, allows us to obtain light-based “fingerprints” of different species of algae as a sample flows through the device. We can use these measurements to extract information about the algae size and shape, and then we can classify the species using neural networks which can be trained to recognize patterns. Besides this optical identification, we also showed that we can use microfluidics and optics to passively sort the algae by size, which is a useful tool for pre-sorting the samples before doing measurements.

This new technology provides a novel tool with which we can automatically and rapidly count and identify the algae in water. It will allow researchers, regulatory agencies, aquaculture farmers, and ship owners to save money and time in sample collection, and could lead to a better understanding of the way we impact the environment.

# 1

Introduction:  
Algae meet microfluidics

## 1.1 Introduction

As primary producers of oxygen, algae are important organisms for understanding and monitoring the environment. Algae species dynamics – the amount and concentrations of the species in a body of water – vary in response to changing environmental conditions. These conditions can include the concentration of nutrients, temperature, light conditions, and intentional or unintentional human intervention. This sensitivity to the environment makes algae a useful biomarker for changes occurring in the water and surrounding area.<sup>1,2</sup> Beside the use of algae as surrogate sensors, monitoring species dynamics can be useful in identifying and studying harmful algae blooms, which can occur when the local nutrient supply changes. These blooms may consist of toxin-producing algae<sup>3,4</sup> or non-toxin-producing algae. Even in the latter case, the bloom can destroy the local environment, causing damage to other aquatic life.<sup>5</sup>

Algae monitoring is therefore essential not only for studying environmental changes, but also as a public health necessity. Indeed, as part of an increasing worldwide effort to understand and control the impact of human activity on the environment, algae monitoring is enforced in government regulations on water quality. Finally, algae monitoring is also of economic importance in the farming of algae as a fuel source, when a population of desired algae needs to remain uncontaminated by other species.

Knowing the amount and type of algae in a given body of water is clearly useful for many applications, but there is a lack of quick and low-cost methods for doing so. The most common method of identifying algae is to manually identify specimens in a water sample. This process is slow and limited in scope, but the existing alternative technologies have yet not offered adequate flexibility or automation to replace it.

**This thesis describes work done to address this technology gap; the approach presented here takes advantage of integrated optical and microfluidic technology to enable the automatic identification of algae.**

This introduction presents some background on algae and their identification, followed by an overview how the lab on a chip field has intersected with algae.

## 1.2 Algae basics

“Algae” is a broad term, encompassing organisms from the micro- to the macro-scale. It is not itself a formal taxonomical term but rather a general classification of organisms, which share some morphological and ecological traits. Algae species range

in size from the several meters of the gigantic kelp forest in Californian shores, to the centimetres of the invasive seaweed *Caulerpa taxifolia* that caused great damage upon its accidental introduction to the Mediterranean sea, to the submillimetre scale of the microalgae in Figure 1.

In this thesis, the term “algae” is used to refer exclusively to submillimetre phytoplankton (“microalgae”) for simplicity. The term *phytoplankton* specifies organisms that are drifting in water, and which use light or energy from chemical reactions to convert inorganics into organic compounds, through photosynthesis or chemosynthesis. Algae are distinct from plants; they lack specialized tissue forming roots, leaves, stems, and vascular tissue, and their reproductive systems and life cycles are typically simpler.

Algae exhibit a wide array of morphologies, as illustrated in Figure 1. They are found in fresh or salt water and in a broad range of values for pH, temperature, turbidity, oxygen levels, and carbon dioxide levels.

All algae contain chlorophyll-*a*, which enables the conversion of carbon dioxide, water, and light into oxygen and carbohydrates. Algae also contain accessory pigments which work in conjunction with chlorophyll-*a* to widen the range of wavelengths which can be used by the algae, as well as protective pigments which protect from photodamage.<sup>6</sup> These pigments – which can include carotenoids, xanthophylls, and

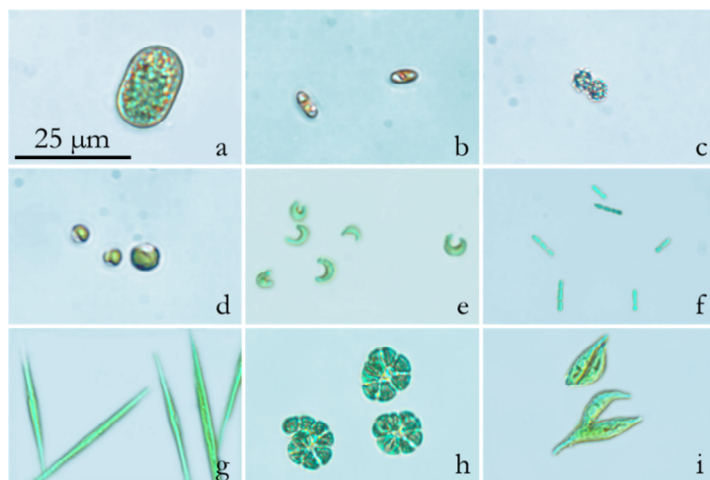


Figure 1. Microscope images of some of the algae species used in this research: (a) *Cyanothece aeruginosa*, (b) *Navicula pelliculosa*, (c) *Microcystis viridis*, (d) *Chlorella vulgaris*, (e) *Pseudokirchneriella subcapitata*, (f) *Pseudanabaena* sp., (g) *Monoraphidium griffithii*, (h) *Anabaenopsis* sp., (i) *Scenedesmus acuminatus*.

Table 1. Spectral ranges (approx.. half-maximum values) of absorption and emission for some common algae pigments. Data compiled from various sources.<sup>6,8-10</sup>

<b>Pigment</b>	<b>Absorption maximum</b>	<b>Emission maximum</b>
Chlorophyll- <i>a</i>	400-440 nm	660-690 nm
Chlorophyll- <i>b</i>	520-570 nm	640-670 nm
Phycocyanin	500-560 nm	630-670 nm
Phycocerythrin	470-510 nm	550-590 nm

the fluorescent phycobilins – have different wavelengths of peak light absorption, ranging from roughly 400 nm through 700 nm (see Table 1).

The different phyla (groups of species) of algae possess different typical combinations of these pigments, lending them the colours which are often the basis for the informal names of the group (for example, “green algae” for the chlorophyta, “brown algae” for diatoms, and “red algae” for the rhodophyta).<sup>7</sup> Different colours are prominent in different geographic regions or environments, as certain species or families are better adapted to certain intensities or wavelengths of light.

Algae can exist alone or as aggregates, with or without flagella for motion control. Algae surfaces feature a simple cell membrane, made of a lipid bilayer 7-8 nm thick. Additional structures and materials may also be present.<sup>7</sup>

The density of algae is only slightly higher than that of fresh or sea water, generally between 1.03 and 1.10 g/cc. Algae need to control their depth to access light and to move to regions of undepleted nutrients. Some algae can control motion with flagella, while some others regulate their position by controlling their buoyancy with gas-filled structures inside the cell or by producing liquids with lower density than water.<sup>7</sup>

It is evident that algae are a widely diverse set of organisms, and thus pose interesting challenges in their identification as well as interesting opportunities for their use.

## 1.2.1 Monitoring algae species dynamics

Monitoring the *species dynamics* – the amount and concentration of the species in a body of water – can help identify and study harmful algae blooms (HABs, see Figure 2). Algae blooms can occur when the local environment changes, particularly when the limiting nutrient (usually phosphorus or nitrogen) rapidly becomes available in higher supply. Blooms can be particularly harmful if they consist of toxin-

producing species such as cyanobacteria, also known as blue-green algae. The cyanotoxins produced by these species have been known to cause mass animal mortalities, and can have neurotoxic or hepatotoxic effects in humans.<sup>3,4,11,12</sup> Even a bloom of non-toxin-producing algae can have serious consequences, as the accumulated biomass of the bloom can cause local oxygen depletion or habitat destruction by blocking light to submerged vegetation.<sup>5</sup>

The formation of algae blooms are complex events, involving the interplay of many variables; better methods of monitoring the dynamics of the species and the local environment would help to detect, understand, and respond to such events.<sup>5,13,14</sup>

As described by Anderson et al.,

“All too frequently, public perception of whether nutrient over-enrichment has reached undesirable levels has been based on acute, obvious or easily measured symptoms, such as high biomass algal blooms, massive fish kills, and oxygen deficits. Because of this focus, a broad array of indirect, chronic, often-subtle but serious impacts of nutrient pollution on aquatic ecosystems remain underemphasized and, in some cases, poorly understood.”

(from D. Anderson et al.<sup>5</sup>)

Further interest in algae monitoring comes from the need to inform and enforce government regulations. For example, a European Parliament directive requires the



Figure 2. Harmful algae bloom (HAB) in Lake Erie. Photo credit: the Michigan Sea Grant, [www.miseagrant.umich.edu](http://www.miseagrant.umich.edu)

monitoring of recreational water quality, which can include the use of algae and cyanobacteria as markers thereof.<sup>15</sup> The success of the Dutch provinces in meeting these water quality standards is shown in Figure 3.

Concerns over the introduction of foreign algae species by the dumping of ship ballast water has also prompted the need for fast-response, portable algae species monitoring.<sup>16</sup> Algae have also been proposed and studied as a fuel source; farming algae for this purpose may also require an accurate understanding and monitoring of the species distribution.

## 1.2.2 Economic impacts of algae growth

In the EU, it is estimated that HABs cost approximately €589 million/year.<sup>17</sup> These costs include damage to commercial fisheries, treating illnesses, negative impacts on tourism and recreational facilities, and the costs of monitoring and management of the blooms. This is a world-wide problem: in the USA, HABs cost at least \$82 million/year<sup>18</sup> (about €67 million/year), and in China, a single algae bloom lasting two weeks caused an estimated loss of €4.5 million to commercial fisheries in 2005.<sup>19</sup>

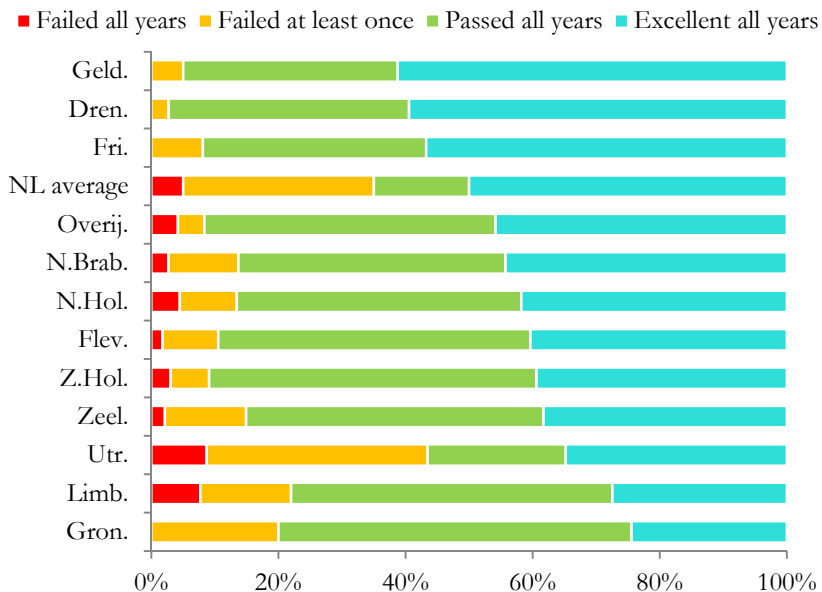


Figure 3. Water quality in the Netherlands, by province, based on the results of 2011-2013 according to the standards set in Directive 2006/7/EC of the European Parliament.<sup>15</sup>



## 1.3 Performance requirements for algae identification technology

The United States Environmental Protection Agency performed a National Lakes Assessment (NLA) in 2007. 1157 lakes across the country were sampled and the phytoplankton in each sample were counted and identified by species. This data provides a useful glimpse into the ranges of abundance (number of cells per volume of water) and number of species seen *in situ*. This data will be used to identify some performance requirements of an automated algae identification system.

### 1.3.1 Typical algae distributions

The NLA data show a mean highly nonlinear distribution of phytoplankton abundance (Figure 4). The mean abundance was  $3.8 \times 10^4$  cells/mL and the median abundance  $7.16 \times 10^3$  cells/mL. The maximum abundance measured was  $4.99 \times 10^6$  cells/mL water, which was measured in Caruth Lake, Texas; over 99.9% of the cells taken in this sample were the cyanobacteria *Microcystis*.

### Species dynamics and distributions

Most sites had a large number of species present: between 1 and 69 species were identified at the sites, with the median number of species at 24 (Figure 5, top). Of the

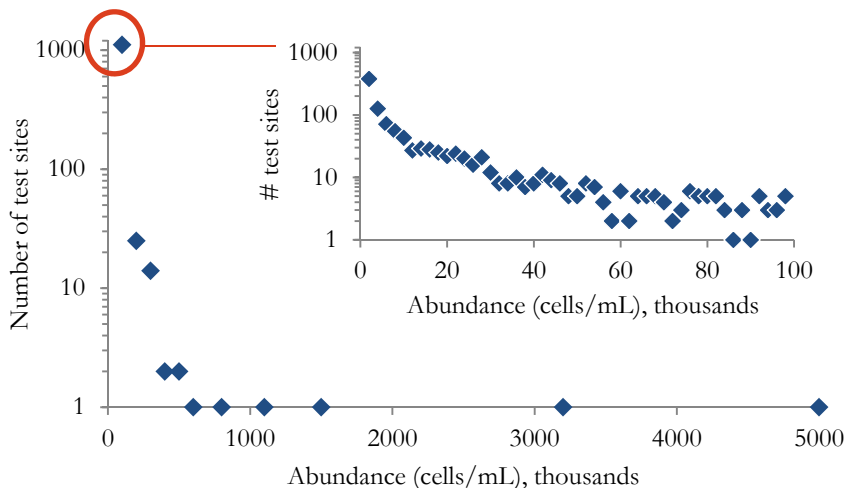


Figure 4. Abundance of phytoplankton measured by the US EPA National Lakes Assessment 2007 study.<sup>20</sup> The inset shows the distribution of the abundance values captured in the first data point of the main graph.

1157 test sites, 884 sites (76%) had 10 or fewer species representing 90% of the phytoplankton population, and 925 sites (80%) had 5 or fewer species responsible for 70% of the phytoplankton population. However, a much smaller number of species dominate the population; examples from four randomly-selected test sites from the EPA NLA data demonstrate this effect (Figure 5, bottom).

The vast majority of sites had a small number of species (<10) with an abundance of

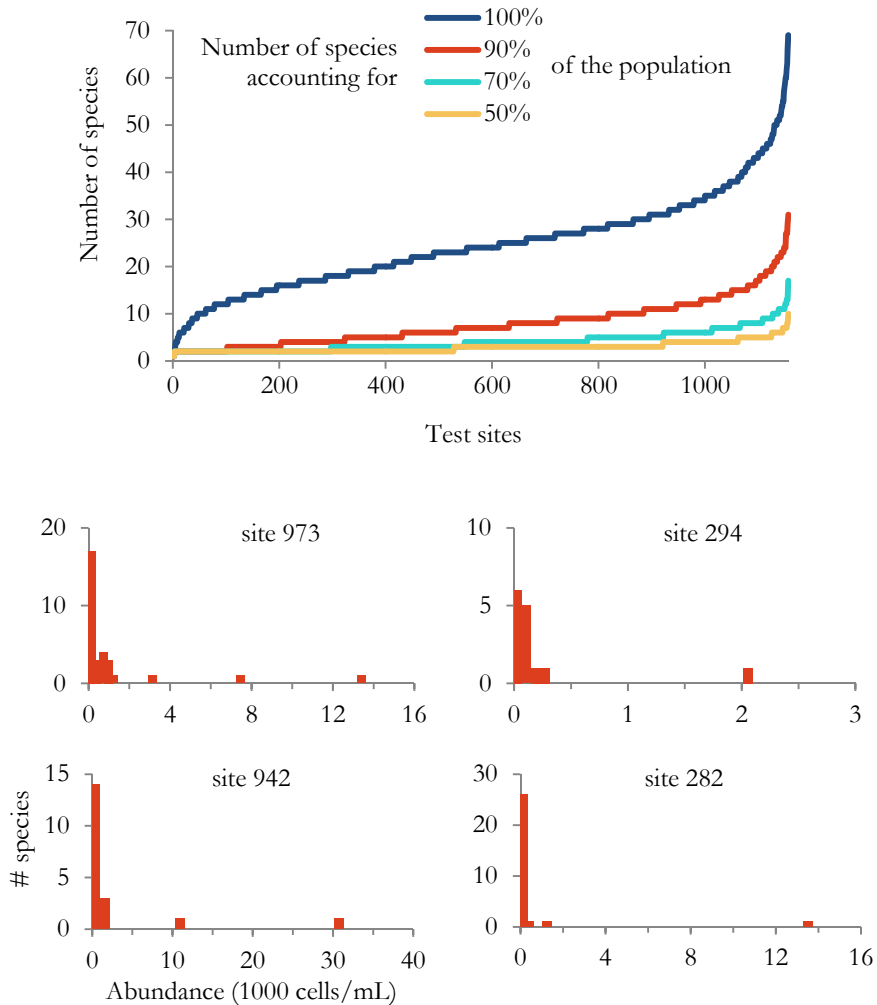


Figure 5. (Top) Distribution of phytoplankton species as measured in the US EPA NLA. (Bottom) Distribution of phytoplankton species by abundance (thousands of cells per mL water) for four randomly-selected locations. Source of raw data: US EPA NLA (2007).<sup>20</sup>

at least 10% that of the most abundant species (Figure 6). The single-most dominant species accounted for, on average, half of the phytoplankton measured (Figure 7). The number of species present was not significantly related to the abundance of cells present (Figure 8).

### 1.3.2 Performance requirements

All of this data can provide tools for setting device performance requirements. While user needs would define the ultimate benchmarks, routine monitoring could focus on either the few species that dominate the population, or could measure the relative abundance of the most populous species before or during an algae bloom. In cases where this type of strategy would be acceptable, this suggests a set of technological benchmarks that should be met by an automated monitoring system.

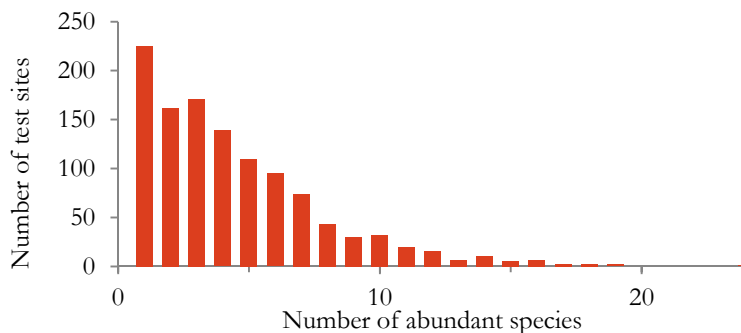


Figure 6. Number of species with an abundance at least 10% that of the most abundant species. Data from US EPA NLA.<sup>20</sup>

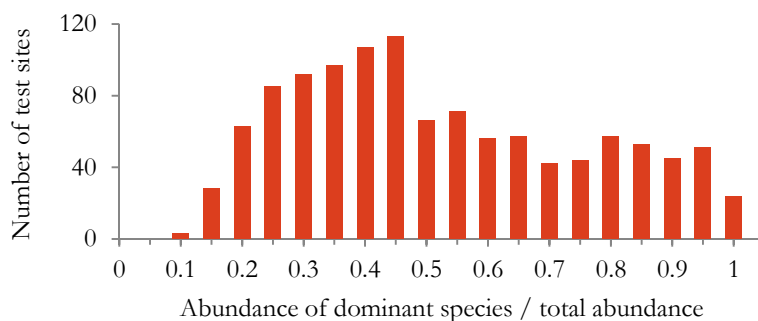


Figure 7. Relative dominance of the single most abundant species. The relative dominance of the most populous species varies widely, but on average it is responsible for about half of the phytoplankton in a given sample. Data from US EPA NLA.<sup>20</sup>

## Concentration and species abundance

First, the system should be able to handle high concentrations of hundreds of cells/mL, while still being able to handle the more common case of having tens of cells/mL. The method should be able to distinguish between several (up to 10) species regularly and over a longer term than provided by manual identification. The analytical method should not depend on having similar concentration levels of each species, but rather be flexible enough to accommodate the most abundant species representing between 20% and 100% of the local population.

## Measurement volume and time

According to the National Oceanic and Atmospheric Administration (USA), the time for an algae population in the ocean to double can be from hours to a few days in good conditions.<sup>21</sup> Any system will have a trade-off between the volume of sample and the time over which the sample is analysed. The rate of algae growth suggests useful monitoring data would be provided from a system that can provide time resolution on the scale of around a day in low-concentration conditions and around an hour in high-concentration conditions.

An EPA standard operating procedure for phytoplankton identification calls for between 2.5 and 50 mL samples to be used.<sup>22</sup>

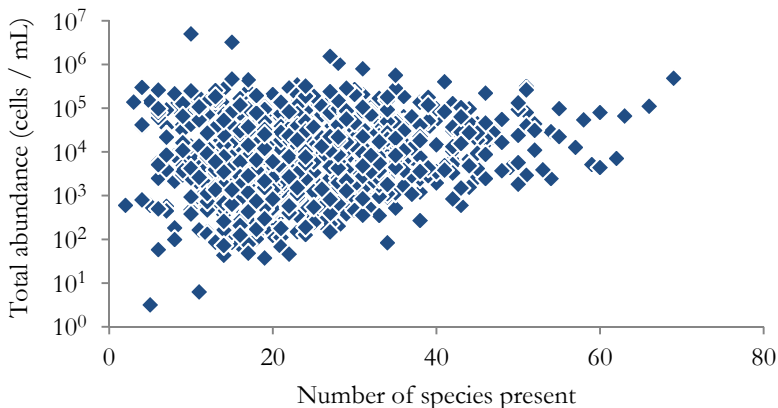


Figure 8. The US EPA NLA data<sup>20</sup> shows no significant correlation between the total phytoplankton abundance and the number of species present.

## Potential failure scenarios

A system that conforms to these guidelines should be able to provide useful monitoring in the vast majority of cases. It would potentially fail in two situations: one, where the concentration of algae is so high that it exceeds the capacity of the sensor (i.e., in an algae bloom), and second, in the case where there is a low concentration of many different species. In the first case, the growth of the algae bloom would have already been monitored, and the device could presumably warn the user of the excessive concentration. In the second case, automated computer clustering would be likely to fail. This case may be of less interest for (for instance) regulatory monitoring but it may well be of interest for research purposes, and thus complementary identification approaches may be required.

## 1.4 Traditional algae identification methods

To illustrate which characteristics of algae have successfully been used for identification, an overview of existing methods for algae classification is presented here. We will first present methods that require laboratory-based equipment unsuitable for *in situ* use. We then continue with several field methods which seek to automate these approaches proven in a laboratory setting, and lastly we present remote techniques, which provide rapid and large-area data on phytoplankton concentration.

### 1.4.1 Laboratory-based identification processes

The most common traditional and current method of single-cell algae identification is using light microscopy. For water monitoring purposes, this requires collecting a sample, bringing it to the lab, fixing the cells, storing the sample, and later imaging the sample to manually count and identify the species present. While this is a reliable method, it is too time-consuming and slow to use for rapid monitoring.<sup>7</sup>

### Optical methods

Optical methods are a promising approach for algae identification, as algae have a variety of shapes and structures (i.e. morphological identification) and contain coloured pigments necessary for photosynthesis (i.e. pigment identification).

Automated morphological identification that relies on using image recognition has been achieved primarily on stationary specimens on a microscope.<sup>23–26</sup> More recently,

species identification through image recognition has also been attempted for moving samples in a stream of water.<sup>25</sup> The approach faces several challenges: large amounts of data are collected, and must be compared quickly against large libraries of shapes in computationally-heavy processes. Additionally, expensive optics and good lighting are required to ensure good image quality, and for a moving algae sample in particular, a high-speed camera is needed to obtain adequately good images.

The second main automation approach to algae identification is based on measuring the contents of the algal cells, usually relying on pigment analysis. As described in section 1.2, algae possess a wide range of pigments and these have been used to distinguish between species or between different lines of the same species.

Flow cytometry, commonly used in biomedical applications for cell counting or sorting, can also be applied to algae. In a flow cytometer, the cells are hydrodynamically focused into a narrow stream, and passed in front of one or more light sources which excite autofluorescence in the algae. The system collects the scattered light and the excited fluoresced light from a large number of samples. These measurements are used to calculate parameters such as the ratio of chlorophyll to the algae size (as measured by side scattering) or to some accessory pigments, such as phycoerythrin (PE) or phycocyanin (PC) (see Table 1). These parameters are then input into a cluster analysis which distinguishes the different groups present within the sample.

The most common flow cytometric approach for algae is to excite fluorescence at one single wavelength and measure the fluorescence emission at multiple wavelengths.<sup>27–30</sup> Excitation at multiple wavelengths with the emission measured only at one has also been demonstrated for species classification.<sup>31–34</sup>

Measuring both the fluorescent and non-fluorescent pigments for algae classification offers more data than purely fluorescent methods such as flow cytometry, but at the cost of a significantly slower and more complicated system. This can be done on a single intact cell or in bulk after lysing a sample of cells, typically using a chromatography and spectrometry approach. Raman spectroscopy, for example, has only been attempted a few times as a classification method, and on fairly small datasets.<sup>35,36</sup> It has been used more often for compositional analysis of a fixed, concentrated sample of algae.<sup>37,38</sup> An alternative spectroscopic method, Fourier Transform Infrared (FTIR) spectroscopy, was used to distinguish two very similar diatoms which are very difficult to differentiate by microscopy.<sup>39</sup> FTIR has also been used for classifying cyanobacteria.<sup>40</sup>

## 1.4.2 Field-deployable identification technologies

These laboratory techniques have also been developed for *in situ* application with limited success. Handheld fluorescence meters are available; rather than the single-cell approach of a flow cytometer, they measure the total amount of chlorophyll present in a given amount of water. The submersible FlowCAM system acquires fluorescence measurements and photographs of particles in the size range 10  $\mu\text{m}$  – 600  $\mu\text{m}$  with a throughput rate of up to 3 mL/min depending on the particle size of interest.<sup>41</sup> Designed to be deployed from – and tethered to – a fixed object, it requires 67 W for normal operation and weighs 48 kg, with a volume of approximately 0.25 m<sup>3</sup>. The submersible Cytobuoy system similarly provides a cluster analysis based on in-situ measurements of scattering and fluorescence of particles in water, with an option for triggering selective image capture as well.<sup>31,32</sup> These systems offer reasonable throughput rate but at a high price and with limited portability.

## 1.4.3 Remote techniques

Lastly, the identification of algae blooms and quantification of average algae biomass *in situ* is possible with satellite imaging (Figure 9) or by measuring the absorption or scattering of light under water. Both techniques can provide information about a large volume quickly, but at the cost of specificity. Satellite data provides an average measurement of the chlorophyll load of water, but lacks specificity at the species level and is not sensitive enough for early detection of outbreaks.<sup>43</sup> Scattering or

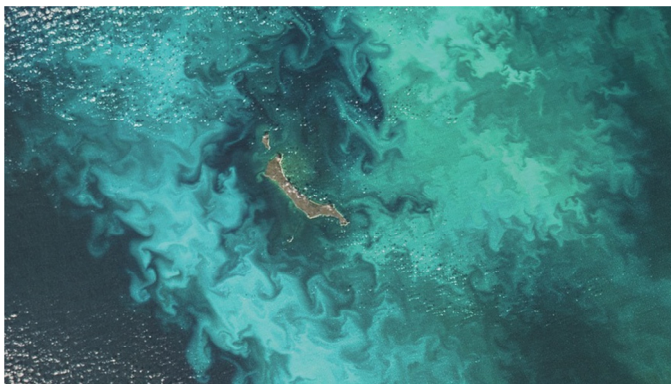


Figure 9. Algae blooms surrounding the 51 km long St. Matthew Island in the Bering Sea. The image was taken by the MODIS (Moderate Resolution Imaging Spectroradiometer) satellite, owned by NASA. Source: NASA/MODIS Ocean Color Image Gallery.<sup>42</sup>

absorption measurements can also offer a measurement of the total amount of chlorophyll, but are heavily dependent on the type of algae present and offer distinguishing only at the colour level, rather than the species level.<sup>44</sup>

## 1.5 Algae on lab on a chip devices

### 1.5.1 Lab on a chip

The research and development of lab on a chip devices – characterized by the miniaturization of laboratory equipment or functions onto the microscale – has grown rapidly over the past few decades. This growth was driven by a desire to mimic and take advantage of the scalability of mass parallel microfabrication technology, with the goals of making small-scale, low-cost, portable devices.<sup>45</sup>

These lab on a chip devices typically contain some form of fluid transport, commonly in channels with cross-sections on the scale of tens or hundreds of micrometres. The fluidics are then combined with on-chip functionalities including biological, optical, mechanical, electrical, or chemical-based sensing and actuation. Having a measurement volume on a similar scale to the object being measured can yield advantages in signal-to-noise ratio and reduce the power or the volume of reagents required. Using small, enclosed fluidic channels leads to more predictable fluid behaviour due to the low Reynolds number of the flow. This can offer more control over the local chemical and thermal environment, and allows the user to take advantage of forces, which scale advantageously with decreasing length scales.

Interested readers are referred to some of the many related reviews on, for example, optofluidics<sup>46</sup>, on-chip cell handling<sup>47</sup>, on-chip flow cytometry<sup>48</sup>, and system integration and requirements.<sup>49,50</sup>

### 1.5.2 Algae in lab on a chip devices

The use and study of algae in microdevices is spread over several fields and applications, and is not restricted exclusively to detection. Figure 10 shows a general overview of the uses of algae in microdevices, classifying them into three categories: the on-chip use of algae as fuel or sensors, the growth and manipulation of algae on-chip, and the detection or identification of algae. In some cases, of course, these functionalities may be combined.



The first category includes examples such as algae serving as biosensors or fuel. Algae have been used as on-chip biosensors through measuring, for example, optical<sup>51</sup>, conductometric<sup>52,53</sup>, and amperometric<sup>54</sup> markers of enzyme inhibition in the algae.

There are many other potential applications of algae as biosensors that have been – or may be – implemented in a lab on a chip device. One overview of such applications is presented by Brayner et al.<sup>2</sup> Algae have attracted attention as potential fuel sources and this interest has also translated down into the world of microdevices. In this capacity, algae have been used as a power source, for example, in a micro photosynthetic cells.<sup>55,56</sup> Micro-scaled optofluidic devices have also been exploited as bioreactors for growing algae as a fuel source.<sup>57–59</sup>

The second category (algae growth and manipulation on a chip) includes on-chip culturing<sup>60,61</sup>, imaging with an on-chip microscope<sup>62</sup>, the manipulation of algae by hydrodynamic tweezers<sup>63</sup>, and the lysis of algal cells<sup>64</sup>, sometimes combined with a subsequent analysis of cell contents.<sup>65</sup> These applications can, of course, overlap with the first category. Other goals for manipulating the algae are to analyse their contents, to study the properties of the algae themselves, or to use them as test cells for technology development.

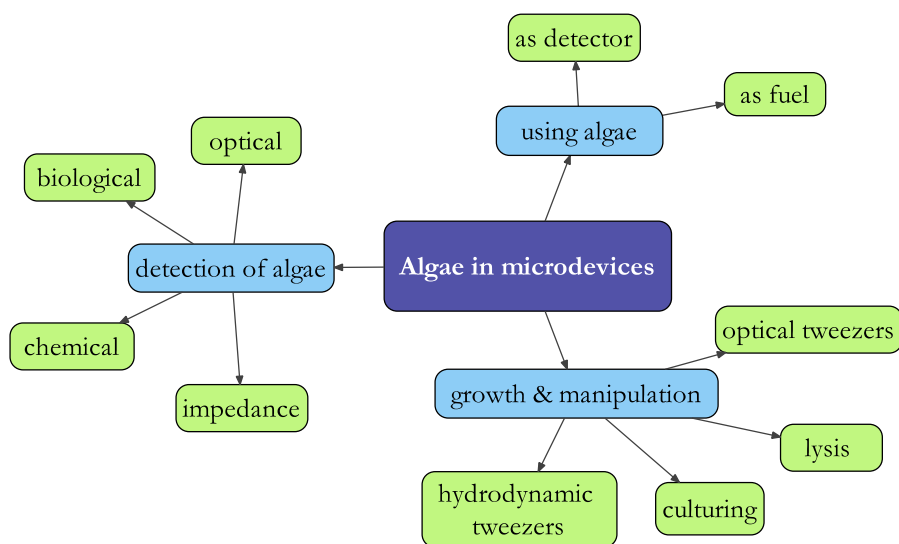


Figure 10. Overview of the use of algae in lab on a chip or MEMS devices. We classify the work reported in the literature into detection or counting technologies, technologies for the growth and manipulation of algal cells, and for the use of algae for other purposes.

The third category – phytoplankton counting and identification – has been performed using impedance spectroscopy<sup>66</sup>, scattering<sup>67</sup>, and fluorescence.<sup>8,68,69</sup>

An algae classification chip by Benazzi *et al.* used free-space, non-integrated optics and showed clear classification of a sample of three mixed algae species, with the results well-aligned to those obtained from a commercial flow cytometer.<sup>66</sup> In a second device, the photosensitive polymer SU-8 was used to define channel walls and grooves for seven optical fibres arranged around the channel.<sup>8</sup> The fibres were used to illuminate the sample and to collect fluoresced and scattered light. This chip was able to simultaneously perform fluorescence and impedance cytometry, and was used to classify particles in a mixed sample containing one species of algae and two different types of microspheres with different sizes and fluorescent dyes.

An improved device was presented by Hashemi *et al.* featuring a similar optical setup but with flow focusing in two dimensions instead of one (Figure 11).<sup>69</sup> This micro-scaled flow cytometer had optical fibres embedded in a polydimethylsiloxane (PDMS) chip, with external optical filters and photomultiplier tubes collecting the scattered and fluoresced light. In the first published prototype, fluorescence was excited at 488 nm

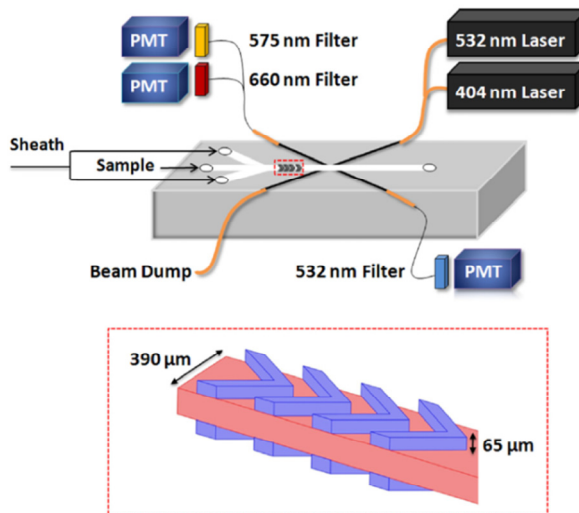


Figure 11. The microflow cytometer for algae identification presented by Hashemi *et al.*<sup>68</sup> Two wavelengths of light illuminate the sample, while two wavelengths of fluoresced light and the scattered light are measured with photomultiplier tubes. The flow is focused first in-plane with the sheath flow inlets (top image), and then in the out-of-plane direction by wrapping the sheath flow around the sample flow with grooves in the top and bottom of the channel (bottom image) (Reprinted from <sup>68</sup>.

Copyright Biomicrofluidics, 2011, American Institute of Physics.)

and three algae species were tested separately from one another in the microflow cytometer and in a commercial flow cytometer for comparison.<sup>69</sup> Three unmixed algae species were tested separately: *Synechococcus* sp. (cyanophyta), *Nitzschia dissipata* (bacillariophyta), and *Thalassiostrira pseudonana* (bacillariophyta). When overlaid, the scatter plots comparing the various optical parameters show clustering by species, most distinctly in the plot comparing phycoerythrin (PE) to chlorophyll (CHL). In comparison to the commercial flow cytometer, similar trends were observed in the PE-CHL plots, but the data comparing the CHL to side scatter and PE to side scatter were less consistent between the microflow cytometer and the commercial device. Nevertheless, the system was able to detect the small *Synechococcus* ( $\sim 1 \mu\text{m}$ ) which was not detectable by the impedance spectroscopy based methods described by Benazzi *et al.*<sup>66</sup>

Later work by the same group used two excitation lasers, at 404 nm and 532 nm, with the scattered light measured at 532 nm.<sup>68</sup> The best results were found at the lowest flow rate used: 167 nL/min. Four species of algae were tested: *Synechococcus* sp. (cyanophyta, diameter  $\sim 1 \mu\text{m}$ ), *Karenia brevis* (dinophyta, on the order of 10's of microns), *Alexandrium* (dinophyta, also 10's of microns), and *Pseudo-nitzschia* (baillariophyta, high-aspect-ratio cylinder of length in the 10's of microns and width in the microns). The analysis of the CHL, PE, and side scatter signals showed differences in the mean values of each species. However, there was significant overlap between the species due to wide variability within a single species. This makes classification based on these three parameters alone quite difficult.

## 1.6 Conclusions and relation to thesis

There is significant need in the research and market worlds for technology which can automate the process of algae identification. Lab on a chip methodologies are uniquely well-suited to tackling this problem, as they offer well-integrated fluidic handling and sensing technologies which match well with the size and properties of algae. The ability to reliably, quickly, and cheaply distinguish and count several species in a mixed sample would go far to improving the state of the art.

This thesis explores various methods of identifying algae, primarily using optical methods, and with a focus on glass-based devices which are fabricated using femtosecond laser micromachining. This fabrication technique and a first device which measures morphological features of algae will be presented in the next chapter. Following that is a focus on analytical work related to this device: signal processing and pattern recognition, evaluating device performance and exploring the use of

models to help interpret the data collected experimentally. The fourth chapter focuses on developing complementary technology which could improve the performance of the algae identification device. Specifically, it compares and evaluates two methods of passive size- and shape-based sorting both analytically and experimentally. The final chapter brings together all of these technologies with discussion and conclusions presented on their suitability for use together in the field.

# 2

Fabrication, modelling, and  
characterization of the optical  
algae identification system

## 2.1 Introduction

As exhibited in Chapter 1, algae exist over a wide variety of shapes and sizes. Algae cells absorb and scatter light, and these properties are often used to examine the optical properties of bulk volumes of water containing large numbers of cells. Here, we present a method to identify *individual* algal cells by monitoring intensity variations of a light signal transmitted through them. We use a glass-based microchip with a microchannel and waveguide included on a monolithic substrate, and demonstrate its use for building up a library of signals from different algal species. The glass chip is made with a relatively uncommon microfabrication technique: femtosecond laser micromachining. This chapter starts with an introduction to this technique before explaining the principles, characterization steps, and the experimental setup specific to our device. Some sample results are shown along with a description of the overall analytical approach. The next chapter focuses specifically on the data analysis, with various pattern recognition approaches examined and evaluated.

## 2.2 Microfabrication with a femtosecond laser

The design and abilities of microscale devices are often limited by the fabrication processes available. For lab on a chip devices, the most common manufacturing techniques have inherent two-dimensionality, or limited three-dimensionality. However, the creation of three-dimensional features for microdevices has many applications, and, in the case of the present project, allows the creation of uniquely robust optofluidic devices with a high signal-to-noise ratio. This is accomplished in glass by means of a two-step process: selective exposure of the glass to femtosecond laser irradiation, and subsequent etching.

Ultrashort pulses of light – i.e. pulses shorter than a picosecond – can be used to locally modify glass in such a way that the properties of the glass at the laser focal volume are permanently altered.<sup>70,71</sup> This alteration of the glass properties is a highly non-linear process: only regions in which the laser intensity exceeds a threshold value are affected. As a typical order of magnitude, in silica glass, the material used in this work, instant power must be in the range of a gigawatt per millimetre square to induce non-linear absorption effects. By moving a specimen under a femtosecond laser beam, truly three-dimensional patterns can be defined on the surface or inside the bulk of the glass (see setup, Figure 12).

Among the possible modifications induced by the laser beam, two are of particular interest for optofluidic device manufacturing. First, the index of refraction of the

modified glass is increased relative to the surrounding pristine glass. Second, the modified glass exhibits an increased etching rate in hydrofluoric acid or potassium hydroxide. The type of modifications induced by the laser depends on various laser parameters, such as the beam intensity, the pulse duration, the net fluence, and on focusing parameters like the numerical aperture. By modulating the laser exposure conditions while fabricating the device, one can combine on a single device zones with increased refractive indices and zones with increased etching rates. Features on the surface of the material will be etched, while waveguides can be created by producing continuous regions of high refractive index under the surface of the material, where they are protected from the etchant. For optofluidic applications in particular, three-dimensional waveguides and microchannels can be combined in a single monolithic piece of material, with a single fabrication process.

### 2.2.1 Examples of femtosecond laser fabrication

Femtosecond lasers have been used for microfabrication in a variety of applications, ranging from the purely optical to the purely mechanical, with combinations of optomechanics, optofluidics, and mechatronics also demonstrated.

As an example from microfluidics, femtosecond lasers have been used to produce 3D microchannel structures which work as microfluidic mixers.<sup>72</sup> The technology is particularly well-suited to this problem: the low Reynolds numbers typical in

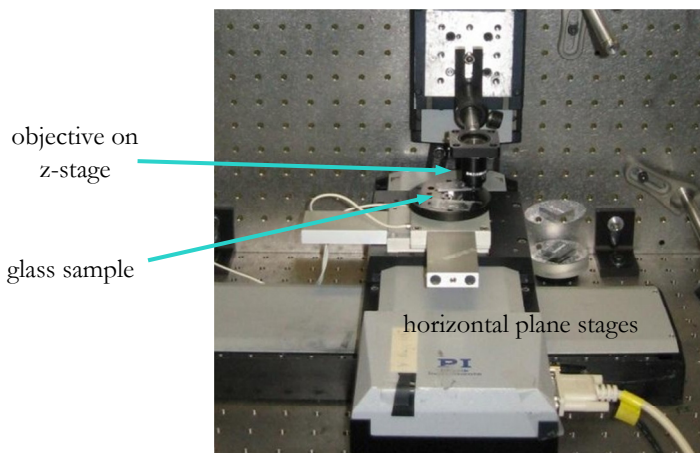


Figure 12. The final stage of the femtosecond laser micromachining setup. At the bottom are two stages, which move the sample in the horizontal plane. The position of the laser focus is controlled in the z-axis by moving the final objective on a third stage mounted perpendicularly to the horizontal plane.

microfluidic systems mean that the main mechanism for mixing liquids is the slow process of diffusion. Using three-dimensional geometry to mix and stretch flows to increase the area of contact between two liquids is an effective solution that is difficult to realize with more standard methods of microfabrication.

In micromechanics, three-dimensional flexures<sup>73</sup> or linear guidance mechanisms with integrated electronic actuation<sup>74</sup> can be manufactured with these lasers. Three-dimensional shapes fabricated in glass can also be used as a mould for soft polymer replication, enabling the low-cost replication of complex microstructures (Figure 13) which can create surfaces with specifically engineered optical or mechanical properties.<sup>75</sup>

Further functionalities can be created by taking advantage of the change of refractive index of the laser-modified zones. This has led to the creation of optofluidic chips with, for example, integrated waveguides for illuminating and collecting light from passing cells<sup>76</sup>, a device with a microchannel and integrated Mach-Zender interferometer<sup>77</sup>, and a “nano-aquarium” for observing living cells.<sup>78</sup> The combination of optics and mechanics has also led to optomechanical devices such as a distance encoder based on a linear guidance mechanism and multiple waveguides

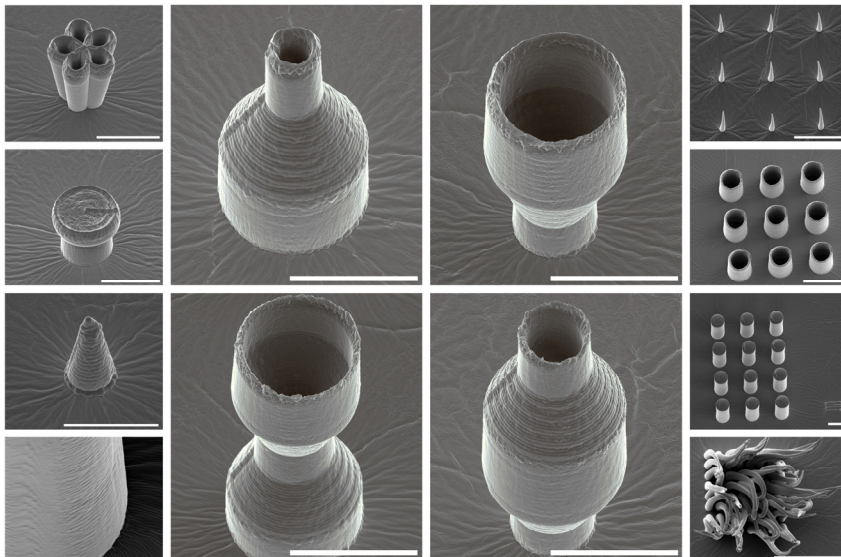


Figure 13. Polymeric 3D microstructures created by replicating a glass mould fabricated by a femtosecond laser. The material used here is PDMS; it was poured as a liquid onto the mould, cured, removed, and coated with gold to produce these SEM images. The scale bars are all 100  $\mu\text{m}$  long.



which align or misalign with one another as the mechanism moves.<sup>79</sup>

The first device presented in this chapter was fabricated off-site at Translume, a company which produces femtosecond laser fabricated microdevices. Later devices, including those presented in the other chapters of this thesis, were fabricated with a range of laser conditions. A typical set of parameters for microchannel fabrication was a laser power of 240 mW with a repetition rate of 800 kHz, resulting in a pulse energy of 300 nJ. Circularly polarized light was used, because with linearly polarized light the etching rate will vary according to the angle between the polarization and the writing direction. The writing was usually done at 5 mm/s in the x-y plane, although this varied between 1 mm/s and 10 mm/s depending on the position accuracy required for the device.

## 2.3 System principle and experimental setup

### 2.3.1 System design

The heart of the system consists of a glass (fused silica) chip with curved waveguide and microchannel fabricated with a femtosecond laser as described above. The system is shown schematically in Figure 14. The waveguide ( $8\ \mu\text{m} \times 8\ \mu\text{m}$ ) starts near one edge of glass, curves around 90 degrees, and ends perpendicular to a straight microchannel. The guided monochromatic light traverses the channel, exits the chip, and its intensity is measured with a four-quadrant photodetector next to the chip, as

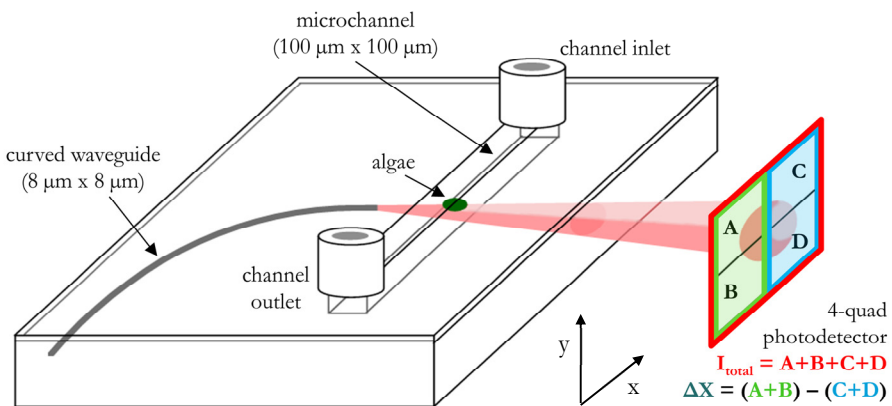


Figure 14. Schematic of the system: a curved waveguide directs single-mode 1550 nm laser light across a microchannel onto a photodetector while algae or other samples are transported in front of the beam.

depicted in Figure 14. The curved design of the waveguide prevents unguided light from reaching the detector. The waveguide is fabricated in the bulk of the substrate, buried at a depth of 50  $\mu\text{m}$  from the surface, so that the light is symmetrically distributed about the middle depth of the microchannel. The waveguide ends 500  $\mu\text{m}$  from the nearest channel wall; this distance is enough that the light exiting from the waveguide expands enough to illuminate the entire height of the channel. This expansion is defined by the numerical aperture of the beam, as described in the next section.

The channel is 100  $\mu\text{m}$  x 100  $\mu\text{m}$  in cross-section and 4 cm long. As the channel is fabricated on the surface of the glass, a thick film made out of PDMS is used for the fourth wall of the channel. The PDMS is not permanently bonded onto the glass, so that the channel can be easily cleaned if necessary. Fluidic access to the channel is provided by through-holes machined through the bulk of the glass at either end of the channel. PDMS cylinders with holes punched through them are used as tubing plugs and bonded permanently to the glass at the inlet and outlet.

## 2.3.2 Beam characterization

### Normalized frequency and numerical aperture

The properties of a waveguide can be described using dimensionless numbers that relate to the behaviour of the light wave inside of and after exiting the waveguide.

The *normalized frequency*

$$v = \frac{2\pi}{\lambda} a \sqrt{n_{\text{core}}^2 - n_{\text{cladding}}^2} \quad (3.1)$$

depends on the light wavelength  $\lambda$ , the waveguide radius  $a$ , and the indices of refraction of the core and cladding,  $n_{\text{core}}$  and  $n_{\text{cladding}}$  respectively. The normalized frequency is used to calculate the number of modes which can be propagated through the waveguide; if  $v < 2.41$ , only single-mode light can be propagated. In the device described in this chapter, we have  $\lambda = 1550$  nm,  $a \sim 4$   $\mu\text{m}$ ,  $n_{\text{core}} = 1.455$ , and  $n_{\text{cladding}} = 1.45$ , resulting in a normalized frequency of  $v = 1.95$ , indicating that the waveguide is single mode for this wavelength of light.

The *numerical aperture*

$$NA = n \sin(\theta) = \sqrt{n_{\text{core}}^2 - n_{\text{cladding}}^2} \quad (3.2)$$

of the waveguide indicates the half-angle  $\theta$  at which the light will diverge after exiting the waveguide into a medium of index  $n$ . In the device described here, the theoretical NA is 0.12 when the beam exits the waveguide.

The radius of curvature (18 mm) of the waveguide is dictated by the difference in index of refraction of the modified glass and pristine glass ( $\Delta n \sim 5 \times 10^{-3}$ ). A curved waveguide can cause optical losses if the conditions of total internal reflection are no longer met.

Given the waveguide and channel properties described above, a NA of 0.12 means that the beam radius

$$r_{beam} = 4 \mu m + 500 * \left( \frac{NA}{n_{glass}} \right) \quad (3.3)$$

as the beam crosses the threshold from the glass to the water of the channel is 45.7  $\mu m$ , with the half-angle of the beam cone in the water

$$\theta_{beam} = \sin^{-1} \left( \sin \left( \frac{NA}{n_{glass}} \right) * \frac{n_{glass}}{n_{water}} \right) = 0.09 \text{ rad} \quad (3.4)$$

with respect to the optical axis.

## Measurements of beam intensity distribution

The quadrant photodetector was temporarily replaced with a CCD camera with a phosphor coating for infrared sensitivity to capture images of the intensity profile of the beam after it crosses the channel and exits the chip. While the beam would ideally have a single-mode Gaussian profile, in reality the roughness of the machined surfaces also affects the beam intensity profile (Figure 15). The potential negative effects of this surface roughness are negated somewhat by the use of differential, rather than absolute, measurements with the photodetector. Even an asymmetrical intensity distribution can provide useful data as long as it is stable when there are no objects interacting with the beam.

### 2.3.3 Experimental procedure

During experiments, a syringe pump moves particle- or algae-laden water through the channel. A fibre-coupled laser source (1550 nm) was butt-coupled to the waveguide at the edge of the glass piece. The glass chip is shown in Figure 16, with a fibre coupled to the waveguide at the bottom left of the image.

The photodetector (New Focus model 2903) returns two signals: one, the intensity of the total detected light ( $I_{\text{total}}=A+B+C+D$ , as on Figure 14) and the other, the difference between the two upstream detectors and the two downstream detectors ( $\Delta X=(A+B)-(C+D)$ , as on Figure 14). A microscope objective (20x) and a camera were positioned above the channel, so that the particles or algae could later be identified manually and used to calculate the accuracy of the automated classification

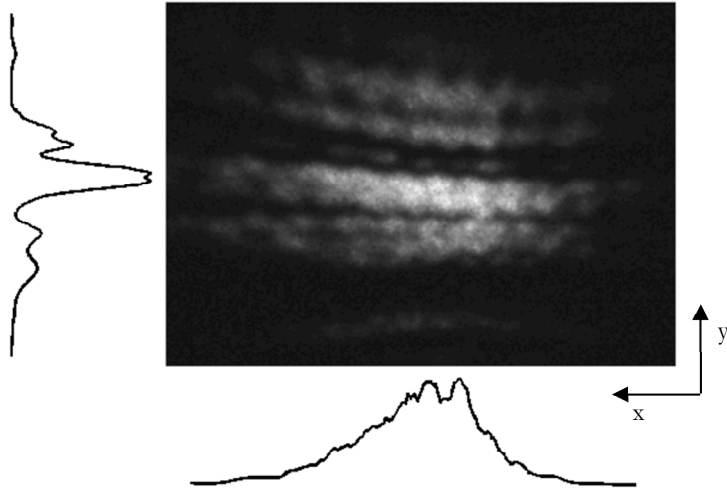


Figure 15. The beam intensity after its exit from the chip. The image was captured with an infrared-sensitive CCD camera while the channel was filled with water.

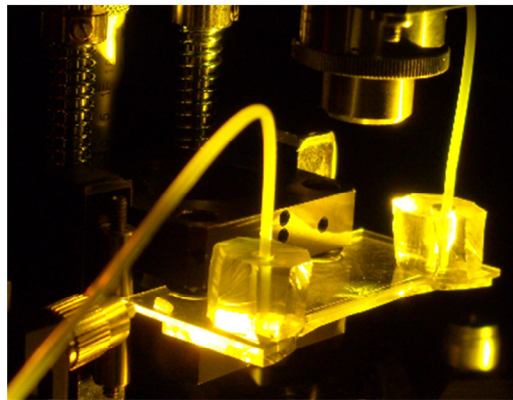


Figure 16. The microchannel system in the experimental setup. The two transparent cylinders with tubing inserted are the PDMS inlets and outlets; the metal cylinder in the bottom left corner is the optical fibre from the 1550 nm laser.

system. The photodetector signal was monitored and triggered the collection and storage of 100 ms of data at 2 kHz from the photodetector any time the  $\Delta X$  signal passed over a user-programmable threshold; simultaneously, the camera was triggered. This image is later used for measuring the accuracy of the detection method.

The use of the camera is necessary for device development in the lab, but ultimately not necessary in a field-deployable device. It imposes significant limitations on the maximum flow rate that can be used in the channel; if the flow rate is too high, the images will be too blurred to positively identify the specimens.

### 2.3.4 Samples

Nine algae cultures from the Norwegian Water Research Institute and polystyrene latex microspheres of three sizes (5  $\mu\text{m}$ , 10  $\mu\text{m}$ , and 20  $\mu\text{m}$ ; from Corpuscular Inc., USA) were used as specimens in this work. The algae cultures were stored in Z8 buffer<sup>80</sup>, and diluted with deionized water as necessary before use. 20 cells of each species were imaged and their dimensions measured to find statistical data about the size of each species (Table 2).

Table 2. The nine species of algae from the Norwegian Water Research Institute

Species Name	Abbrev.	Culture number*	ESD <sup>†</sup> ( $\mu\text{m}$ )	AR <sup>§</sup>
<i>Cyanothece aeruginosa</i>	S1	NIVA-CYA 258/2	$12.5 \pm 1.1$	1.4
<i>Scenedesmus acuminatus</i>	S2	NIVA-CHL 58	$8.1 \pm 1.1$	3.6
<i>Chlorella vulgaris</i>	S3	NIVA-CHL 19	$6.2 \pm 1.0$	1
<i>Microcystis viridis</i>	S4	NIVA-CYA 122/3	$8.0 \pm 0.8$	1.5
<i>Anabaenopsis sp.</i>	S5	NIVA-CYA 417	$10.2 \pm 1.5$	
<i>Navicula pelliculosa</i>	S6	NIVA-BAC 42	$5.5 \pm 0.3$	2.0
<i>Pseudokirchneriella subcapitata</i>	S7	NIVA-CHL 1	$4.2 \pm 0.7$	
<i>Pseudanabaena sp.</i>	S8	NIVA-CYA 504	$6.8 \pm 0.5$	3.9
<i>Monoraphidium griffithii</i>	S9	NIVA-CHL 8	$8.4 \pm 1.8$	17.4

\*The culture numbers are assigned by the supplier to indicate the specific strain and are provided here for reference.

<sup>†</sup>Equivalent spherical diameter.

<sup>§</sup>Average aspect ratio = largest dimension / smallest dimension; only presented for roughly ellipsoidal or cylindrical species

The device was tested with three separate types of samples. The first dataset is composed of microspheres of three diameters; the second dataset is a mixture of five species: the cyanobacteria *Cyanothece* and the algae *Chlorella*, *Microcystis*, *Anabaenopsis*, and *Monoraphidium*. The last dataset is based on field-collected water containing detritus with added *Cyanothece* cells.

For this third set, water was collected from the slow-moving Dommel River, which passes through the campus of the Eindhoven University of Technology. It was filtered to remove all particles above 100  $\mu\text{m}$  (to avoid clogging the microchannel), and lab-cultured *Cyanothece* cells were added to the water. A micrograph of the resulting detritus-*Cyanothece* mix is shown with the results of the experiments in Chapter 3 (section 3.3.2).

### Data preparation

Before being used in analysis, each photodiode signal is normalized so that the initial 25 ms of data have an average value of 0. From each signal obtained, various features of the signal are extracted and used in the pattern recognition approaches, which are described in the following chapter.

## 2.4 System characterization and initial results

### 2.4.1 Sample data

Figure 17 shows sample data from 9 species of algae cells. It should be noted that these examples are not specifically chosen as statistically representative of each species, but are rather intended to show examples of the types and general properties of the data acquired.

Each plot shows the total intensity of light hitting the quadrant photodetector,  $I_{\text{total}}$ , and the differential signal  $\Delta X$ . The smallest species, such as the *Pseudanabaena sp.* (S8) and *Navicula pelliculosa* (S6) have very low signal-to-noise ratios, particularly visible in the high-noise  $I_{\text{total}}$  signals.

### 2.4.2 Characterization and optimization experiments

In the species-recognition results in the following chapter, the quadrant photodiode collects data at 2 kHz, with a flow speed of 0.4  $\mu\text{L}/\text{min}$ . Ultimately, though, it would be ideal to run a field-deployable version of the system as quickly as possible (within

practical financial constraints), to increase the throughput rate. A series of characterization experiments examine the limitations of the systems response to flow speed (Figure 18 and Figure 19) and the level of trigger used to indicate the presence of a particle (Figure 20).

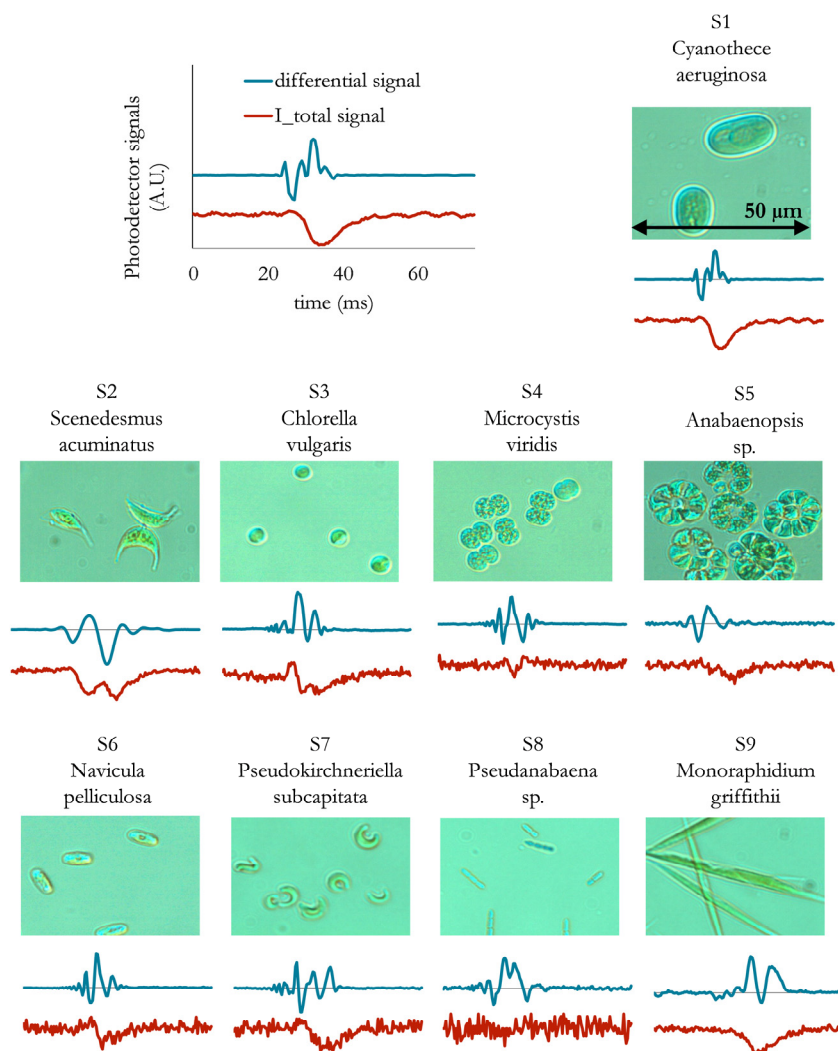


Figure 17. Differential ( $\Delta X$ ) and total ( $I_{total}$ ) photodiode signals obtained from nine species of algae, with corresponding micrographs, forming the basis of a library for comparison of data obtained by the optofluidic chip. Data was collected at 2 kHz for 100 ms; 70 ms of data are shown here, with the scaling on the y-axis in arbitrary units.

## Flow speed effects

Increasing the system flow speed causes a decrease in the amount of light blocked per particle (Figure 18). This was measured by calculating the value of  $h$  defined as

$$h = \max(I_{total}) - \min(I_{total}) \quad (3.5)$$

*i.e.*, the difference between the maximum and minimum of the  $I_{total}$  signal while a particle passed in front of the photodetector. By default, the system collects data at 2 kHz. The average velocity in the channel

$$V_{ave} = \frac{Q}{WH} \quad (3.6)$$

is the flow rate  $Q$  divided by the channel cross-section (width  $W$  times height  $H$ ). While the velocity of any given particle can vary from near-zero (if the particle is near a wall) to twice the average (at the channel centre), the average will be used for some estimates of the effect of flow speed on sampling behaviour.

A particle traveling at  $V_{ave}$  crosses the sampling zone defined by the width of the beam, which is just under 100  $\mu\text{m}$ . The time to cross the beam

$$t_{cross} = \frac{\text{beam width}}{V_{ave}} \quad (3.7)$$

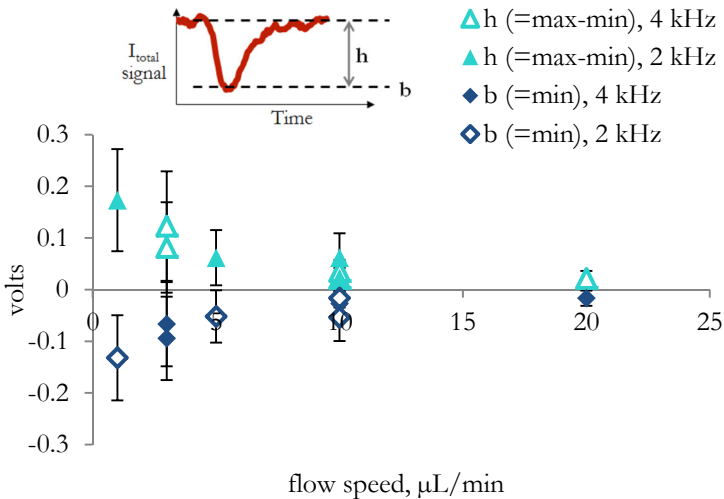


Figure 18. Effect of flow speed on the change ( $h$ ) and minimum ( $b$ ) of total light intensity at two different sampling rates (2 kHz & 4 kHz) of the photodetector. A sample recording (inset) shows the values being measured.



is 0.054 s for a flow rate of 1  $\mu\text{L}/\text{min}$ . At 2 kHz, this means that the 108 samples should be taken while the particle crosses the beam. For a flow rate of 10  $\mu\text{L}/\text{min}$ , this drops accordingly to 11 samples and for a flow rate of 20  $\mu\text{L}/\text{min}$ , 5 samples. The effect of this decrease can be seen in Figure 18, as the ability of the system to accurately represent the change in light intensity decreases as the flow rate increases. This behaviour is analogous to that described by the Nyquist sampling criterion in electrical engineering, which states that the sampling rate used to measure a time-variant system must be at least twice the rate of the highest-frequency signal of interest.

While low flow speeds may improve the system's ability to resolve the signal, they can cause other problems particularly when sampling with polystyrene latex (PSL) microspheres. The density of PSL is greater than that of water, so the microspheres eventually settle out of the flow during testing. This effect is demonstrated in Figure 19, where a measurement of particle concentration is made as a function of time for tests of 1, 2, and 5 minutes at a constant flow speed of 10  $\mu\text{L}/\text{min}$ . The apparent concentration decreases with increasing sample time.

### Threshold choice

While the system is running, it continuously monitors the  $\Delta X$  signal. If this signal exceeds a threshold value (because of the passing of a particle), data from the photodiode is saved and a photo of the channel contents is taken. The user has to set the threshold which defines an item of interest; too low a threshold means too much data with only noise and no algae, and too high a threshold risks missing cells. To find

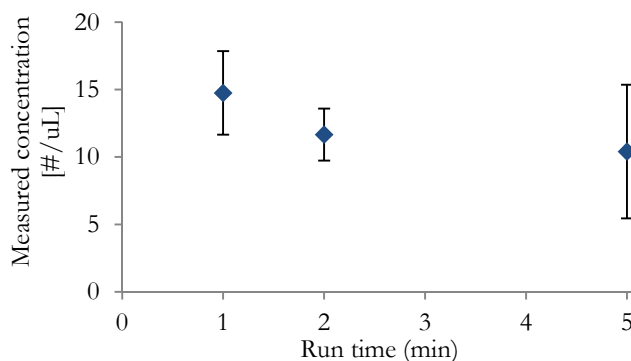


Figure 19. Results of particle counting experiment at different flow speeds. The apparent concentration decreases over time as particles settle out of the flow due to gravity.

an acceptable range of threshold values, continuous video was taken while water with  $10\ \mu\text{m}$  PSL microspheres was flown through the channel at  $1\ \mu\text{L}/\text{min}$ . The photodiode signal was continuously recorded, and later analysed with various threshold levels to compare the number of events to the number of particles seen in the video.

The threshold is defined as a multiple of the standard deviation of the noise on the signal (Figure 20). A threshold of 10 times the noise value provided a good match between the video and the photodetector; this was equivalent to a voltage of about 11 mV. The experiments with algae samples used a threshold value in this range, with a slightly lower value for very small species. In this experiment,  $10\ \mu\text{m}$  diameter beads were used with a flow rate of  $1\ \text{mL}/\text{min}$ .

The choice of this threshold is a combination of experimentally-informed statistics and value choices for the end user. First, as shown previously, higher flow rates adversely impact the system's ability to accurately measure the changes in the light intensity distribution. Therefore, for higher flow rates the threshold could be lowered to adjust for this effect. Second, it may be that the user would prefer to have a higher rate of false positives – that is, data which contains only noise– than risk missing the passage of an algal cell. In this case, a lower threshold would also be appropriate.

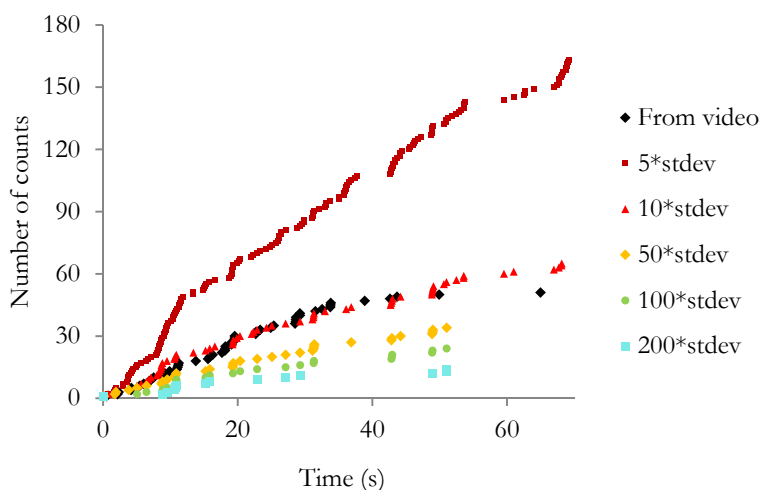


Figure 20. Effect of the trigger threshold (as a multiple of the standard deviation of the noise) on the particle count. The black points show the actual particle count, as counted from a video recording taken at the same time. The experiment used  $10\ \mu\text{m}$  microspheres with a  $1\ \mu\text{L}/\text{min}$  flow rate.

### 2.4.3 Self-alignment of high aspect ratio particles

Some algae species are highly non-spherical; when they are sent through the sensor system studied here, they are not forced into a particular orientation by external means. However, here the laminar flow inherent in microfluidics provides a benefit in the form of the time-independent Poiseuille flow field. The fluid at the centre of the channel is moving the fastest, with the flow at the walls constrained by the no-slip condition. This difference in flow speeds results in a velocity gradient perpendicular to the channel which causes high-aspect-ratio particles to self-align in the direction of the flow. This was studied with a sample of *Monoraphidium* algae, a highly non-spherical species with aspect ratios occasionally exceeding 20: A MATLAB-based automated image analysis script measured the angle  $\theta$  (inset, Figure 21) and aspect ratio of the *Monoraphidium* cells as they passed through the microchannel.

The percentage of cells with an angle within  $10^\circ$  of the channel axis was found; for samples with an aspect ratio greater than 6, 80% of the samples were within this measurement (Figure 21). The percentage of aligned particles is, unsurprisingly, dependent on the aspect ratio, and not significantly dependent on flow rate. The channel is very long compared to its cross-section, so presumably any flow-rate-dependent differences in the time to alignment have been rendered irrelevant.

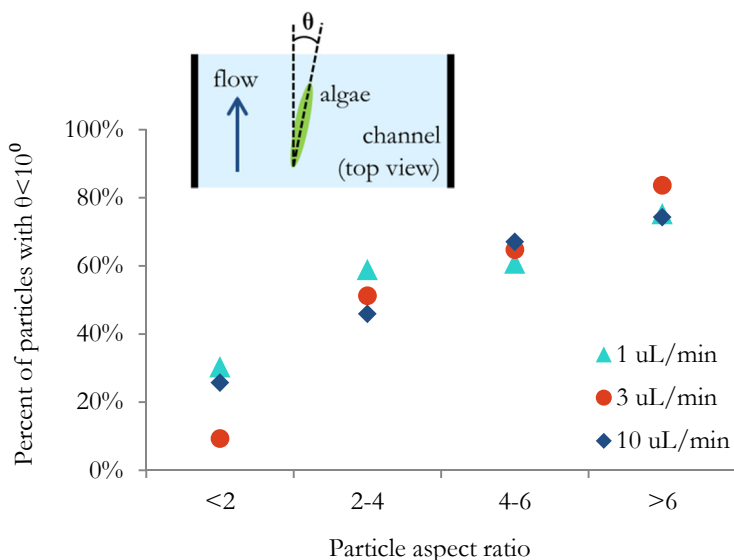


Figure 21. Orientation of high-aspect-ratio particles, represented as a percentage of particles with a long axis angled within  $10^\circ$  of the channel axis.

## 2.4.4 Microsphere and algae size correlations

Literature on algae suggests that knowledge of the size distribution of the algae present in a body of water can be a valuable tool for monitoring the species dynamics<sup>81</sup>. With this motivation, PSL microspheres were used to examine the specimen size dependence of the photodetector signals, independent of the varied geometries of the algae. Additionally, nine species of algae (Table 1) were measured and similarly examined. The total change in the  $I_{\text{total}}$  signal during each passing specimen (that is, the value of  $h$  in equation 3.5) was recorded from samples of each size of particle and species of algae.

The microspheres had nominal sizes of 5, 10, and 20  $\mu\text{m}$  but in reality each size contained a wide spread of diameters around the nominal mean. Therefore, the actual diameter of each microsphere was measured individually from the photo taken by the system as the sphere passed the sensing region. An MATLAB script was created to automatically perform this task. The channel depth was larger than the depth of focus of the microscope objective, so the processing step also removed poorly-focussed images from consideration, to prevent errors in diameter measurements. After this step, 2994 recorded microsphere datasets remained. The results of the comparison, shown in Figure 22, are presented with the spheres grouped into integer diameters. The microspheres were tested in a mixture of glycerol and water, to prevent their sinking to the bottom of the channel. The data of the microspheres and

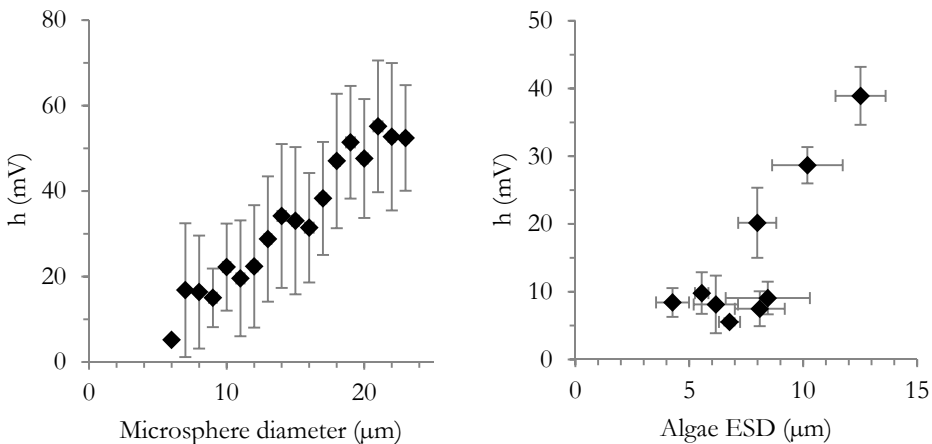


Figure 22. Microsphere (top) and algae (bottom) size compared to  $h$ , the change in total light intensity (as in equation 3.5). The algae equivalent spherical diameters (ESDs) are calculated as an average for the species, rather than by measuring the individual cells as they pass by the sensor.

algae are thus presented separately, as the index of refraction of glycerol is different than that of water.

Monocultures of algae were run through the system, one species at a time, until at least one thousand instances of each species had been recorded. The images were examined to rule out any samples that could not be positively identified as that species with a high degree of certainty. Of the remaining data, 525 samples were chosen at random from each species and the photodiode signals compared to the species size, represented by the average equivalent spherical diameter (ESD) for the species. This value was determined by calculating the volume of 20 cells of the species from microscopy images, and finding an average and standard deviation of the ESD.

This approach had to be used for the algae due to high uncertainties that would be present in the in-channel size measurements. These uncertainties were lower with the microspheres because they were in glycerol which has a higher index of refraction, which led to clearer images.

Both the microsphere and monoculture algae data showed that the average total change in the total intensity photodiode signal  $\max(I_{\text{total}}) - \min(I_{\text{total}})$  closely correlated well with the microsphere diameter or algae ESDs.

## 2.4.5 Overview of classification strategy

The ultimate goal of the system is to identify the species of an individual algal cell as it passes the sensor. To this end, multiple pattern recognition were compared after the sensor data had been pre-processed.

Data pre-processing followed several steps: first, the micrograph of the channel and algae for each dataset was examined to manually identify the algae or particles. Second, several features of the total-intensity and difference signals ( $I_{\text{total}}$  and  $\Delta X$  in Fig. 1) were extracted and subsets of these signal features were used to explore the species recognition capabilities of the system. Both discriminant analysis and neural networks were used for this pattern recognition problem. The resulting classifications could then be compared, on a cell-by-cell basis, with a manual identification of each cell from the photo captured as the cell passed in front of the interrogating laser beam.

This procedure was followed on several different datasets. The first was a dataset consisting of microspheres, intended to predict the size of the sphere from the photodiode signal. The second dataset consisted of 5 mixed algae species, intended to predict the species of each cell. Lastly, a field-collected sample was spiked with

cultured algae, to test the differentiation between the algae and the detritus present in the field sample. The details of the analysis and classification methods are presented in the following chapter.

## 2.5 Optical modelling

As morphologically-complex cells, algae are difficult to model optically on a single-cell basis. However, some of the species used here have relatively simple shapes and can be modelled to some extent. A three-dimensional ray tracing model was used to explore how the variables of algae shape, size, index of refraction, and absorption play a role in the measurements. Furthermore, the models were used to examine the relative effects of these variables and whether they could be distinguished from one another. Lastly, they were used as a first-order approximation of the effects of the algae being located in different parts of the channel cross-section, since this is not controlled in the experiments. The models are based on the algae being represented as combinations of ellipsoids. The rays are refracted at the surface of the algae and absorbed by the algae, depending on their path length.

### 2.5.1 Mathematical and geometrical basis

A refracted ray

$$\mathbf{R} = n\mathbf{I} + (n c_1 - c_2)\mathbf{N} \quad (3.8)$$

depends on the angle of the incident ray,  $\mathbf{I}$  with respect to the incident normal ray  $\mathbf{N}$  and the indices of refraction  $n_1$  and  $n_2$  as in Figure 23 with

$$n = \frac{n_1}{n_2} \quad (3.9)$$

$$c_1 = \mathbf{N} \cdot \mathbf{I} \quad (3.10)$$

$$c_2 = \sqrt{1 - n^2(1 - c_1^2)} \quad (3.11)$$

To identify rays which interact with the algae, we look for the intersections of a ray

$$\mathbf{I} = \mathbf{P} + \mathbf{D}\alpha \quad (3.12)$$

with origin  $\mathbf{P} = (p_x, p_y, p_z)$ , normalized direction  $\mathbf{D} = (d_x, d_y, d_z)$ , and length  $\alpha$  with an ellipsoid which satisfies

$$\frac{(x - c_x)^2}{r_x^2} + \frac{(y - c_y)^2}{r_y^2} + \frac{(z - c_z)^2}{r_z^2} = 1 \quad (3.13)$$

with centre point  $(c_x, c_y, c_z)$  and semi-principal axes of length  $r_x, r_y, r_z$ .

The ellipsoid-ray intersections are defined by the solutions to the system of equations

$$\left\{ \begin{array}{l} p_x + d_x \alpha = x \\ p_y + d_y \alpha = y \\ p_z + d_z \alpha = z \\ \frac{(x - c_x)^2}{r_x^2} + \frac{(y - c_y)^2}{r_y^2} + \frac{(z - c_z)^2}{r_z^2} = 1 \end{array} \right. \quad (3.14)$$

The number of real roots of this system of equations corresponds to the number of intersections, at lengths  $\alpha$  along the line of the ray. The MATLAB function *solve* yields the following solutions for  $\alpha$ :

$$\begin{aligned} \alpha_{1,2} = & - \left[ p_z - (c_z d_z^2 r_x^2 r_y^2 + d_x^2 p_z r_y^2 r_z^2 + d_y^2 p_z r_x^2 r_z^2 + c_x d_x d_z r_y^2 r_z^2 + \right. \\ & c_y d_y d_z r_x^2 r_z^2 - d_x d_z p_x r_y^2 r_z^2 - d_y d_z p_y r_x^2 r_z^2 \pm d_z r_x r_y r_z d_x^2 r_y^2 r_z^2 - \\ & c_x^2 d_z^2 r_y^2 - c_y^2 d_x^2 r_z^2 - c_z^2 d_x^2 r_y^2 - c_z^2 d_y^2 r_x^2 - d_x^2 p_y^2 r_z^2 - \\ & d_x^2 p_z^2 r_y^2 - d_y^2 p_x^2 r_z^2 - d_y^2 p_z^2 r_x^2 - d_z^2 p_x^2 r_y^2 - d_z^2 p_y^2 r_x^2 - c_x^2 d_y^2 r_z^2 + \\ & d_y^2 r_x^2 r_z^2 + d_z^2 r_x^2 r_y^2 + 2c_x d_y^2 p_x r_z^2 + 2c_x d_z^2 p_x r_y^2 + 2c_y d_x^2 p_y r_z^2 + \\ & 2c_y d_z^2 p_y r_x^2 + 2c_z d_x^2 p_z r_y^2 + 2c_z d_y^2 p_z r_x^2 + 2c_x c_y d_x d_y r_z^2 + \\ & 2c_x c_z d_x d_z r_y^2 + 2c_y c_z d_y d_z r_x^2 - 2c_x d_x d_y p_y r_z^2 - 2c_y d_x d_y p_x r_z^2 - \\ & 2c_x d_x d_z p_z r_y^2 - 2c_z d_x d_z p_x r_y^2 - 2c_y d_y d_z p_z r_x^2 - 2c_z d_y d_z p_y r_x^2 + \\ & \left. 2d_x d_y p_x p_y r_z^2 + 2d_x d_z p_x p_z r_y^2 + 2d_y d_z p_y p_z r_x^2 \right]^{\frac{1}{2}} (d_x^2 r_y^2 r_z^2 + \\ & d_y^2 r_x^2 r_z^2 + d_z^2 r_x^2 r_y^2)^{-1} \Big] d_z^{-1} \end{aligned} \quad (3.15)$$

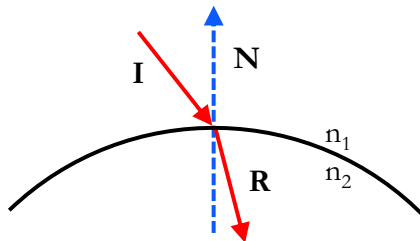


Figure 23. Refraction at a curved surface, to illustrate the equations 3.8 -3.11.

## 2.5.2 Model steps and geometric simplifications

The above two expressions for refraction (3.3) and ray-ellipsoid interactions (3.10) are combined in a three-dimensional model of the system as illustrated in Figure 24. In the model, all non-algae interfaces are ignored; this means the refraction at the surfaces of the channel and the chip are not taken into account, since they should just scale the whole image.

Further, this model ignores the wave properties of light; that is, it does not account for interference of the coherent monochromatic light as a result of its interaction with the algae cell.

The beam's initial intensity is a Gaussian distribution, defined such that the intensity of the beam at  $50\ \mu\text{m}$  from the optical axis is  $1/e$  the intensity at the centre to mimic the actual beam dimensions. Unless otherwise specified, it has  $\text{NA}=0.12$ .

Unless otherwise specified, the algae default to a position in the centre of the channel cross-section, and the distance from the algae to the detector is 1 cm.

### Simulation steps

The overall steps of the simulation allow the user to determine the algae and beam properties, and then traces a large number of rays while moving the algae along the

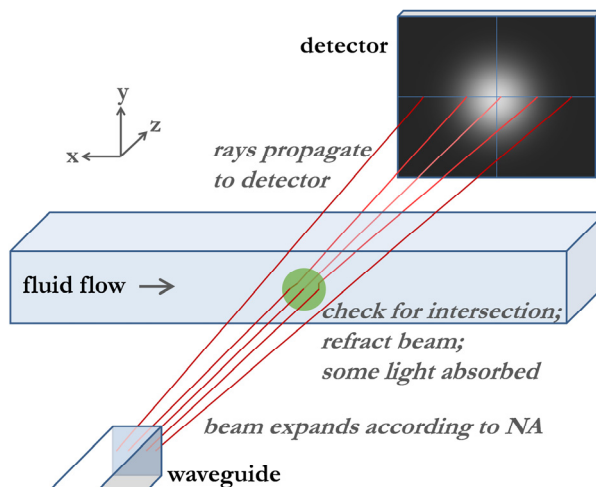


Figure 24. Layout of the modelled system. Note that while the figures shows only rays in one x-z plane for simplicity, the rays are in three dimensions in the calculations and examples shown below.



channel. Specifically:

1. Parameterize algae: user specifies algae position in cross-section and its radius (sphere) or axis lengths (ellipsoid), as well as the algae index of refraction and absorption coefficient.
2. Determine algae's position along the channel length (the position moves by a user-determined step at each repeat of the simulation).
3. For each ray, calculate the ray's intensity depending on its distance from the center of the optical axis of the Gaussian beam. Use equation 3.15 to calculate whether there is a ray-algae interaction.
  - a. If none: propagate the ray in a straight line, and record final intensity & position on a "detector"
  - b. If an algae-ray intersection:
    - i. calculate position of first intersection point
    - ii. refract the ray at that point (ray enters algae)
    - iii. calculate next intersection point; calculate path length inside the algae and decrease ray intensity from absorption
    - iv. refract the ray at that point (ray exits algae)
    - v. free space propagation until detector
    - vi. record the ray's final position & intensity on the detector, with the ray's intensity decreased according to its path length in the algae
    - vii. after all rays have been propagated, calculate the total intensity and differential signals, corresponding to  $I_{\text{total}}$  and  $\Delta X$  in Figure 14.

### 2.5.3 Sample results

#### Ray tracing (demonstrated with a sphere)

A function within the program allows the production of a ray trace for beams on the y-z plane, which can more easily demonstrate the effect of different variables on the model results. Other than the algae position, shape, and optical properties, the user can set several parameters to control the simulation: the spatial resolution of the rays, the beam's numerical aperture, the algae size, and the spatial resolution of the algae movement (Figure 25).

Using a  $6\ \mu\text{m}$  radius sphere as an example yields the signals seen in Figure 26 for total beam intensity  $I_{\text{total}}$  and differential signal  $\Delta X$ . The real part of the index of refraction was taken as 1.4, with the imaginary part, representing the absorption, as indicated on the figure.

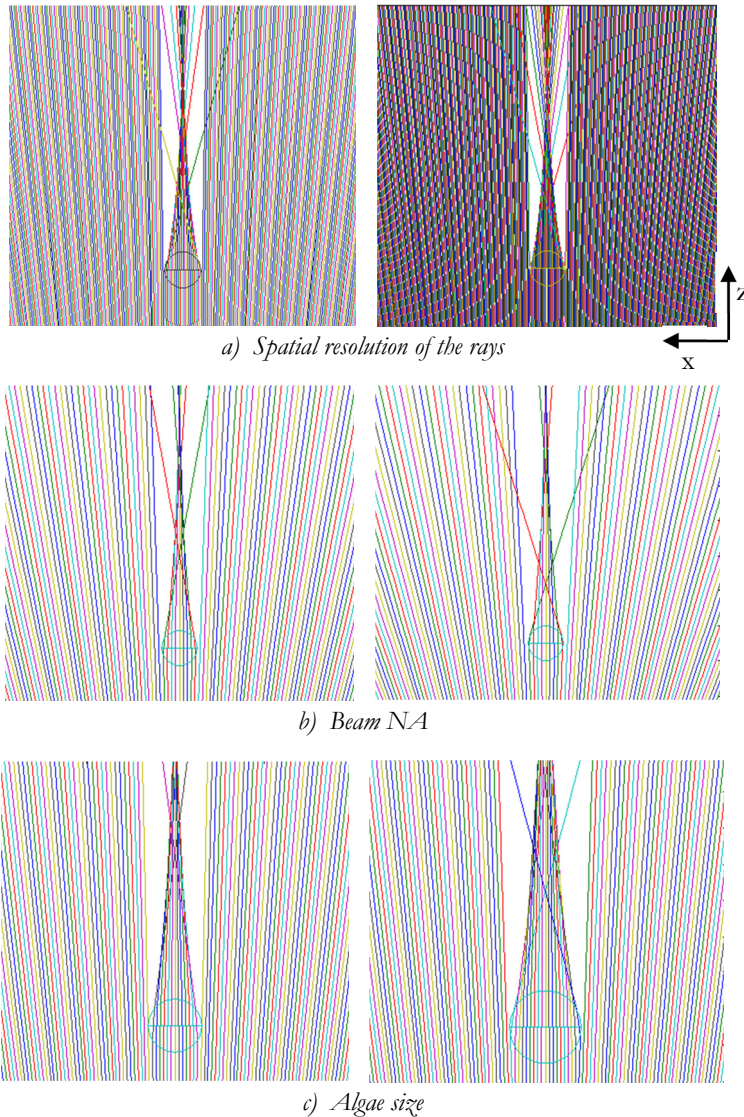


Figure 25. The effects of the modelling parameters set by the user. While the actual simulation results are 3-D, only a 2-D slice of rays is shown for clarity.

The  $\Delta X$  signal does not depend on the amount of absorption, indicating that the main effect here is due to the refraction of the beams; the sphere is essentially acting as a lens, collecting the light and focusing it on the detector segment behind it.

The light intensity signal shows the opposite case: the amount of absorption plays a strong role in the value of  $b$  (the amount of light blocked as the object passes the laser beam, equation 3.5). Logically, spheres that absorb more light affect the intensity more than those which absorb less. An absorbance of zero leads to almost no change in the total intensity signal. This raises the question of how much the optical absorbance of the algal cells will interfere with measurements of the algae morphology.

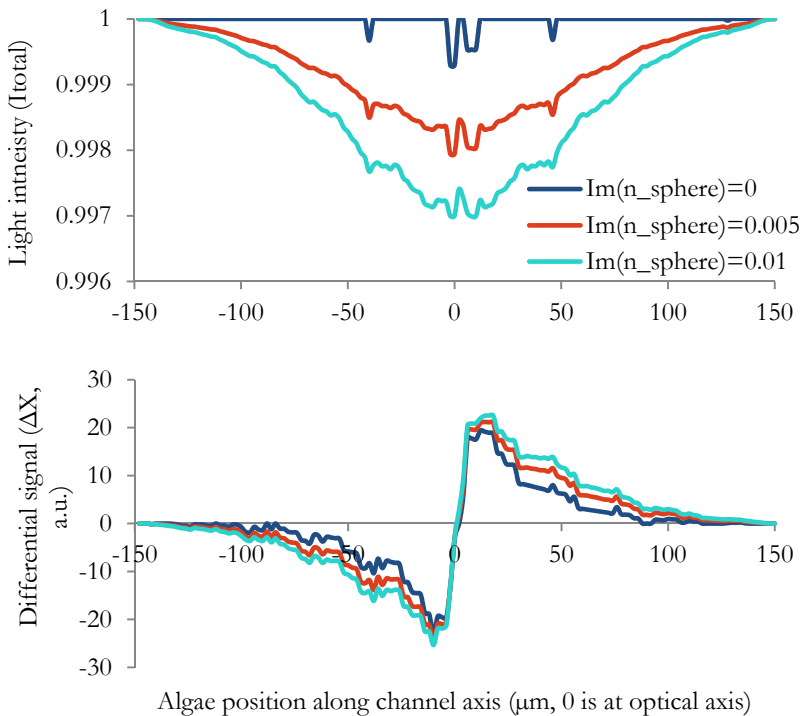


Figure 26. Sample results of the modelled  $I_{\text{total}}$  and  $\Delta X$  signals obtained from a  $6 \mu\text{m}$  sphere. The top plot shows total light intensity dropping as the sphere moves across the beam, with the effect greater for spheres with higher absorption. The bottom plot shows the difference between the upstream and downstream halves of the photodiode, as in Figure 14. Some noise can be seen because of the discrete nature of both the light rays and the algae positioning.

## Comparison of sphere radius and absorption

To compare the effects of algae size and absorption, the model was used to study the total change in light intensity  $b$  created by passing spheres with different properties across the beam (Figure 27). The results show that the two factors interact significantly, and that any attempt to definitively measure algae size with this sensor

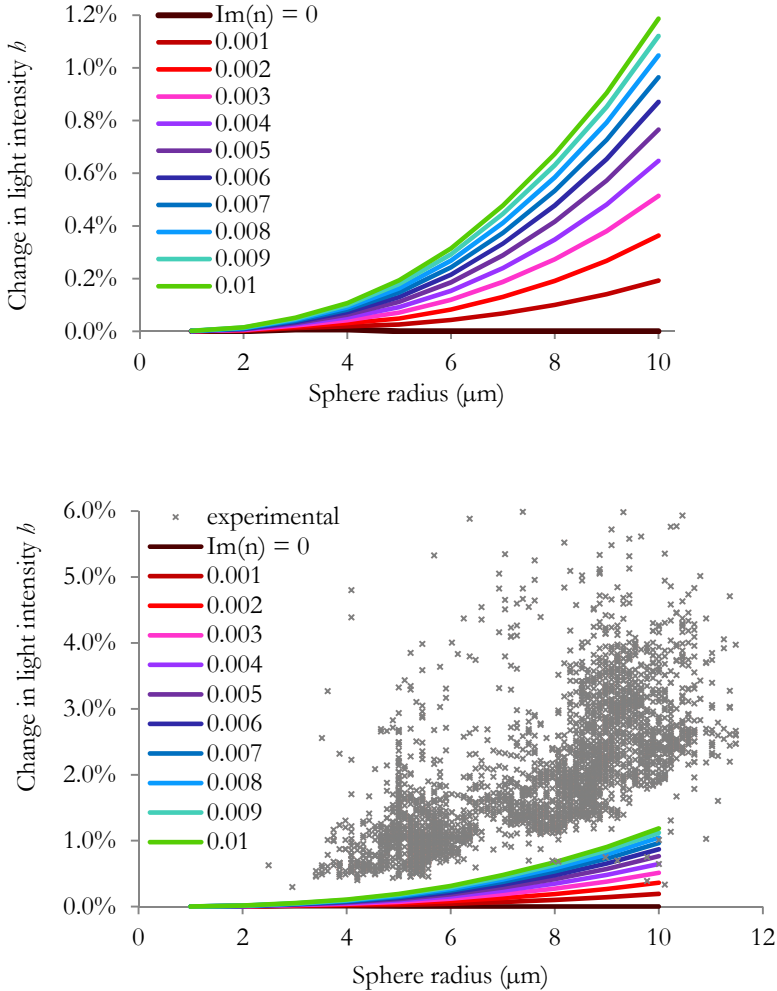


Figure 27. (Top) Normalized change in light intensity  $b$  (*i.e.*  $b$  as in equation 3.5, with the total light intensity set to one) as spheres of  $\text{Re}(n_{\text{sphere}})=1.6$  with various sizes and absorption values traverse the modelled beam. (Bottom) the modelling results compared to experimental values from polystyrene latex (PSL) microspheres,  $\text{Re}(n_{\text{PSL}})=1.6$ .

will be limited in part by the uncertainties in the optical absorption of the species in question.

### Effect of particle position in the channel

It is common in microfluidics to use a focusing technique to force particles to assume a certain position in the channel cross-section. This is often done with flow focusing, where a clean, particle-free sheath fluid enters the main channel on either side of the sample fluid, forcing the sample fluid and particles towards the centre of the channel. The motivation for this can be to keep the particles away from the walls of the channel, or to control their axial speed along the channel. However, this technique does require either a supply of clean water or another actuation system to reliably control the cross-sectional position of the particles, neither of which is desirable in a field-deployable device unless strictly necessary. Because of this, the system presented here has no particle focusing mechanism, and microspheres or algae are free to assume any position in the channel cross-section.

Figure 28 shows the photodetector response (differential signal  $\Delta X$  and the total intensity  $I_{\text{total}}$ ) as a  $5\ \mu\text{m}$  radius sphere moves along the channel, with the sphere in different positions along the channel height.

For both signals, the  $40\ \mu\text{m}$  offset in the channel height causes the signal to decrease

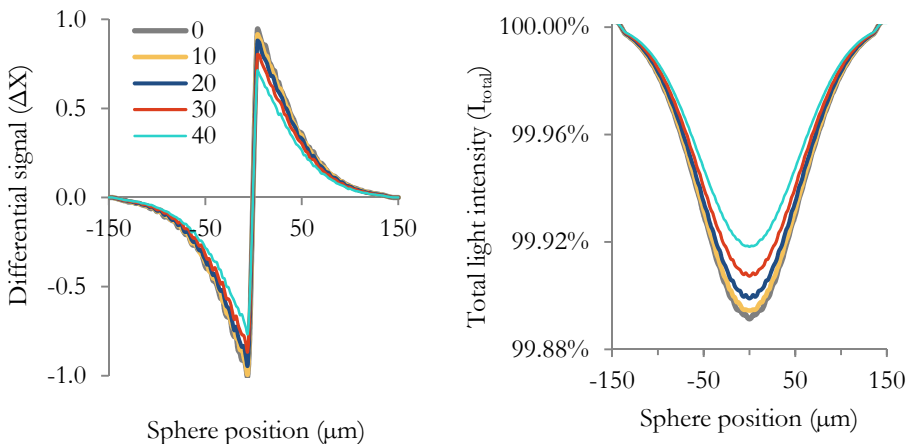


Figure 28. Normalized photodetector signals of a  $5\ \mu\text{m}$  sphere moving along the channel at different heights. The amount of y-offset from the channel centre is indicated in the legend (in  $\mu\text{m}$ ). The bottom axis is the sphere's position along the channel, with 0 the intersection with the optical axis.

to about 75% of its value at no offset. If we compare this effect to that of the sphere radius, we see that the height position causes a decrease in light intensity on the order of the decrease caused by a radius change of one micron (Figure 29). These results suggest that the effect of the particle position is negligible compared to the overall variability in particle or algae size, and that the trade-off of system simplicity for slightly more uncertainty is warranted.

### 2.5.4 Algae modelling

Five species of algae and various sizes of microsphere were modelled using the ray tracing mechanism described above. The five species (see Table 3) were chosen because they could be reasonably modelled with combinations of spheres and ellipsoids.

The index of refraction of the algae was taken as  $n = \text{Re}(n) + \text{Im}(n)$ , with  $\text{Re}(n) = 1.05$  and  $0.005$ . These values are taken from theoretical and experimental studies looking at the inherent optical properties of phytoplankton cells.<sup>41,82,83</sup>

The models show that the total light intensity corresponds reasonably well to the algae models (Figure 30). The modelled differential signals show a clear similarity to the measured signals but lack higher-order features seen in the experiments. From this we can conclude that the refraction and absorption of light, while relevant, is insufficient to fully describe the behaviour of the system during measurements.

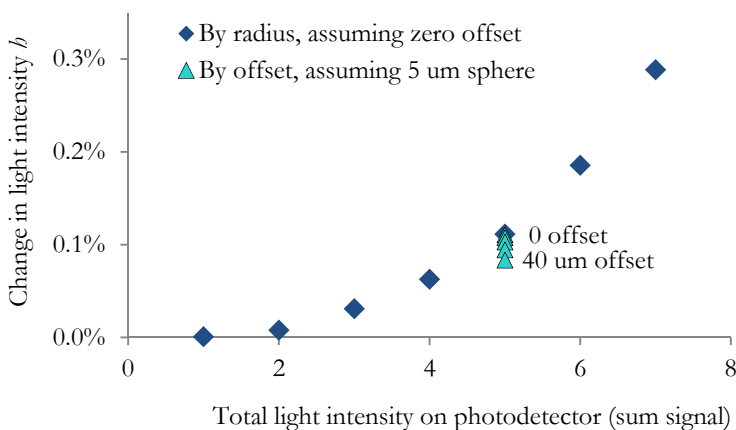

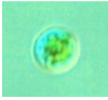

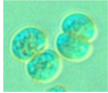
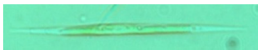



Figure 29. The change in light intensity on the photodetector (as a percentage of the total light intensity) caused by spheres from 1-7  $\mu\text{m}$  radius, compared to a 5  $\mu\text{m}$  radius sphere being offset by 10, 20, 30, and 40  $\mu\text{m}$  in the y-direction.

Table 3. Microspheres and species of algae used in modelling, along with a description of the combinations of spheres and ellipsoids used to model the species.

Species	Picture	Model	Dimensions
polystyrene microsphere		sphere	variable radius
<i>Chlorella</i>		sphere	radius = 3 μm
<i>Cyanothece</i>		ellipsoid	radii = 6, 8, 6 μm
<i>Microcystis</i>		two ellipsoids	radii = 4, 3, 3 μm
<i>Monoraphidium</i>		ellipsoid	radii = 4, 70, 4 μm
<i>Scenedesmus</i>		four ellipsoids	radii = 5, 2, 2 μm

### Limitations of the approach

A more complete model of the algae could perhaps provide further information on which aspects of the cells are affecting which properties of the signals. This in turn might lead to insights about which features of the signals should be used as input to the neural networks for classification. For this to happen, a more complex and refined model of the algae cells themselves would be necessary, and a more complete model of the optics would be required. A model of the algae would need to include detailed optical properties of the internal microscopic and sub-micron features unique to each species. The optical model would need to take into account the wave nature of light, with the wave front distorted by passing through the algae cell. The model would need to account for interference of the coherent monochromatic light as a result of these sub-micron algae features.

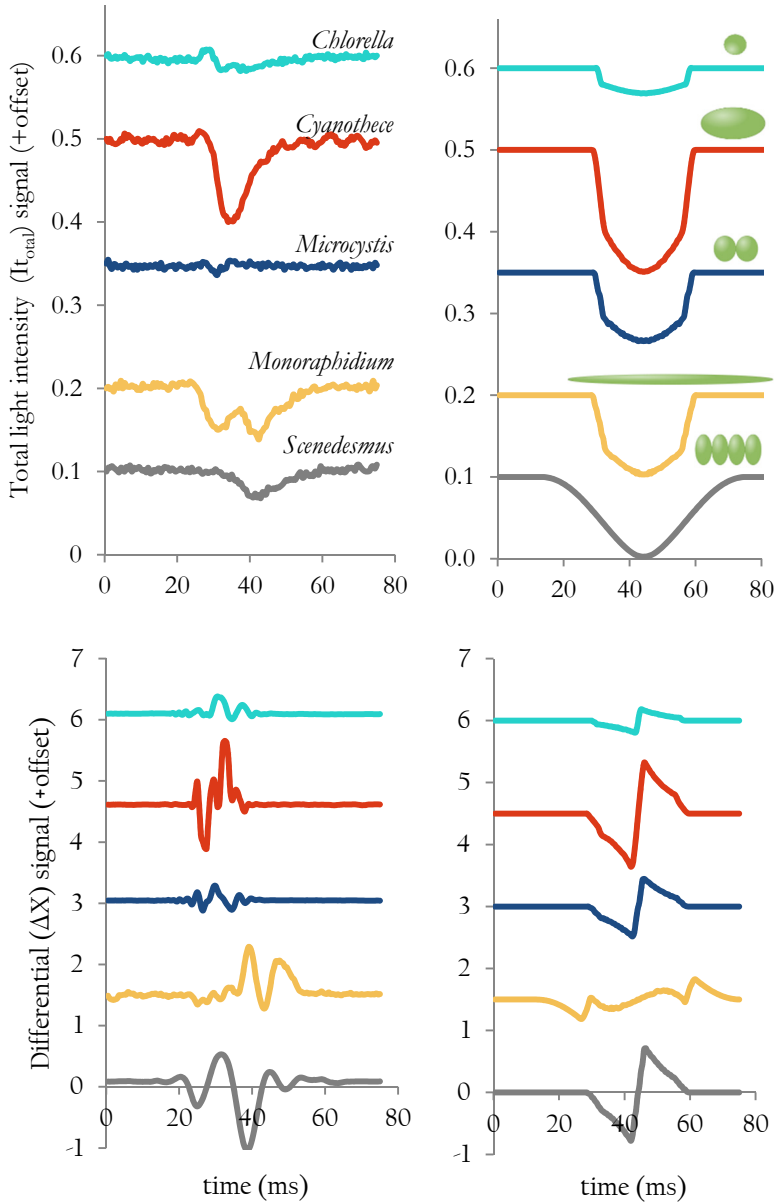


Figure 30. Experimental (left) and modelled (right) sum signals from 5 algae (see Table 3). The signals are on an arbitrary but consistent scale; the green images on the right depict the three-dimensional models of the algae used.



## 2.6 Conclusions

A simple glass device is presented, featuring a sub-surface curved waveguide and a surface microchannel. Light transmitted by the waveguide crosses the channel and is measured with a quadrant photodetector. The system provides optical “fingerprints” of spheres or algae suspended in the flow.

Characterization measurements provide insights into the system’s behaviour under varying conditions. The signal properties change when the flow rate is increased or when user-defined sensitivity thresholds are modified. This suggests that a higher flow speed will require faster data collection than currently being implemented. The laminar flow inherent in microfluidics causes the high-aspect ratio particles to self-align, which increases the repeatability of measurements of highly non-spherical algae species. For example, over 80% of particles with aspect ratios greater than 6 were aligned to within  $10^\circ$  of the channel’s long axis. The total light intensity incident on the detector corresponds well to the sample’s physical size (diameters for spheres, or equivalent spherical diameter for the algae species).

Simple ray-based optical model were created to mimic the system’s measurements. It was found that offsets of the sample in the y-direction cause small errors in size measurements, which is important for a device with no flow focusing. As expected, the optical absorption of the sample greatly affects the total light incident upon the detector. Lastly, some of the algae species were modelled, with their geometries represented as combinations of ellipsoids. These models showed similar overall patterns to those found experimentally, but lacked some of the higher-order features seen in the experiments. More detailed models of the tiny internal features of the algae cells, coupled with a wave-based model of the optics, could potentially yield further insights into which properties of the cells influence the signals. If a model were shown to accurately represent the signals obtained experimentally, perhaps this could even be used to interpret measurements of previously unencountered species.



# 3

Pattern recognition, results,  
and analysis of the optical  
algae identification system

### 3.1 Introduction

The previous chapter discussed the fabrication, design, and characterization of a microfluidic chip for classifying and quantifying algae species in water. Here we study the device performance and classification methods for data analysis. Specifically, the results from two pattern recognition methods are compared: discriminant analysis classification and neural network pattern recognition. Since the neural network yields a higher success rate, its algorithm parameters are subsequently tuned to optimize the classification.

Both methods require the selection of features from the input signal. The algorithms for classification depend on matching these sets of features, rather than matching the shape of the signal itself.<sup>84</sup> For these tests, five metrics were initially selected from each of the two photodiode signals. One was rejected for showing no difference across the different types of samples, leaving four distinct parameters extracted from each photodiode signal: the maximum value, the minimum value, the sum of the signal, and the sum of the signal after it was normalized and rectified. Each algae cell produces two photodiode signals (the  $I_{\text{total}}$  signal and the  $\Delta X$  signal), so there are a total of eight signal features to describe each algae or microsphere recorded (Figure 31).

The discarded feature for the signals was the signal length (in the time domain). If the

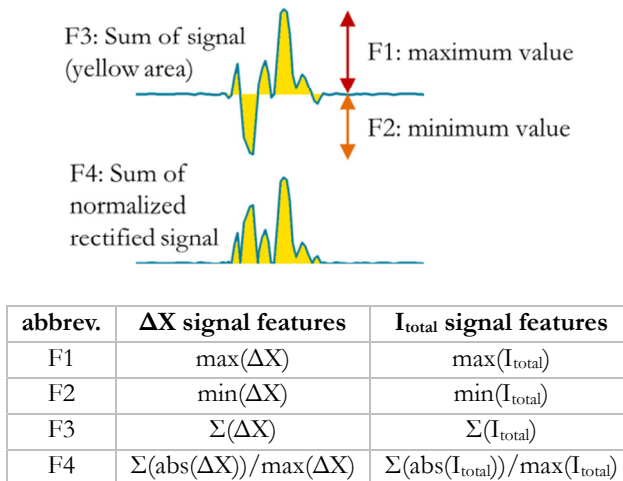


Figure 31. Signal features used as input to the DA and NN pattern recognition systems

particles or algae had been focused to a fixed position in the channel cross-section, the length of each signal might have been a useful measurement of the physical length of the specimen. Since no such focusing was used, the lack of correlation between the signal length in time and the specimen physical length is unsurprising.

## 3.2 Pattern recognition methods

Both discriminant analysis and neural networks are methods for taking a set of inputs and providing a prediction of the correct output value. In the case of algae classification, they take in the signal features mentioned above and output a prediction of the species that created that signal.

Both methods require training before use. In this initial step, a subset of the inputs and the corresponding correct outputs are designated as training data. This data is used to define some function that maps from inputs to outputs. The method is then tested: the remaining input samples are classified by the software. In order to validate the methods and identify the misclassifications, the results are compared to a manual (i.e. human done) classification to characterize the performance of the method. The correct classification is defined, in this case, as the manual identification of the algae species from the photo taken by the system.

### 3.2.1 Discriminant analysis

Discriminant analysis (DA) is a statistical pattern matching method whereby the  $d$  features of a signal are represented as vectors  $x=[x_1, x_2, x_3, \dots x_d]$  in  $d$ -dimensional space. The training data is used to define groups, or clusters, in the  $d$ -dimensional parameter space. The goal of the DA is to classify the unknown test data into the groups that are statistically most likely to belong to. In the most intuitive application, using Euclidean distances, the DA method could identify the mean position of all the groups in the  $d$ -dimensional space, and then classify an unknown vector as belonging to the group whose mean it is closest to. More complex approaches allow for non-linear methods of determining the group membership. An example is using Mahalanobis distances, which generalizes this idea by defining “distance” in terms of how many standard deviations a point is from a mean, rather than using absolute distance.<sup>85</sup>

In this work, we use the Mahalanobis distances and the built-in discriminant analysis tool (the “classify” command) of MATLAB (R2010b, The MathWorks) to do DA classification. 70% of the data from each group is used for training. The remaining

30% is treated as unknown, and is classified and then evaluated. These values were chosen to be comparable with the split of data used in the neural networks (next section).

### 3.2.2 Neural networks

Inspired by biological neurons, artificial neural networks (NN) are used for pattern recognition or machine learning. For supervised pattern recognition, the goal of the system is to find some mapping which produces the desired output values given a set of inputs. The NN approach allows for a more complex, adaptive, non-linear weighting of the various signal features than discriminant analysis, often yielding better results.<sup>84</sup>

An NN uses a multi-layered network to link the input vectors with their intended output values (Figure 32). The network consists of three layers: input, hidden, and output layers. The input layer transmits a signal to the hidden layer, where the input is weighted and/or transformed in a series of hidden neurons. The output layer receives the results of the hidden layer and assigns the signal to an associated group.

The training step is used to adjust the hidden layer to optimize the mapping from input to output by minimizing the output errors. This process is iterative, and the algorithm used to update the weights and transformations can have a significant effect

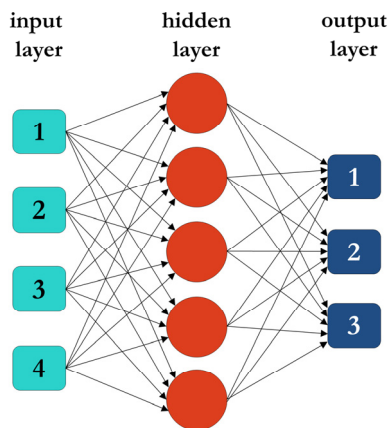


Figure 32. Schematic overview of a neural network architecture. Four input parameters (equivalent to our signal features) are fed into a hidden layer with 5 neurons. They are recombined in the output layer which has three classes. Each of three classes is assigned a value based on the hidden layer results; the class with the highest value is the predicted species of the sample.

on the results.

We initially use the neural network pattern recognition tool (the *nprtool* command) of MATLAB with the default settings to do classification. With this tool, the fraction of data to be considered training, validation, and unknown data can be selected by the user; we use 60%, 10%, and 30% respectively, and use a network with 10 hidden neurons. A rule of thumb in neural networks is that the number of examples from each group in the training data should be about 5-10 times as high as the number of features. Otherwise, over-training can occur. Since 8 features are being used, assigning 60% of the data to training fulfils this criterion, though more data in the training group could be beneficial. However, these values were used in the interests of having a large enough number of unknown samples for statistical analysis. A discussion of avoiding over-training will be included in the neural network optimization process (section 3.4).

### 3.3 Results: Neural networks vs. discriminant analysis

#### 3.3.1 Test 1: Sizes of microspheres

The first dataset contained a mixture of microspheres, of nominal diameters 5  $\mu\text{m}$ , 10  $\mu\text{m}$ , and 20  $\mu\text{m}$ . The actual diameters were measured from micrographs taken before the experiments; the measured diameters (mean  $\pm$  standard deviation) were  $6.15 \pm 0.52 \mu\text{m}$ ,  $11.05 \pm 0.26 \mu\text{m}$ , and  $20.20 \pm 1.25 \mu\text{m}$ . Data was only included in the sample set if the associated photo was sufficiently well-focused that the microsphere's diameter could be determined from the picture. A total of 983 microspheres were successfully sampled, with 182, 496, and 305 microspheres of 5, 10, and 20  $\mu\text{m}$  diameters, respectively.

The rate of successful identification overall was 85% with the NN, and 77% with the DA, as shown in Figure 33. The largest difference between the two methods was seen with the 20  $\mu\text{m}$  microspheres; only 42% of the actual 20  $\mu\text{m}$  microspheres were identified as such by the DA.

An examination of just two of the signal features – the sum of the  $\Delta X$  signal and the sum of the  $I_{\text{total}}$  signal for each microsphere occurrence shows that while the mean values of these two features may differ by size, they exhibit significant overlap (Figure 34). Examining some of the other features (data not shown) shows a similar

situation – different microsphere sizes have different mean values, but significant overlap. While the use of all eight features is intended to provide better classification

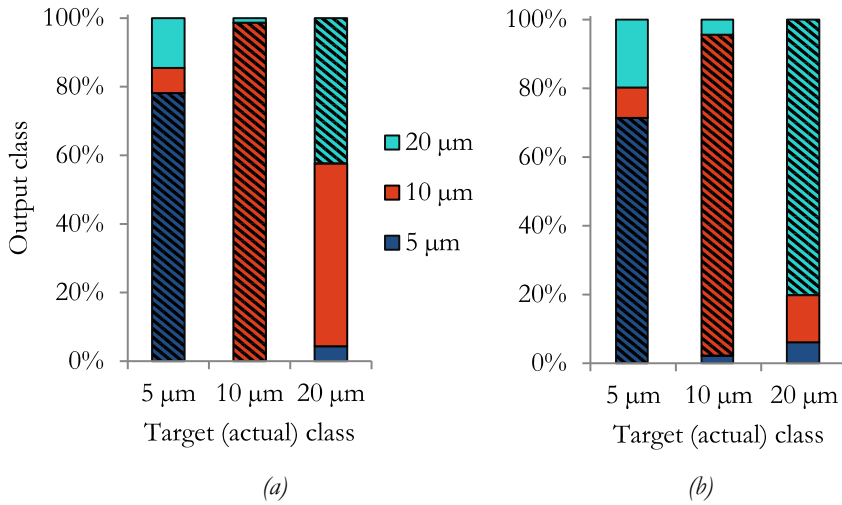


Figure 33. Results of (a) discriminant analysis and (b) neural network classification of microspheres by size. The horizontal axes represent the real size of the microspheres, as identified manually from the photographs taken during experiments, while the vertical axes are the output classes returned by the pattern recognition analyses. The areas marked with diagonal stripes indicate correct classifications; i.e., output class = target class.

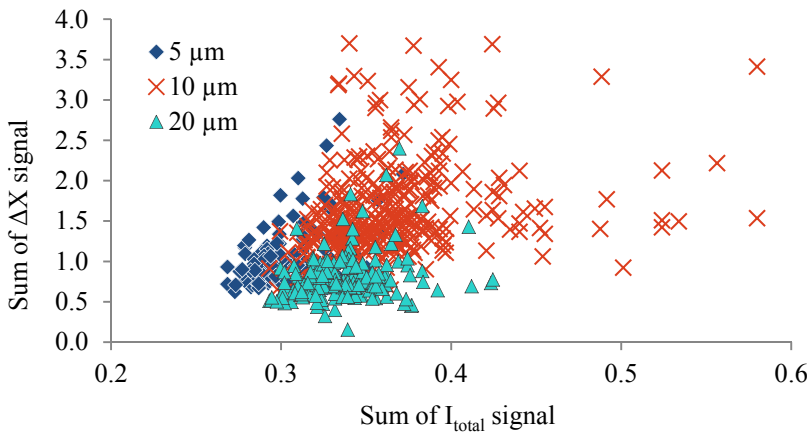


Figure 34. Plot of the sum of the  $I_{\text{total}}$  signal versus the sum of the  $\Delta X$  signal for each microsphere occurrence. This sample data shows significant overlap between the groups, and serves as an example of why discriminant analysis may not be sufficient for classification.



results than using merely two, the results nonetheless suggest that even in the eight-dimensional feature space used by the DA, there is too much overlap between the different groups, particularly the 10  $\mu\text{m}$  and 20  $\mu\text{m}$  spheres, to distinguish them by these parameters alone.

### 3.3.2 Test 2: *Cyanothece* & detritus

The second dataset used to test the microchip and classification algorithms was designed to mimic the conditions in a field test. Water was collected from the slow-moving Dommel River, which passes through the campus of the Eindhoven University of Technology. It was filtered to remove all particles above 100  $\mu\text{m}$  (to avoid clogging the microchannel), and lab-cultured *Cyanothece* cells were added to the water.

This dataset was chosen to characterize the system's ability to distinguish the toxin-producing cyanobacteria from surrounding detritus and other algae, in an attempt to simulate the conditions of a cyanobacteria bloom. A compound micrograph (containing images of cells from multiple separate micrographs) of the solution is shown in Figure 35. The green ellipsoidal *Cyanothece* can be visibly distinguished from the detritus, which exhibit a wide array of morphology and which even includes other types of algae. In total, 106 *Cyanothece* cells and 216 pieces of detritus were sampled.

The results of this classification were quite successful, with the NN and DA methods yielding correct identifications 95% and 94% respectively. For the NN, 8.6% of the



Figure 35. Detritus from the Dommel River mixed with lab-cultured *Cyanothece* (green ellipsoids). Scale bar is 100  $\mu\text{m}$  long.

specimens classified as *Cyanothece* were, in fact, false positives, while 3.2% of the specimens classified as detritus were false negatives. The DA yielded no false negatives, but 15.8% of the *Cyanothece* classifications were false positives.

To conclusively decide between these two approaches for this particular type of test, more types of detritus and a larger number of samples would be necessary. These preliminary data reveal an interesting difference between the classification methods: while the NN method yields more average successful classifications, it also has a higher rate of false negatives. In some situations, it might be more desirable to choose settings which yield more false positives than false negatives or vice versa. For example, it might be deemed preferable to overestimate rather than underestimate the actual number of toxin-producing cyanobacteria. On the other hand, false positives may be an expensive error in settings like aquaculture or regulatory compliance monitoring.

### 3.3.3 Test 3: five mixed algae species

The third dataset was based on a sample containing a mixture of four phytoplankton and one cyanobacterium. The species were *Cyanothece aeruginosa*, *Chlorella vulgaris*, *Microcystis viridis*, *Anabaenopsis sp.*, and *Monoraphidium griffithii*. The cell sizes of these species range from a few microns (*Chlorella*) to the tens of microns (*Cyanothece* and *Monoraphidium*). These species were chosen out of the nine available species primarily because they were distinctive enough to be reliably identified. The *Navicula*, *Pseudokirchneriella*, and *Pseudanabaena* are all very small, difficult to distinguish with the microscopy system on the detector platform, and have lower signal-to-noise ratios than most of the other species. The *Scenedesmus* was left out because there is a very high variability in that species over its growth cycle. An examination of that species at the time of the experiments showed that the cells were quite polydisperse, and that it would probably need to be treated as two different groups from the classification point of view.

The five species were mixed together and run through the sensor until there were over 1000 datasets collected. The species of each sample was manually identified from the photo; if the photo was too unclear to identify certainly it was removed from the dataset to ensure a careful analysis of the neural network results. The data from the first ~100 cells of each species comprised the dataset, for a total of 509 samples. The rate of successful identification for all five species was on average 78% with the NN, and 67% with the DA, shown in Figure 36.

Both methods had low success (<50%) with the *Chlorella*, and the DA had even worse results with *Microcystis*. These two species are the smallest of the five, and they had lower signal-to-noise ratios than the other species. To illustrate this, the signal-to-noise ratio (SNR) of the *Chlorella* and *Cyanothece* was calculated with the  $I_{\text{total}}$  signal for each sample. The SNR was defined as the ratio of the minimum value of the signal to the RMS value of the noise. For the *Chlorella* the average SNR was 8.7 and for the *Cyanothece* 56.4. This is likely a contributing factor to their lower classification rates. This hypothesis is supported by the fact that the misclassified *Chlorella* (NN & DA) and *Microcystis* (DA) were almost all misclassified as each other or as *Monoraphidium*, the third-smallest species.

This suggests that for higher-accuracy classification of small (<7  $\mu\text{m}$  equivalent diameter) algae, there may be other signal features which lend themselves to the

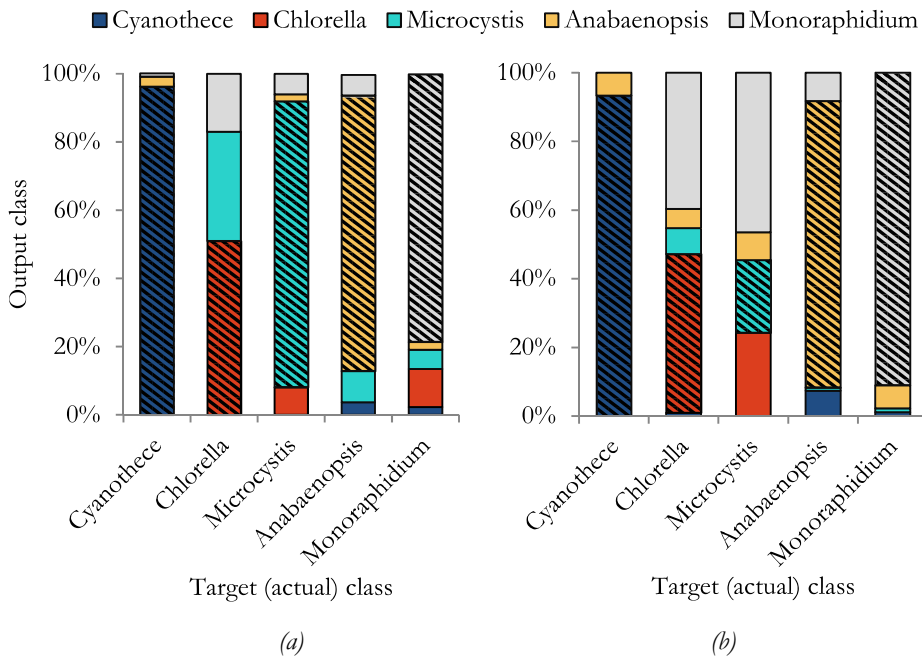


Figure 36. Results of (a) neural network and (b) discriminant analysis classification of a mixture of five algae species, based on the eight signal features obtained from the photodiode signals collected during each algae occurrence. The horizontal axes represent the real species, as identified manually from the photographs taken during experiments, while the vertical axes are the output classes returned by the pattern recognition analyses. The areas marked with diagonal stripes indicate correct classifications; i.e., output class = target class.

distinguishing of these species. It would be beneficial to use a smaller microchannel and laser beam to illuminate the channel, to increase the proportion of light affected by these small samples. Using a smaller wavelength of light might also help; this would require a smaller waveguide in order to maintain single-mode transmission.

## 3.4 Neural network optimization

While the default values of the *nprtool* yield promising results, there are several variables which can be manipulated to optimize the neural network performance. In the following section, each variable was changed and then tested 10 times with the same dataset (5 mixed algae species). Each time that the test was run, the input data was randomly re-assigned to be training, validation, or test data, in order to see if the new set of variables was susceptible to over-training to a certain set of test data. The results present the percentage of the test data that was correctly identified, with the bar height showing the mean of the 10 tests and the error bars showing the standard deviation. Ideally we want the method with the highest mean and a low standard deviation, which means that the method is both accurate and robust against random initial training conditions. Note that by default, MATLAB shows the final classification of all of the data (including the training and validation data), and in the previous section this is what was shown. However, in the following sections only the results of the “test” data are shown, as it represents a more difficult task that is more representative of real usage.

### 3.4.1 Training algorithm

The training algorithms determine how the weights and bias values of the hidden neurons are updated. There are 12 options for training algorithm functions appropriate to pattern recognition available with MATLAB’s Neural Network toolbox, listed in Table 4; the number of hidden neurons and other variables were kept constant at the default values.

The functions *trainbr*, *trainrp*, *trainlm*, and *trainr* all showed high success rates and low standard deviations (Figure 37). The *trainscg* method, which is the default, showed high variability. The *trainr* method took one to two orders of magnitude more time to train than the other three high-performing methods, so it will be excluded from further analysis.

Table 4. Available training algorithms and function names

Function	Algorithm
trainbfg	BFGS quasi-Newton backpropagation
trainbr	Bayesian regularization backpropagation
traincgb	Conjugate gradient backpropagation with Powell/Beale Restarts
traincgf	Conjugate gradient backpropagation with Fletcher-Reeves updates
traincgp	Conjugate gradient backpropagation Polak-Ribière updates
traingd	Gradient descent backpropagation
traingdm	Gradient descent with momentum backpropagation
traingdx	Gradient descent with momentum and adaptive learning rate backpropagation
trainlm	Levenberg-Marquardt backpropagation
trainoss	One step secant backpropagation
trainrp	Resilient backpropagation
trainscg	Scaled conjugate gradient backpropagation ( <i>the default method</i> )

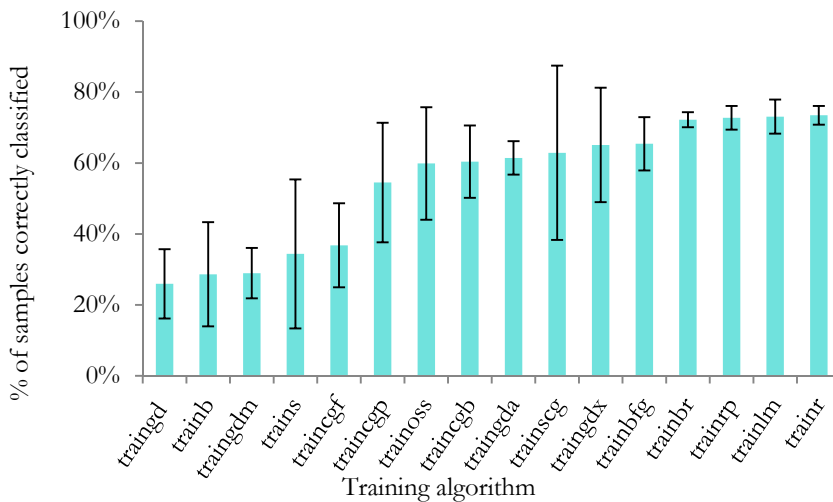


Figure 37. Percent of correctly classified samples from a sample with 5 mixed algae species, depending on the training algorithm. The error bars are the result of the analysis being run 10 times with each method, with a randomly-selected subset of data used for training, validation, and classification each time.

### 3.4.2 Number of hidden neurons

The default training method (*trainscg*) and the three highest-performing methods (except for *trainr*) were used to test the effect of the number of hidden neurons. In each case, increasing the number of neurons improved the results up to a point at which the success rate more or less plateaued (Figure 38). *Trainlm* was the quickest to hit this plateau at only 2 hidden neurons; the default *trainscg* saw little improvement with more than 3 neurons. *Trainbr* and *trainrp* both improved rapidly until the 10 hidden neuron mark, with *trainbr* having the highest success rate and lowest variability at 50 neurons.

### 3.4.3 Performance function and regularization parameter

The performance of a neural network must be evaluated at each iterative step in order to improve. There are four options for how a network's performance is measured. In each case this is done with a calculation of the error of the network, but the method by which the error is calculated is different. The four methods available are the mean squared normalized error (MSE), the sum squared error (SSE), the mean absolute error (MAE), and the sum of absolute errors (SAE). The latter two methods underperform compared the other two and are not available for all training methods, and so are discarded as options. The MSE option performed as well or better than

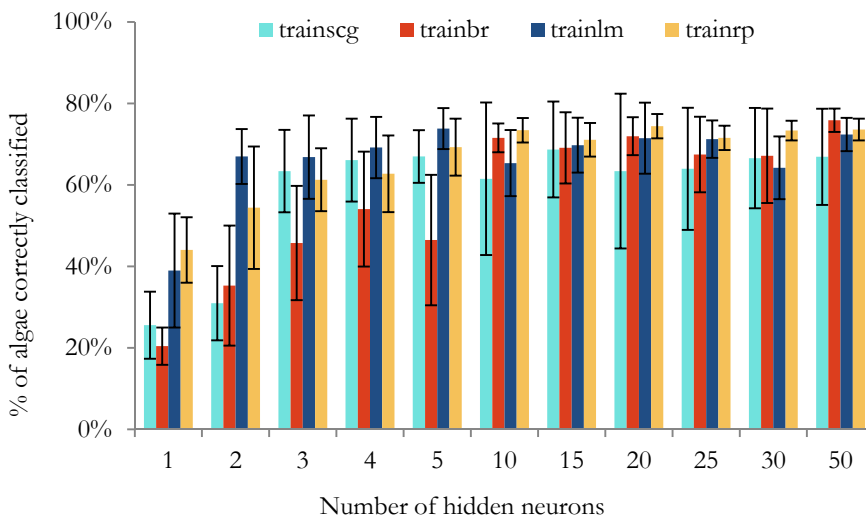


Figure 38. Percentage of correctly classified algae from the mixture of 5 species, using various numbers of hidden neurons with four of the top training methods.

SSE for all of the top performance functions (*trainbr*, *trainlm*, *trainrp*) and can be used for all three of them, so it is selected as the default.

The MSE performance function is, by default, simply a sum of the errors squared. However, it also allows manipulation of a regularization parameter which penalizes high weight values in the network. If the regularization parameter is not zero, the values of the weights themselves are also a factor in the error calculation. Including this term helps to prevent over-training specific to a set of training data. The results of changing the regularization parameter are shown in Figure 39; the *trainbr* method already includes an automated optimization of this parameter and it is thus not included in the figure.

Increasing the regularization parameter has the most effect on the default *trainscg* method, where it increases the performance of the network significantly. The *trainrp* method shows a very slight improvement up to the 0.1 level, and then both it and the *trainlm* algorithms decrease in performance rapidly.

### 3.4.4 Trade-off between certainty and samples identified

A neural network outputs a matrix containing values which are analogous to posterior probabilities – an array of values which indicate the relative likelihood that a sample is a member of a given class. By default, each sample is assigned to the class with the highest output value. The values range from 0 to 1. In this test, the class is only

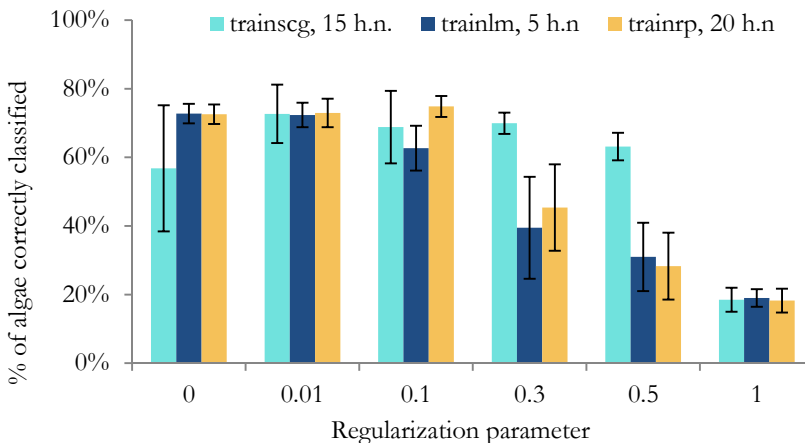


Figure 39. Effect of the regularization parameter in the MSE error performance function. The default value is 0; higher values cause the network to penalize large weights and biases in the network.

definitively assigned if the output value of the highest-probability class is above a threshold value. This is conceptually equivalent to requiring a specified level of certainty before assigning a species to a sample. This behaviour can also be manipulated to bias the network towards, for example, preferring false negatives over false positives.

The results (Figure 40) show that *trainbr* returns results with high certainty: even if the required certainty goes from 0.05 to 0.9, the percentage of results classified and the percentage of correct classifications remain nearly constant. The other three methods show dramatic drop-offs in the number of classified samples as the certainty threshold increases above 0.5.

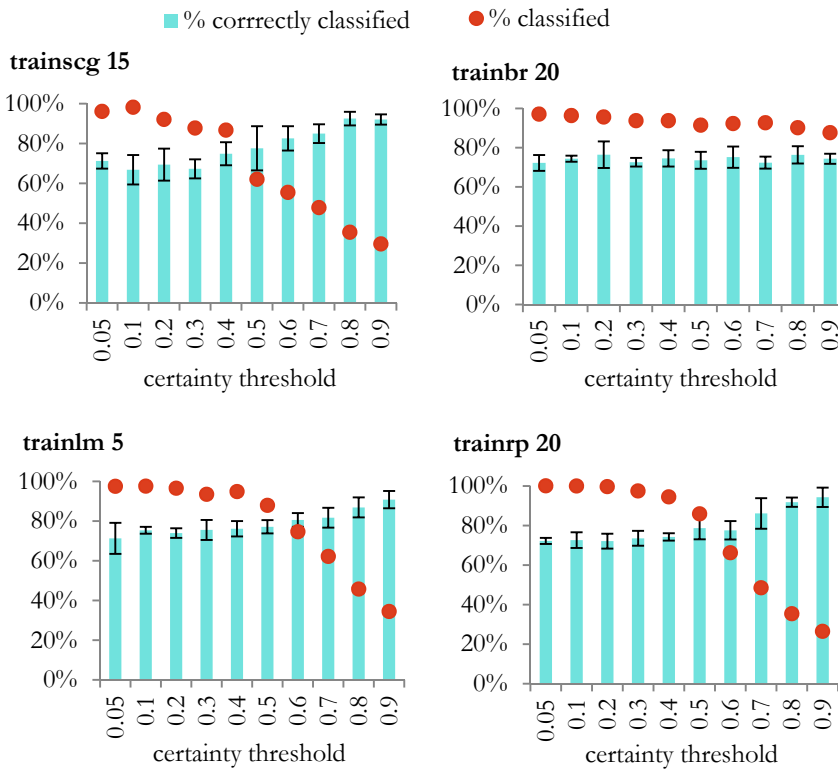


Figure 40. The results of the imposition of a “certainty threshold” in the neural network results: a higher certainty requirement leads to fewer specimens being classified. The label on the top left of each plot indicates the training method and number of hidden neurons.



### 3.4.5 Best classification results

The best result obtained during these procedures was with the method *trainbr* with 50 hidden neurons, using the *mse* performance function. This combination resulted in  $75.9\% \pm 2.9\%$  of the algae in a sample of 5 mixed species being correctly classified. This value reports only the percentage of correctly identified specimens from the test data, and does not include the data used to train and validate the network. With those data included, the success rate is  $91.0\% \pm 1\%$ . A breakdown of the classification results by species is shown in Figure 41.

For comparison, the default settings (*trainseg* with 20 hidden neurons, *mse* performance function) result in  $61.5\% \pm 18.7\%$  of the test algae being correctly classified. With the training and validation data included, the default settings result in  $69\% \pm 7.8\%$  correct classifications. Figure 42 shows an overview of all of the results obtained by the top three training methods, along with the default method, for various parameters.

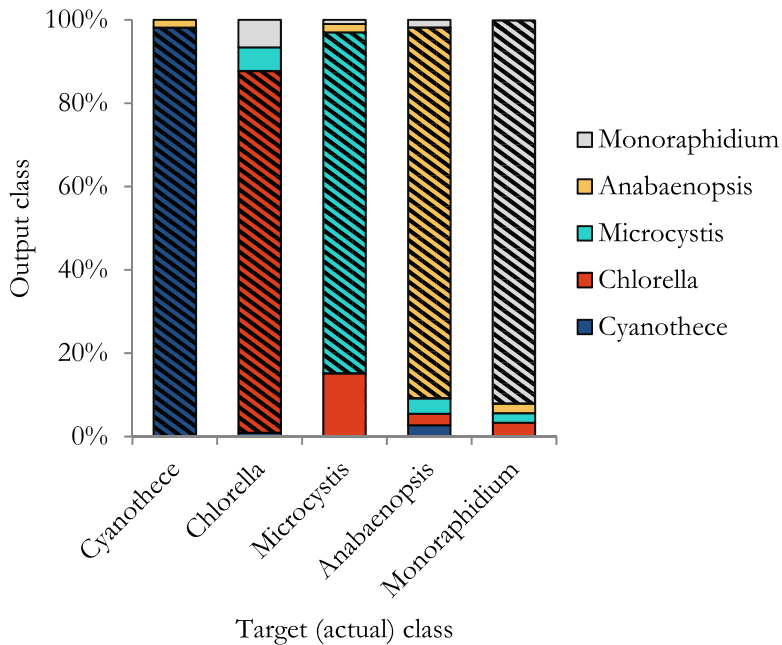


Figure 41. Results of the classification of five mixed species of algae, with the optimized neural network. These data can be directly compared to those in Figure 36, where the results from the default NN settings are shown. The horizontal axes represent the real species of the algae, while the vertical axes are the output classes returned by the NN analysis. The areas marked with diagonal stripes indicate correct classifications; i.e., output class = target class.

### 3.5 Discussion

For each of the datasets, the NN classification gave better average results than the DA classification. This is a trend seen in other works requiring pattern recognition, for example, the analysis of data from an electronic tongue<sup>86</sup>, the classification of medical data from clinical laboratory studies<sup>87</sup>, predicting pollen season severity<sup>88</sup>, and modelling fish species distributions.<sup>89</sup>

A benefit of both of these signal-feature-based methods is that data from other sensors which may be added onto the device in the future (including sensors that give off only one data point per algae, such as the ratio of emitted fluorescence at two different wavelengths) can be incorporated fairly seamlessly into the data handling and pattern recognition.

However, one major disadvantage to the signal-feature-based methods lies in the selection of features to use. To identify the best subset of  $m$  parameters out of a possible  $d$  parameters, one of several algorithms can be followed with no guarantee of finding the actual optimum. To identify the true optimum, it would be necessary to run the neural network again for each possible combination of features, for each possible value of  $m$ , requiring  $2^d-1$  separate training and classification procedures.

The rule of thumb mentioned in the neural network introduction was to keep the number of features less than around 1/5 or 1/10 the number of training samples; otherwise, over-training can occur and decrease the overall performance of the

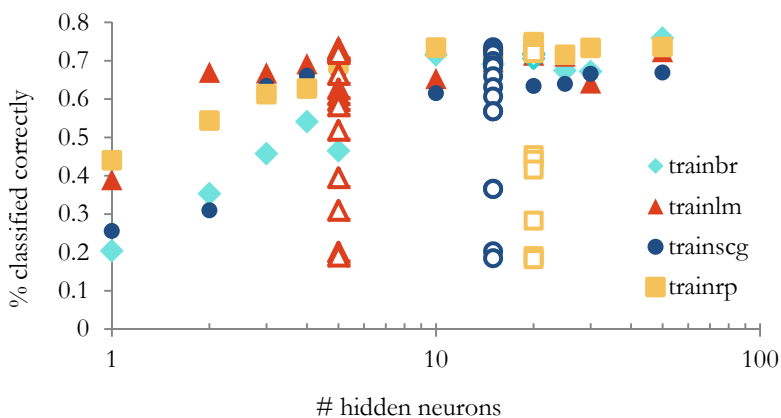


Figure 42. Results from the three top-performing training methods and the default training method. The solid marker represent the best performance at that number of neurons, with the hollow markers showing results from other sets of parameters.

classification method. To ensure that we were not over-training the classification, the neural network analysis was repeated multiple times, each time removing a different one of the eight features to see if removing one feature improved the performance. This test was completed only with the five mixed species (dataset 2), since it had the lowest average number of training data sets per type of specimen. This procedure showed that the average classification performance did not improve upon removing any of the features, so all eight features were left in for the analyses.

## Neural network optimization

The optimization process provides a clear improvement in the percentage of algae correctly classified. It also significantly improves the repeatability of the classification results when a different random subset of the data is selected for training and validation. The best method found (*trainbr* with 50 hidden neurons) yields a 23% (14 percentage points) higher success rate than the default values. The most significant change from the default settings (Figure 36) is in the classification of the *Chlorella*. These cells have a low signal-to-noise ratio compared to the other four species, and the default NN is not able to handle this well.

The *trainbr* algorithm includes a process to automatically optimize the regularization parameter, which, as described in section 3.4.3, helps to prevent over-training. This likely contributes to the high success rates of this approach; the algae data is inherently noisy, an inevitable result of the variations between cells of the same species. Additionally, the rule of thumb that suggests having at least 5-10 times as much training data per group as features is satisfied, but not by a large margin – there are between 5 and 10 times as many training datasets as features in the 5 mixed species case. Both of these facts suggest that there may be some susceptibility to over-training in this task, and that the *trainbr* algorithm's success is likely due at least in part to its robustness against this problem.

## Alternative pattern recognition methods

Two approaches to pattern recognition were presented here, each a common technique used in similar situations, but other techniques for pattern recognition may offer advantages or alternative benefits. For example, both of the techniques presented here require initial training data, placing them in the class of *supervised* pattern recognition techniques. *Unsupervised* pattern recognition techniques, in comparison, are designed to form the groups in the first place. This can be done by identifying data clusters according to criteria chosen by the designer, who can select how similar data must be to be considered a group. This approach can, of course,

over- or under-estimate the total number of groups, but it has the major advantage of not requiring prior knowledge of the types of organisms being encountered by the device. For a field-deployable device, using a pattern recognition method that can be transformed to an unsupervised method is advantageous. Unsupervised learning has been used in both neural network and discriminant analysis classification methods.<sup>84,86</sup>

### Wavelet matching

Wavelet matching is a possible complementary approach for this problem, in which the actual shape of the signal (rather than selected representative features) is matched. This is done through a convolution process, whereby a set of signals (wavelets) are convolved against a test signal to see which provides the best overlap. Each wavelet shape is convolved multiple times against the same test signal, but with different scaling in the time and amplitude axes. This approach is useful particularly for very noisy signals, but requires that each sample in a set have the same overall shape. It is limited, though, by requiring an initial set of wavelets to match the sample data to. This means that wavelet analysis alone would not be adequate for an unsupervised learning method, although it would be possible to use the correlation of a signal to a wavelet as a feature input into a neural network or discriminant analysis pattern recognition system.

## 3.6 Conclusions

The use of neural networks (NN) for classification proved more successful than discriminant analysis (DA) in each of the datasets examined here. The performance gap between the DA and NN increased for more complicated problems: when only two groups (*Cyanobesce* & detritus) were present, the NN results were nearly identical to the DA's. With three groups (three sizes of microspheres) tested, the NN outperformed the DA by 8 percentage points. In the test with five groups (five species of algae) the optimized NN's rate of successful classification was 24 percentage points higher than the DA's.

The neural network performance was optimized by exploring the use of different numbers of neurons and training algorithms; the best results were obtained by an algorithm which is inherently non-susceptible to overtraining (*trainbr*). In addition to having the highest average correct classifications, the best results from *trainbr* also had one of the lowest standard deviations, meaning that it had highly repeatable results

even when a different random subset of the data was used for training. Furthermore, it yielded a high certainty compared to the other methods.

This data analysis, coupled with the monolithic optofluidic chip presented in the previous chapter, yields data suitable for the classification of microspheres and algae. It can provide sufficient information for the classification of five different algae species with 76% accuracy when only the test subset of the data is included, and 91% when all data is included. Its promise as a field-deployable device was demonstrated by a success rate of over 90% in distinguishing between cyanobacteria and field-collected detritus.



# 4

Sorting algae with  
optical and fluidic forces

## 4.1 Motivation: Phylogenetics vs phenetics

Taxonomy – the classification of living organisms – is a means of classifying and organizing species to express their relationships with other species or organisms. There are two approaches to algae taxonomy: phenetics and phylogenetics. *Phenetics* groups organisms with similarities in observable traits like morphology (shape, size, patterns, etc.). *Phylogenetics*, on the other hand, is based on molecular (typically genetic) analysis and aims to classify species based on their evolutionary relationship. Various algae taxa have been presented over the years, based on one or both of these approaches.

Each of these approaches offers value in different applications. Phylogenetic classification may be useful particularly to researchers trying to understand the complex relationships between species, their environments, and evolution. However, the genetic or evolutionary background of a particular algae species does not necessarily correspond to predictable behaviour or responses to environmental stimuli. There can be species which are quite far apart on a phylogenetic tree which nevertheless exhibit very similar behaviours or appearances, and which thrive (sometimes together) under similar conditions. For applications like predicting and measuring planktonic blooms, a phenetic approach may yield more useful information while being technically simpler.

A technological approach to algae identification which responds primarily to the cell morphology would serve many purposes within the phycological community. To this end, this chapter looks at size- or shape-sensitive particle sorting methods. After a review of some classification schemes using morphological data, an overview of some existing passive sorting techniques are presented. Two methods are chosen and compared: optofluidic sorting with a laser beam, and inertial sorting in a spiral microchannel. This work is intended to complement the size- and shape-sensitive optical identification methods presented previously in this thesis.

### 4.1.1 Phenetic classification schemes

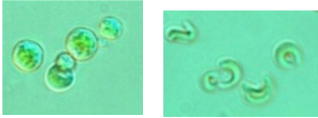
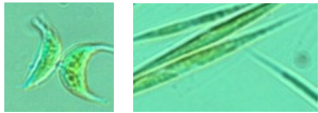
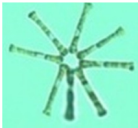
Interest in phenetic classification of algae has recently enjoyed a resurgence, triggered by a paper by Reynolds et al in 2002 which followed up on work by their group from the 1980's on.<sup>90</sup> A few phenetic classification schemes have been presented and tested, but all of them seek to create classes of algae based on morphological traits and/or ecological behaviour, rather than evolutionary history.



The proposed scheme of Reynolds *et al.* featured 31 “functional” groups of freshwater algae, based on shared features of the species in the group.<sup>90</sup> The groups are defined by a combination of habitat, tolerances, sensitivities, and morphology. The habitats are defined by factors including the depth of water, the location of the species in that depth, the degree of mixing in the water, the nutrient conditions, and the time of year. The tolerances are defined with respect to high or low levels of light, carbon, specific or general nutrients, or turbidity. The sensitivities are to other species, flow conditions, light conditions, and to rising or falling levels of pH, Si, or CO<sub>2</sub>.

In 2010 and 2011, Kruk proposed a simpler scheme with seven groups that uses a combination of seven primarily morphological traits.<sup>91,92</sup> The groups are defined by the presence or absence of flagella, siliceous structures, mucilage (a viscous, gelatinous substance which sheathes the cell), or aerotopes (gas vesicles). Further classification was provided by threshold values of the volume, the surface to volume ratio, and the maximum linear dimension. Descriptions of the groups are given in Table 5.

Table 5. The morphology-based algae groups proposed by Kruk *et al.*<sup>91</sup>.

Group	Description	Examples from our algae species
I	Small organisms with high S/V	
II	Small flagellated organisms with siliceous exoskeletal structures	
III	Large filaments with aerotopes	
IV	Organisms of medium size lacking in specialized traits	
V	Unicellular flagellates of medium to large size	
VI	Non-flagellated organisms with siliceous exoskeletons	
VII	Large mucilaginous colonies	

As of a review in 2009, 63 studies had used the classification of Reynolds (2002) for algae studies.<sup>93</sup> This review also pointed out errors that had been made in the placement of certain species into the incorrect Reynolds codon, and suggests some modifications to make the habitat descriptions less ambiguous.

A meeting of the 14<sup>th</sup> Workshop of the International Association of Phytoplankton Taxonomy and Ecology showed numerous examples of studies demonstrating the use of morphological groups (rather than phylogenetic classifications) to characterize the seasonal variations in algae communities in water, or to compare the communities in ecologically similar bodies of water.<sup>94</sup>

In general, the features which define these groups can provide inspiration for the development of identification technology, which could be tailored to identifying the relevant traits. The sorting methods presented in this chapter are morphology-sensitive; thus, the relevance of size in particular is further explored.

### **Using algae size distributions to understand ecosystems**

Various studies have sought to understand the relationship between algae size distribution and population dynamics, functional behaviour, or ecosystem properties.

The spectra of size distributions of organisms in an environment usually follow a power function  $N=M^{\alpha}$  where  $N$  is the abundance of a given size range and  $M$  the size of cells in that range. Huete-Ortega *et al.* found that the factor  $\alpha$  changed for different oceanographic conditions, and concluded that size distributions could provide an efficient description of the transient state of a varying ecosystem.<sup>95</sup> Correlations have also been suggested between the species richness (number of species) and the size distribution.<sup>96</sup> It has also been shown that the algae dynamics in a body of water could be described by the size distribution of the community<sup>81</sup>, and that photosynthetic behaviour changes as a function of algae cell size.<sup>97</sup>

Further motivation for size-based measurements comes from correlating models to measurements. Baird proposes a size-based approach to model the interaction of different plankton species with each other and with their environment.<sup>98</sup> The model encompasses organisms from the sub-micron to the millimetre scale, and combines water, light, and wind conditions with size-based models of biomass, nutrient uptake, and predator-prey relationships. The authors mention the lack of knowledge of the size-distribution of biomass in a given location as a key limitation in the application of this model.<sup>98</sup>

## 4.2 Passive particle sorting methods

To address this demand for technologies which are sensitive to algae morphology, this chapter looks at size- and shape-sensitive sorting techniques. First, an overview of literature on passive particle sorting is presented. “Passive” refers here to systems in which a particle experiences a force related to its size or shape (*i.e.*, excluding systems with separate measurement and actuation steps). The focus is on forces created by fluidics or hydrodynamics, by channel geometry, or by optics. We only include approaches suitable for particles in the 1-50  $\mu\text{m}$  range and which allow throughput rates on an order similar to that of the system presented in chapter 2, or which can be scaled up to be comparable.

Unless otherwise specified, the following definitions are used:

Symbol	Meaning
W	microchannel width
H	microchannel height
$D_h$	microchannel hydraulic diameter, $D_h=2HW/(W+H)$
r	spherical particle radius
a, b	ellipsoid particle radii (short, long)
m	particle mass
$\mu$	fluid viscosity
$\rho_p$	particle density
$\rho$	fluid density
U	fluid velocity ( $U_{\max}$ = maximum velocity)
I	laser light intensity
n	index of refraction
c	speed of light
$\lambda$	wavelength of light

### 4.2.1 Sorting particles with optical forces

A single light source provides two forces on an object in the beam, one in the direction of the beam propagation and one perpendicular to it. The first is due to scattering: the change in momentum of reflected photons imparts a force on the particle in the direction of the light propagation. The second force is due to the refraction of light passing through the particle. If the light intensity is not symmetric, then the change in momentum from refraction is not symmetric either, and leads to a

net force perpendicular to the optical axis. This force is towards the highest optical intensity in the case  $n_{\text{particle}} > n_{\text{medium}}$  and away from it if  $n_{\text{particle}} < n_{\text{medium}}$ .

For Mie particles – objects with size comparable to or larger than the optical wavelength – the scattered field has been solved for spheres, spheroids, and cylinders.

For spheres, the scattering force

$$F_{\text{scattering}} = \frac{n_1 r_p^2}{2c} \int_0^{2\pi} \int_0^{\pi/2} I(\delta, x) Q_s \sin(2\theta_1) d\theta_1 d\phi \quad (4.1)$$

and gradient force

$$F_{\text{gradient}} = \frac{n_1 r_p^2}{2c} \int_0^{2\pi} \int_0^{\pi/2} I(\delta, x) Q_g \sin(2\theta_1) \cos(\phi) d\theta_1 d\phi \quad (4.2)$$

depend on the refractive index of the medium  $n_1$ , the distance in the transverse direction (perpendicular to the axis of light propagation) from the centre of the sphere to the centre of the illumination  $\delta$ , the angle between the incident photon and the particle surface  $\theta_1$ , and the polar angle  $\phi$ .<sup>99</sup> The values of  $Q_s$  and  $Q_g$  are dimensionless factors defined as

$$F = Q \left( \frac{n_1 P}{c} \right) \quad (4.3)$$

where  $P$  is the incident power and  $n_1 P/c$  is the incident momentum per second in a medium with refractive index  $n_1$ .<sup>100</sup> Note that the value of  $Q_s$  increases with an increase in the ratio of the sphere's refractive index to the medium's refractive index.

The laser light intensity distribution for a Gaussian beam

$$I(\delta, x) = \frac{2P}{\pi\omega(z)^2} \exp \left[ -\frac{2\delta^2}{\omega(z)^2} \right] \quad (4.4)$$

depends on the radial position  $\delta$  from the axial centre of the beam, as well as the beam power  $P$  and width

$$\omega(z) = \omega_o \left[ 1 + \left( \frac{\lambda z}{\pi\omega_o^2} \right)^2 \right]^{\frac{1}{2}} \quad (4.5)$$

as a function of the distance  $z$  from the beam waist, along the beam propagation axis.

Some examples of particle manipulation with optical forces are shown below, in Section 4.2.3.

## 4.2.2 Sorting particles with inertial microfluidics

In contrast with optical forces, inertial microfluidics approaches to particle manipulation rely only on the forces inherent in the fluid dynamics of a system. One of the commonly-cited properties of microfluidics is the ability to work at such low Reynolds numbers that inertial effects are negligible. However, this is an oversimplification that is not necessarily always valid. In fact, it is possible to create flow conditions in a microchannel where inertial forces are non-negligible while still remaining in a laminar regime. These inertial forces can be taken advantage of for particle sorting.

### The Segre-Silberberg effect: inertial sorting in a straight channel

When a fluid entraining small, neutrally buoyant particles flows along a straight channel, two forces cause the particles to cross the fluidic streamlines. The particle experiences an asymmetric shear force from the Poiseuille flow profile which pushes the particles towards the channel walls. This force competes with the wall-induced lift forces, which push the particles away from the walls. In order for the shear forces to be large enough to have significant effect, the particle size must be relatively large:  $d_{\text{particle}}/D_h > 0.07$  is required as a rule of thumb.

This combination of forces defines a set of equilibrium positions for the particles in the channel cross-section (Figure 43). In a circular channel, there is an annulus of equilibrium positions at a fixed distance from the centre of the channel. The exact position of this equilibrium location varies with Reynolds number; it is between  $0.6R$  and  $0.8R$  for  $Re < 350$ .<sup>101</sup> For a square channel there can be four or eight equilibrium positions, depending on the flow conditions. A high aspect ratio (rectangular cross-section) channel has two equilibrium positions.

This particle focusing effect has been demonstrated in numerous works from the Di Carlo group. This group showed that, for example,  $9\ \mu\text{m}$  particles at  $Re=90$  in  $50\ \mu\text{m}$  square channels reached an equilibrium position after 1 cm of channel.<sup>102</sup>

### Biasing with Dean force: inertial sorting in a spiral channel

The Segre-Silberberg effect in a straight channel creates a symmetric set of equilibrium positions depending on the channel shape. In order to sort particles into

a unique position according to their size, a biasing force must be applied which collapses the multiple equilibrium solutions to a single point.

This can be accomplished with the use of a curved channel shape. In a curved channel, two counter-rotating secondary flows (“Dean flows”) form in the direction perpendicular to the main flow direction (Figure 43). The combination of flow forces from the Dean flow and the previously-described shear and wall lift forces create a biased (non-symmetric) equilibrium position in the channel cross-section for particles in the flow.

The Dean flow is characterized by the dimensionless Dean number<sup>103</sup>

$$De = Re \sqrt{\frac{D_h}{2R}} = \frac{\rho U_{ave} D_h}{\mu} \sqrt{\frac{D_h}{2R}} \quad (4.6)$$

Assuming Stokes drag from the Dean flow on the particles, the force created on the particles by the Dean flow

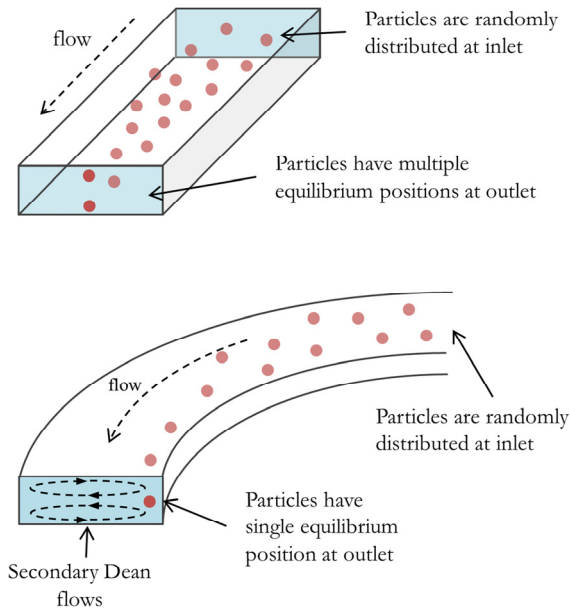


Figure 43. (Top) Particle sorting in a straight channel using the Segre-Silberberg effect: particles in a rectangular channel with  $Re \gg 1$  self-align to equilibrium positions due to inertial forces. (Bottom) A spiral channel (geometry not to scale) creates a counter-rotating secondary Dean flow, which provides an asymmetrical bias to the particle equilibrium positions.

$$F_{Dean} = \rho U_m^2 a \frac{D_H}{r} \quad (4.7)$$

works with or against the lift forces

$$F_{lift} = \frac{\rho U_m^2 a^4}{D_H^2} C_L \quad (4.8)$$

which depend on the lift coefficient  $C_L$ , which in turn depends on the particle's position in the channel cross-sectional.<sup>104</sup>

The ratio of the lift forces to the Dean forces on a particle

$$R_{LD} \sim \frac{2r}{D_H} \left( \frac{a}{D_H} \right)^3 \quad (4.9)$$

is dependent on the cube of the particle radius  $a$ . If the ratio  $R_{LD}$  is lower than one, the particles will be dragged around the channel following the Dean flows. If the ratio is larger than one, the particles will occupy an equilibrium position. The non-constant lift coefficient makes it impossible to analytically solve for a specific cut-off particle size, but the ratio does indicate the *existence* of a cut-off size above which particles will be focused.<sup>104</sup>

This approach has been demonstrated by the Di Carlo group with an asymmetrically wavy channel, used to manipulate particles from 2-17  $\mu\text{m}$  in diameter. They observed two limitations in the migration of particles: a loss of focusing occurred at  $a/D_H < 0.07$  and at  $De > 20$ . In both of these cases, the Dean drag becomes much larger than the lift forces, pulling the particles out of the equilibrium positions and dragging them around the channel with the secondary flows. The group has also applied this technique to sort particles by deformability<sup>105</sup> and aspect ratio.<sup>106</sup>

The Papanastasiou group has demonstrated the use of spiral microchannels to induce Dean flow to bias the inertial microfluidic forces and sort particles. This approach has been successfully used to sort 1.9  $\mu\text{m}$  particles from 7.3  $\mu\text{m}$  particles at  $De=0.47$  and to sort 10, 15, and 20  $\mu\text{m}$  polystyrene latex (PSL) microspheres at  $De=14.4$ .<sup>107,108</sup> The same device could also sort neuroblastoma cells ( $\sim 15 \mu\text{m}$  diameter) from glioma cells ( $\sim 8 \mu\text{m}$  diameter) with 80% efficiency, and with a high throughput rate of  $\sim 1$  million cells per minute. A spiral channel with cross-section 500  $\mu\text{m}$  x 110  $\mu\text{m}$  sorted red blood cells and white blood cells with at 95% efficiency in a 500x diluted blood sample.<sup>109</sup>

### 4.2.3 Combining or competing optical & fluidic forces

Many groups have used optical or fluidic forces for sorting particles; here, we highlight a few applications that have specifically used a combination of both. Each example shown has the laser beam oriented differently with respect to the direction of flow.

Kim *et al* used a single laser beam directed perpendicularly across a channel to sort  $5\ \mu\text{m}$  PSL particles transversely across streamlines by size (Figure 44).<sup>99</sup> A  $532\ \text{nm}$  laser beam had  $1.42\ \text{W}$  of power and a  $70\ \mu\text{m}$  waist directed across a channel that was  $300\ \mu\text{m}$  wide and  $100\ \mu\text{m}$  high. A mean flow velocity of  $80\ \mu\text{m}/\text{s}$  was used. No initial focusing mechanism was used to ensure that all particles started in the same section of the channel cross-section. Therefore, due to the Poiseuille flow profile in the channel, the amount of lateral displacement of the particles depended on their initial positions. Displacements of between  $20$  and  $60\ \mu\text{m}$  were observed; the particles were in the laser beam for approximately  $1\ \text{s}$ .

Helmbrecht *et al.* demonstrated a photophoretic device designed to serve as an optical chromatography system.<sup>100,110</sup> A two-beam optical trap was aligned along the same axis as the fluid flow. The measured velocity of the particle (and thus the effectiveness of trap) was used to back-calculate the particle's optical properties.

A last example, from the Squier group, used a  $2\ \text{W}$  laser diode bar focused with a cylindrical microlens.<sup>111</sup> The laser axis was perpendicular to the channel flow, with the long axis of the laser bar at an angle to the flow (similar to the geometry shown in Figure 45). By tuning the flow rate and laser power, they were able to identify the combinations where the drag force on a particle was not able to overcome the optical force from the laser. With slower flows or lower laser power levels, the particles

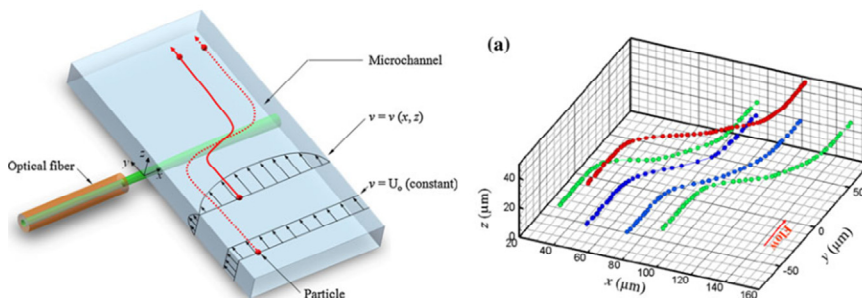


Figure 44. The cross-type single-beam particle sorter used by Kim *et al*; image is from Figures 1 and 6 in their paper.<sup>99</sup>



would instead travel along the line of the laser light until exiting the light field at the farthest downstream position. 2-10  $\mu\text{m}$  particle were used, although later work from the same group showed the setup was also able to manipulate particles around 100  $\mu\text{m}$  in diameter.<sup>112</sup>

## 4.3 Optofluidic sorting experiments

### 4.3.1 Principle

We choose a layout similar to that used by the Squier group to explore the optical force effects on particles in a microchannel.<sup>111,112</sup> A high aspect-ratio bar laser diode is focused inside a microchannel through which particle-laden water is flown. As illustrated in Figure 45, the channel axis is aligned in the  $x$  direction. The laser beam propagates in the  $z$  direction, with its bar orientation  $\theta$  defined with respect to the  $y$  axis. In these experiments,  $\theta \sim 55^\circ$ . As the particles traverse the laser beam, the optical forces pull them towards the point of highest intensity (along the line defined by the bar laser) while the fluidic forces pull them downstream. This combination results in a net displacement in the  $+y$  direction. The scattering optical forces also exert a force in the  $+z$  direction.

### 4.3.2 Modelling the combined optofluidic forces

A model of the combined optofluidic forces was created to estimate the required conditions for causing adequate particle displacement in the  $y$  direction. The solution for the Stokes flow in a rectangular channel from White<sup>113</sup> is used:

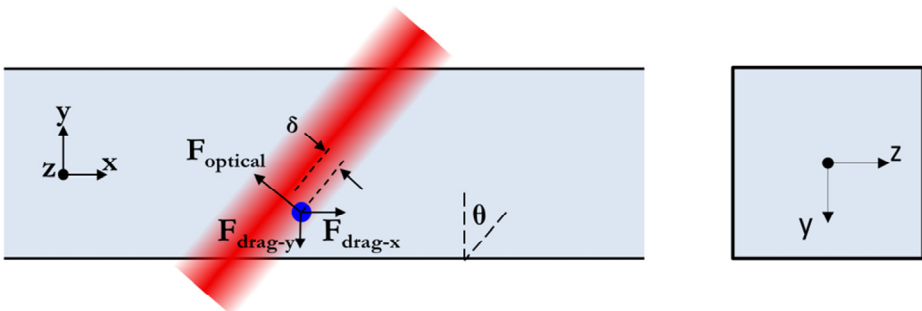


Figure 45. Chip layout for initial experiments. The fluid is traveling in the  $x$  direction, and the laser propagates along the  $z$  axis.

for  $-a < y < a$ ,  $-b < z < b$

$$u_{fluid} = \frac{16a^2}{\mu\pi^3} \left( -\frac{\Delta P}{\Delta x} \right) \sum_{n=1,3,5,\dots} \left[ (-1)^{\frac{n-1}{2}} \left( 1 - \frac{\cosh\left(\frac{i\pi z}{2a}\right)}{\cosh\left(\frac{i\pi b}{2a}\right)} \right) * \frac{\cos\left(\frac{i\pi y}{2a}\right)}{i^3} \right] \quad (4.10)$$

$$\frac{\Delta P}{\Delta x} = Q \frac{3\mu}{4ba^3} \left[ 1 - \frac{192a}{\pi^5 b} \sum_{n=1,3,5,\dots} \left( \frac{\tanh\left(\frac{n\pi b}{2a}\right)}{n^5} \right) \right]^{-1} \quad (4.11)$$

The drag force on a spherical particle

$$F_{drag} = 6\pi\mu Ur \quad (4.12)$$

depends on the particle radius  $r$ , the fluid viscosity  $\mu$ , and on the velocity difference  $U$  between the particle and the fluid.<sup>114</sup> In these simulations, we assume that the particles have matched the downstream (x-direction) velocity of the local fluid streamlines before the particle encounters the optical field.

The optical gradient force exerted by the laser bar diode acts on the particle in the x and y directions, and the scattering force acts in the z direction. For the following calculations, the z direction forces and motion will be ignored as the interest is in y displacement.

The balance of forces on the particle yields the system of differential equations which govern the motion of the particle

$$m \frac{du}{dt} = \cos(\theta) F_{gradient} + F_{drag}(u) \quad (4.13)$$

$$m \frac{dv}{dt} = \sin(\theta) F_{gradient} + F_{drag}(v) \quad (4.14)$$

which depends on the drag and gradient forces,  $F_{drag}$  and  $F_{gradient}$ .

Substituting in the expressions for the optical gradient force and the drag force yields

$$\frac{d^2x}{dt^2} = \frac{3Q_g n P_o \cos(\theta)}{8c\pi\omega^2 r \rho} \left( e^{-\frac{2(\delta+r)^2}{\omega^2}} - e^{-\frac{2(\delta-r)^2}{\omega^2}} \right) + \frac{9\pi}{2r^2 \rho} \frac{dx}{dt} - \frac{9\pi}{2r^2 \rho} U_{fluid} \quad (4.15)$$

$$\frac{d^2y}{dt^2} = \frac{3Q_g n P_o \sin(\theta)}{8c\pi\omega^2 r \rho} \left( e^{-\frac{2(\delta+r)^2}{\omega^2}} - e^{-\frac{2(\delta-r)^2}{\omega^2}} \right) + \frac{9\pi}{2r^2 \rho} \frac{dy}{dt}$$

where

$$\begin{aligned}\delta &= x \cos\theta \\ \delta &= y \sin\theta\end{aligned}\tag{4.16}$$

is the distance of the centre of the particle from the centre of the beam, and defines the vector along which the gradient force acts.

These equations are not solvable analytically, and so the solutions are found numerically with the Euler method. At each time step, the drag forces and optical forces are calculated and used to find the particle's new velocity and position. Specifically, the equation

$$y'(t) = f(t, y(t))\tag{4.17}$$

is solved by defining a time step  $\Delta t$  such that

$$t_n = t_0 + n \Delta t\tag{4.18}$$

and numerically solving

$$y_{n+1} = y_n + \Delta t f(t_n, y_n)\tag{4.19}$$

so that, in the  $x$  direction,

$$\frac{dx}{dt_{n+1}} = \frac{dx}{dt_n} + \Delta t \frac{\Sigma F_n}{m}\tag{4.20}$$

$$x_{n+1} = x_n + \Delta t v_n\tag{4.21}$$

with the velocity and position in  $y$  found similarly.

The values of  $Q_g$  were estimated from those calculated for a sphere by Ashkin.<sup>115</sup>

### Validation of forces and time step choice

To choose the appropriate time step  $\Delta t$  and to validate the fluidic force expressions, the optical forces are set to zero and the particle is set initially at rest. The drag force on the particle (Equation 4.12) should cause it to accelerate from rest to match the fluid velocity, with the particle's  $x$  velocity following an exponential curve with a time constant

$$\tau = \frac{2r^2\rho}{9\mu}\tag{4.22}$$

The time steps  $\Delta t$  should be small enough that the solution to the differential equation does not oscillate about the analytical solution in time.

As an example, the effect of the choice of  $\Delta t$  is shown for a  $15\ \mu\text{m}$  radius particle accelerated from rest (Figure 46). The simulation converges well for  $\Delta t \leq 1\ \mu\text{s}$ , for a flow speed of  $400\ \mu\text{m/s}$ . For higher flow rates, the time step should be decreased accordingly.

To compare the numerical solution behaviour with the analytical time constant  $\tau$ , a  $10\ \mu\text{m}$  radius particle is accelerated from rest in a fluid moving at constant velocity. The time constant  $\tau$  is  $23.3\ \mu\text{s}$  when calculated analytically using equation 4.22; the numerical solution yields the same behaviour of the particle (Figure 47).

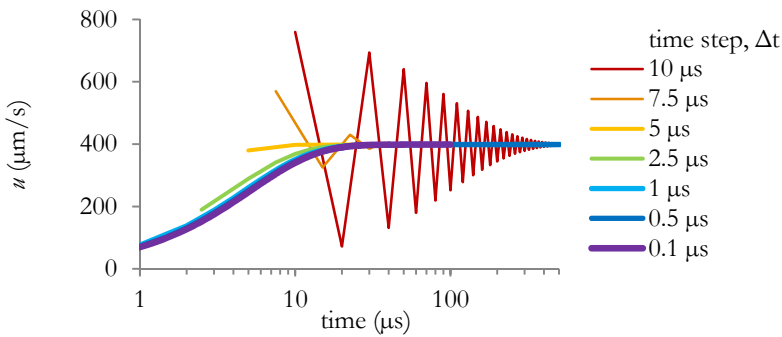


Figure 46. The results of the numeric simulation of the motion of an initially-quiet particle in a moving fluid (velocity  $400\ \mu\text{m/s}$ ), to optimize the choice of the time step  $\Delta t$ . The vertical axis  $u$  is the flow speed of a particle after release..

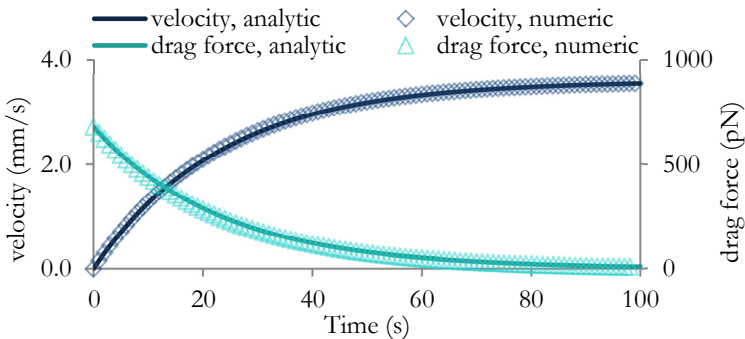


Figure 47. Comparison of the velocity and drag force on a spherical particle starting at rest in a moving fluid, as calculated analytically and numerically.

### 4.3.3 Simulation results

Figure 48 shows the net optical gradient force (amount of force, not directionality) exerted on a  $5\ \mu\text{m}$  radius sphere crossing the bar diode. The particle is assumed to be on the x-y plane (*i.e.* at  $z=0$ , which is at the centre of the channel, height-wise). The forces are small ( $<1\ \text{nN}$ ); however, on the microscale this is not too small to cause an effect. For example, a constant  $0.4\ \text{nN}$  force over a long enough time would cause a  $5\ \mu\text{m}$  radius sphere to accelerate to a terminal velocity of  $4.8\ \text{mm/s}$  in water.

The optical forces illustrated in section 4.2.1 are combined with the fluidic forces shown in section 4.2.2, using the Eulerian method described in section 4.3.1. The optical forces attract the particle to the position of highest optical intensity, creating a potential well along which the particle can travel. The drag forces of the fluid will act to push this particle out of the well, with the final particle position depending on the ratio of the optical and fluidic forces.

An example of the simulated trajectories of particles in the middle plane of the channel height (at  $z=0$ ) are shown in Figure 49. The particles are released at different positions in the channel width:  $0\ \mu\text{m}$  (in the centre of the channel), or at  $\pm 20\ \mu\text{m}$  in the  $y$  direction. A  $1\ \text{W}$  laser beam with a  $10\ \mu\text{m}$  beam radius in the short direction and a 100:1 aspect ratio shines across the channel at an angle of  $\alpha=45^\circ$ . The indices of refraction used are those of polystyrene latex ( $n=1.6$ ) in water ( $n=1.33$ ).

These simulations highlight a few issues with this approach which remain relevant even if the exact properties of the beam or particles change. First, the amount of

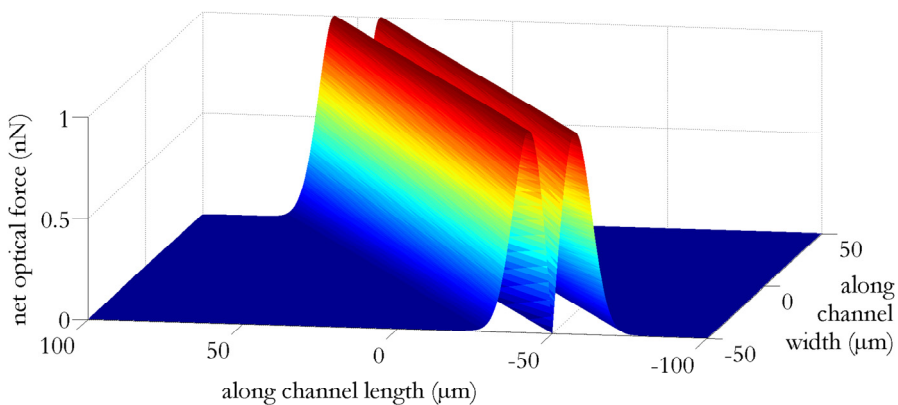


Figure 48. Net optical gradient force experienced by a  $5\ \mu\text{m}$  radius particle flowing along a channel with a laser diode bar oriented at  $\theta=45^\circ$  and a beam waist of  $5\ \mu\text{m}$  at the middle of the channel height.

offset in the transverse direction is quite small, especially for small particles. The beam width needs to be well-matched to the particle size to make any significant effect. Second, the amount of transverse displacement that the particles experience depends not only on the particle size, but also on the particle's initial position in the channel. Particles which are directed by the optical force towards a slower streamline have a larger total displacement than those directed towards a faster streamline with more drag.

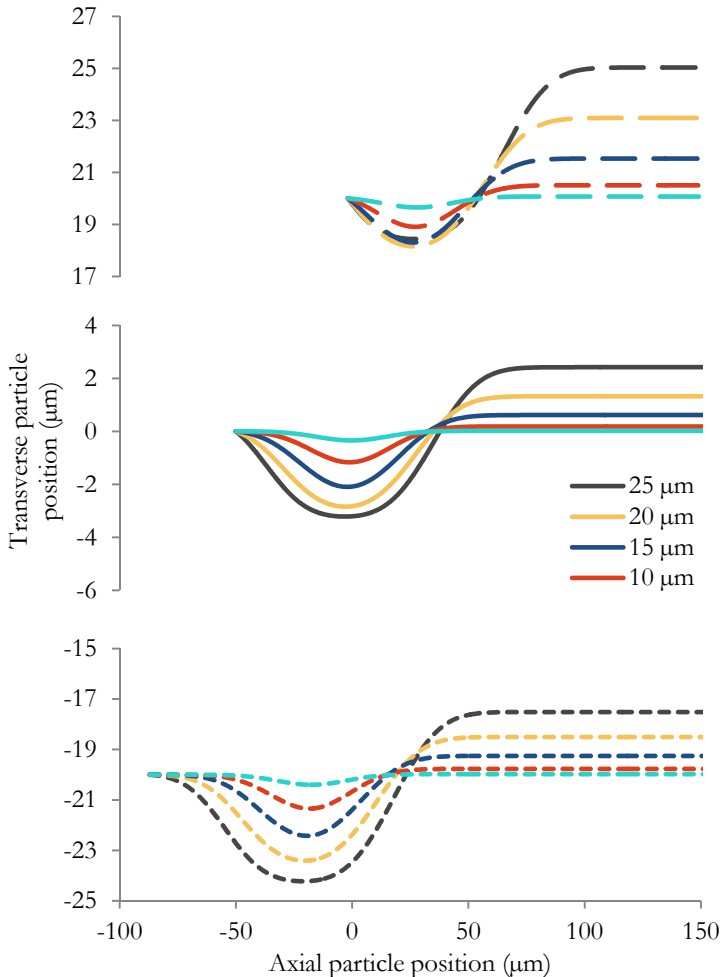


Figure 49. Top view of simulated particle trajectories as they pass through the laser bar oriented at  $45^\circ$  to the channel axis (*ie*,  $\theta=45^\circ$  in Fig. 9). The values in the legend represent the particle radii. The initial position is indicated by the y-axis intersection in each graph: (from top to bottom)  $+20$ ,  $0$ , and  $-20$   $\mu\text{m}$  from the centre of the channel.

### 4.3.4 Experimental setup

A proof-of-concept setup, inspired by the work of the Squier group<sup>111,112</sup>, was built using off-the-shelf components to experimentally study this technique. An 805 nm laser diode with a maximum output of 1 W was used (Thorlabs L808P1WJ). The light produced by the diode had a high (100:1) aspect ratio in the plane perpendicular to propagation. A cage mount system with a dichroic mirror and lenses aimed the focal point of the beam at a glass microchannel (Figure 50). The channel was illuminated from below with a white light source to enable imaging of the particles and their positions. A camera mounted on a microscope recorded the channel and particles at the position of the laser beam.

Measurements of the laser beam showed that the threshold current was  $1.0 \pm 0.03$  A (manufacturer specifications: 1.0 A average, 1.2 A max). The total power output of

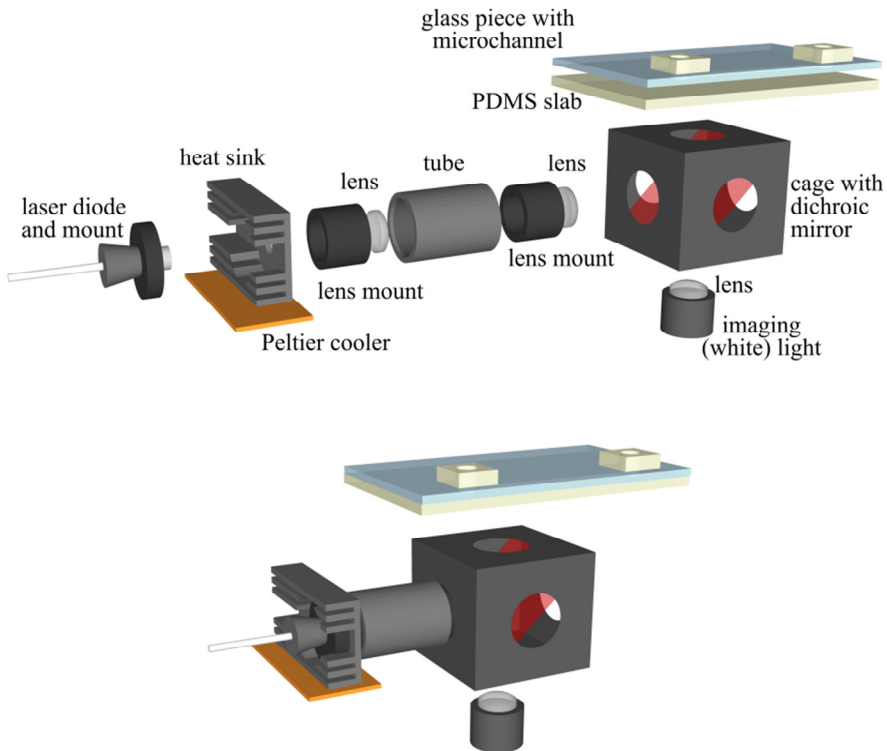


Figure 50. Parts and layout of experimental setup, in exploded (top) and assembled (bottom) view.

the beam was 1.16 W with only one lens; the dichroic mirror caused losses of 16.3% of the power.

The 1W laser produces a significant amount of heat. A Peltier device was used to measure the temperature of the diode during operation to ensure that it did not overheat. The laser was mounted onto a heat sink and a small computer fan was used to cool the laser during operation. This provided enough heat removal that the cooling function of the Peltier device was not necessary.

### 4.3.5 Microchannels

Microchannels were fabricated with a femtosecond laser as described in Chapter 2. The glass chip had a straight channel fabricated on one surface, with through-holes traversing to the other surface of the glass at the ends of the channel, to allow fluidic access (Figure 51). The channel was 100  $\mu\text{m}$  wide, 60  $\mu\text{m}$  high, and 4 cm long. As with the original algae chip, the fourth channel wall is formed by placing a piece of PDMS placed on the glass.

### 4.3.6 Experimental results of optofluidic separation

Experiments were performed with 5  $\mu\text{m}$  diameter PSL microspheres. A very low flow rate was required to observe the effects of the optical gradient force. The syringe pump used was not able to go as low as desired with the syringes available. Therefore,

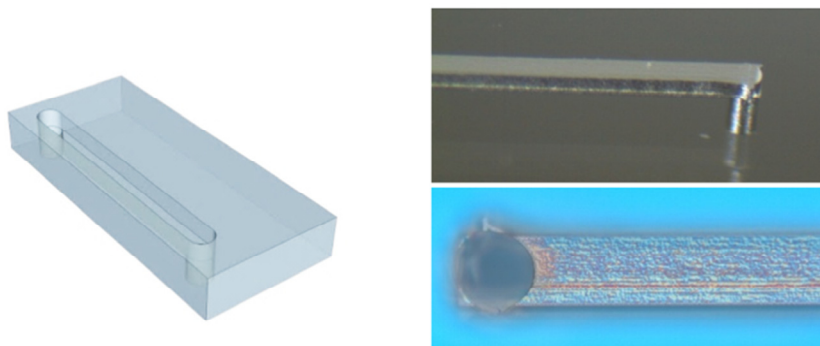


Figure 51. (Left) Channel design, not to scale. (Right) Microscope images of the fabricated channel from a stereo microscope. The bottom picture is focused at the bottom surface of the channel to show the roughness, with the inlet visible on the left. A high speed x-y translation speed was used in the machining, resulting in the imperfections visible at the corners of the channels. The channel is 100  $\mu\text{m}$  wide, 60  $\mu\text{m}$  high, and 4 cm long.



during experiments the pump was run at the minimum speed and then turned off so that the flow rate would slowly decrease over time as the pressure built up in the system slowly reached atmospheric pressure.

The video recording was used to determine the initial velocity of the particles, the offset of the particles in the  $y$  direction caused by the laser beam, and to determine if the fluid flow rate was approximately constant while the particle was traversing the beam (see examples, Figure 52).

MATLAB scripts were written to automatically trace the trajectories of multiple particles from a video (Figure 53). The results show offsets of between  $0\ \mu\text{m}$  and  $13\ \mu\text{m}$  depending on the local flow velocity (Figure 54). Particles in faster-moving streamlines were displaced less because of the higher drag forces.

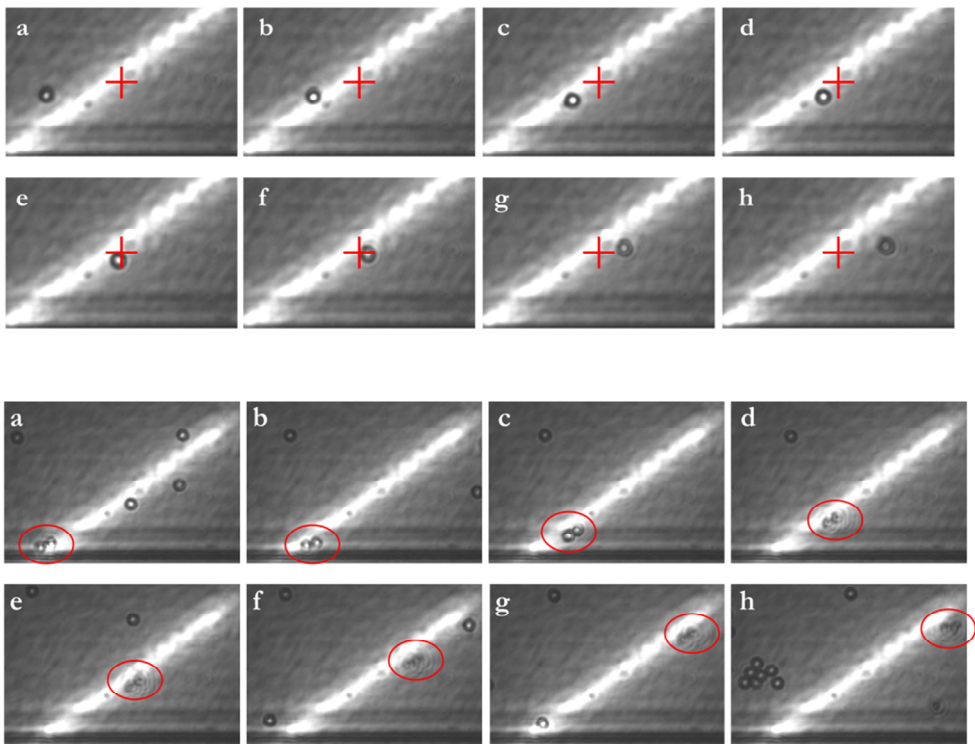


Figure 52. A single particle (top example) or a doublet (bottom example) enter the beam, are deflected upwards, and exits the beam at the point that the fluidic drag forces exceed the optical gradient force. As a visual aid, a red “+” symbol has been overlaid in each photo in the same position in the top example, and the doublet has been circled in each picture in the bottom.

The particles' z-position also changed due to optical scattering forces. This was visible but not quantifiable from the particle's motion in or out of focus while in the beam (see example in Figure 52).

It was observed that particle doublets (two connected particles) traversed further along the optical beam than single particles, and that they aligned so that the long axis of the doublet was parallel to the long axis of the laser cross-section (Figure 52). This is a logical outcome: in this configuration, the doublets would have twice as much optical force as a single particle, but less than twice the drag force, leading to more

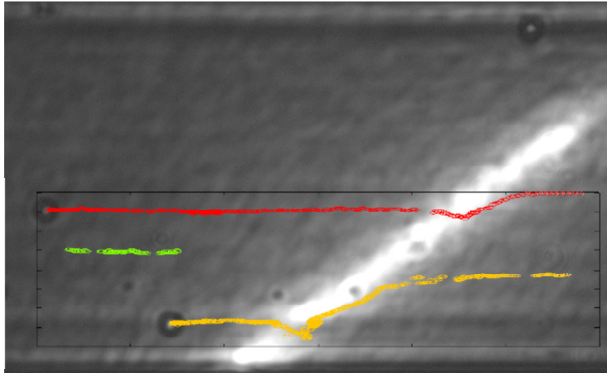


Figure 53. Traces of particle motion from the automated MATLAB script. The lines are overlaid on the image of the channel at the beginning of the recording. The particle closer to the wall has a lower velocity and is displaced further than the particle near the centre of the channel.

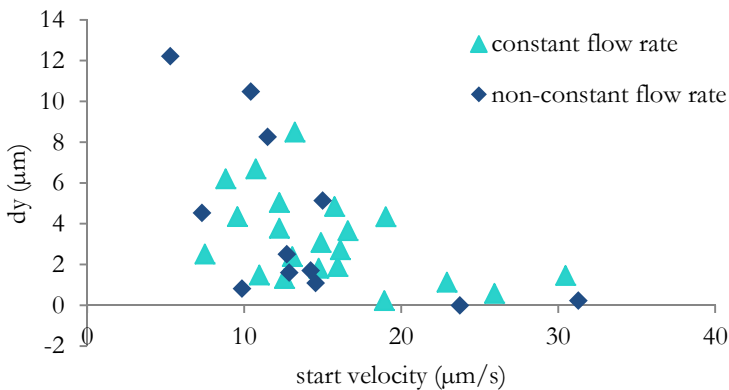


Figure 54. Offset in the channel width caused by the particle traversing the laser bar. Due to the low flow rates used the fluid velocity was not always constant; samples with a visibly fluctuating flow rate are indicated with dark points.

displacement than the single particles.

The 5  $\mu\text{m}$  particles were chosen because of the low flow rate: larger particles settled out of the flow before they reached the laser beam. This limitation could be overcome by increasing the density of the fluid (for example, by adding glycerol to the water) but this also causes an increase in the fluid's index of refraction, decreasing the strength of the optical gradient force.

The advantages and disadvantages of this technique are discussed at the end of this chapter, so that they can be compared with those of the fluidic sorting presented next.

## 4.4 Size-separation with fluidic forces

To compare optical sorting with fluidic sorting, a spiral microchannel was used to test the inertial Dean flow sorting of microspheres and algae.

### 4.4.1 Experimental

The microchannel used for separation had a cross-section of 350  $\mu\text{m}$  wide x 100  $\mu\text{m}$  high. It was in the shape of an Archimedean spiral with three loops, an initial radius of 5 mm, and a final radius of 10 mm. The Dean number ( $De$ ) is a function of the radius of curvature and thus varies over the channel length, but an average can be calculated for a given flow rate. The flow rates in our experiments are all between 0.4 mL/min and 4 mL/min, yielding average Dean numbers between  $De = 7.9$  and  $De=31.5$  respectively.

#### Microchannel fabrication

The microchannel was fabricated using soft lithography. First, a negative mask of the channel design was printed on a transparency sheet with an ordinary office laser printer. Photoresist (SU-8) was spin-coated onto a silicon wafer using the manufacturer's recommended parameters for a 100  $\mu\text{m}$  thick layer. The photoresist was exposed to ultraviolet light through the printed mask, so that the channel pattern was cross-linked and the remaining photoresist could be removed by developer.

Since the mask was made on a laser printer rather than by a professional mask supplier, there was some minor light leakage through the "black" parts of the mask. This necessitated some minor adjustments from a standard photolithography process. To prevent cross-linking in the dark areas, the exposure time was kept as short as possible. The substrate was left in the developer for a long time to remove as much

extraneous cross-linked SU-8 as possible. Despite these steps, there was still some poorly-adhered but cross-linked SU-8 visible on the wafer outside of the channel pattern. To remove this, the substrate was coated with PDMS which was cured, removed, and discarded. The extra SU-8 adhered well enough to the PDMS that it was pulled off the wafer with the silicone, and the wafer could be used for ordinary replication after that.

PDMS silicone was prepared at a 1:10 hardener:base ratio and poured on the wafer/photoresist mould. After the PDMS had cured in an oven at 90°C for 1.5 hours, it was removed from the mould, and holes were punched at the channel inlet and outlets. The PDMS channel and a glass microscope slide were both exposed to oxygen plasma and then put in contact with one another, permanently bonding them.

## Setup

The experimental setup (Figure 55) consisted of the spiral microchannel, a syringe pump which flowed the sample through the channel at a user-chosen flow rate, and a camera with a microscope objective positioned directly above the channel exit. The transparent channel was illuminated from below. The camera was set to capture 120 frames per second. 240 frames were captured at each flow rate (0.4 mL/min to 3.6 mL/min in increments of 0.2 mL/min) for each sample type.

## Samples

Experiments were run with three sizes of polystyrene latex (PSL) microspheres,

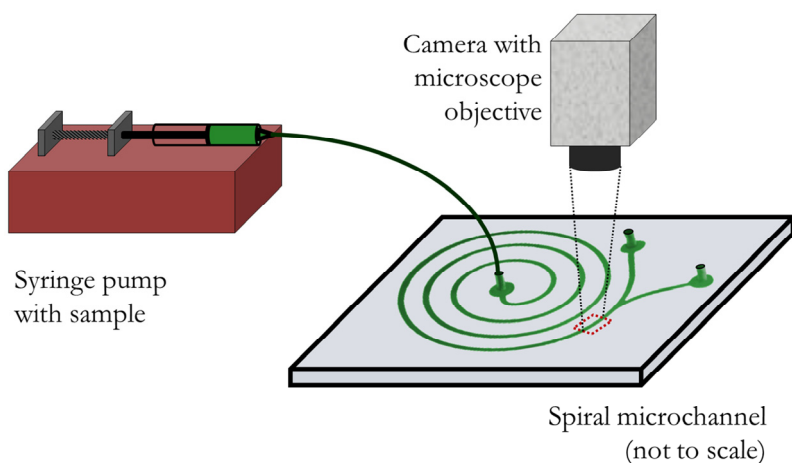


Figure 55. Experimental setup for particle sorting in a spiral channel.

nominally 5, 10, and 20  $\mu\text{m}$ . Micrographs showed the actual sizes of the microspheres to be  $6.2 \pm 0.5 \mu\text{m}$ ,  $11.1 \pm 0.2 \mu\text{m}$ , and  $20.2 \pm 1.3 \mu\text{m}$  (mean  $\pm$  standard deviation) respectively. Three species of algae were also tested, with the goal of separating highly non-spherical samples; pictures of the species are in Figure 57. The three species used were *Chlorella vulgaris* (spheres with  $6.0 \pm 1.0 \mu\text{m}$  diameter), *Cyanobeece aeruginosa*, (ellipsoids with a long axis of  $15.6 \pm 2.3 \mu\text{m}$  and short axis  $11.1 \pm 1.0 \mu\text{m}$ ) and *Monoraphidium griffithii* (high aspect ratio cylinders approximately  $137 \pm 35 \mu\text{m}$  long by  $7.9 \pm 1.5 \mu\text{m}$  diameter).

## 4.4.2 Data analysis

The analysis of the images is automated using MATLAB as follows:

1. **Create a background.** Form a background image by taking the mean value of each pixel over 100 images from the same dataset. This must be repeated separately for each dataset because whenever the sample was changed, the channel moved slightly with respect to the camera.
2. **Background subtraction.** Identify the mean value of the background image in a rectangle on the far right of the image (Figure 56a) and in the same location on the image with particles (Figure 56b). Subtract this difference from the particle image. Then, create a new background-subtracted image where the value of each pixel is

$$final\ image(i, j) = particle\ image(i, j)^2 - bgimage(i, j)^2 \quad (4.23)$$

(Figure 56c). Finally, use a low-pass filter to remove the background noise from the image (Figure 56d).

3. **Sum over many images.** Step 2 is repeated for all images in the set. The images are summed together, and then summed column-wise and normalized to create a plot of the particle distribution across the channel (see examples, Figure 57).
4. **Image registration subtraction.** The datasets are not all in exactly the same x-y position due to small shifts in the channel position with respect to the camera. To account for this in the data analysis, MATLAB's image registration tool is used to identify the translation that best aligns each background image to a reference background image. The values are used to shift the particle distributions in x to make them comparable.

### 4.4.3 Results

An example of the results (for flow rate 1.6 mL/min) is shown in Figure 57. At this flow rate, the smallest particles (the 5  $\mu\text{m}$  spheres and the *Chlorella* algae) do not focus but remain spread across the channel. The medium sized particles (10  $\mu\text{m}$  spheres and *Monoraphidium*), focus, but not as strongly as the largest particles (20  $\mu\text{m}$  spheres and *Cyanobcece*). The largest particles both focus to a position closer to the channel wall than the medium particles. Both the *Monoraphidium* and the *Cyanobcece* are more spread out and further from the wall than the 10 and 20  $\mu\text{m}$  spheres.

The average positions of the microspheres and algae in the channel as a function of flow rate are shown in Figure 58. The smallest microspheres (5  $\mu\text{m}$ ) and algae species (*Chlorella*) do not focus at any speed but remain scattered around the channel cross-section. These particles are very small compared to the width of the channel, and the shear forces across them are consequently very low. In this case, the ratio  $R_{LD}$  is much smaller than one, and the Dean flow drag forces are much larger than the lift forces.

The larger particles (10, 20  $\mu\text{m}$ ) and algae (*Monoraphidium* and *Cyanobcece*) can be focused, and can be distinguished from one another. Of particular interest for morphology-based sorting, the *Monoraphidium* & *Cyanobcece* have similar equivalent

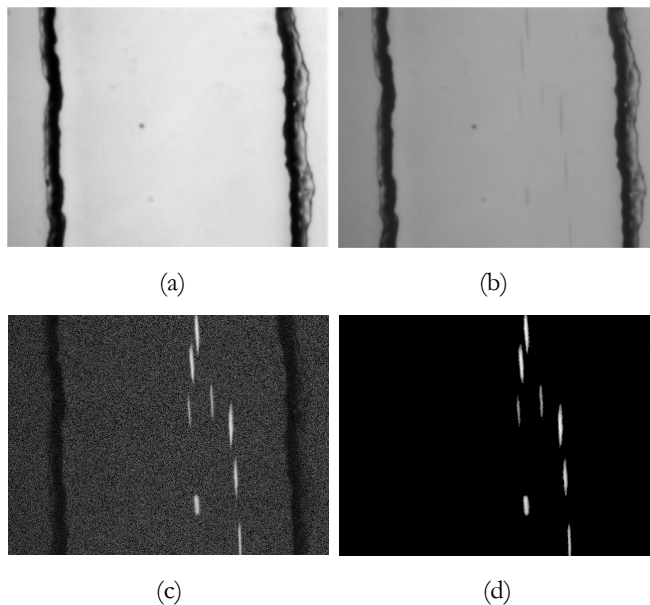


Figure 56. Image processing. (a) shows a background image, and (b) an image with particles. (c) shows the result of background subtraction, and (d) the result of the low-pass filter, which removes noise from the image.

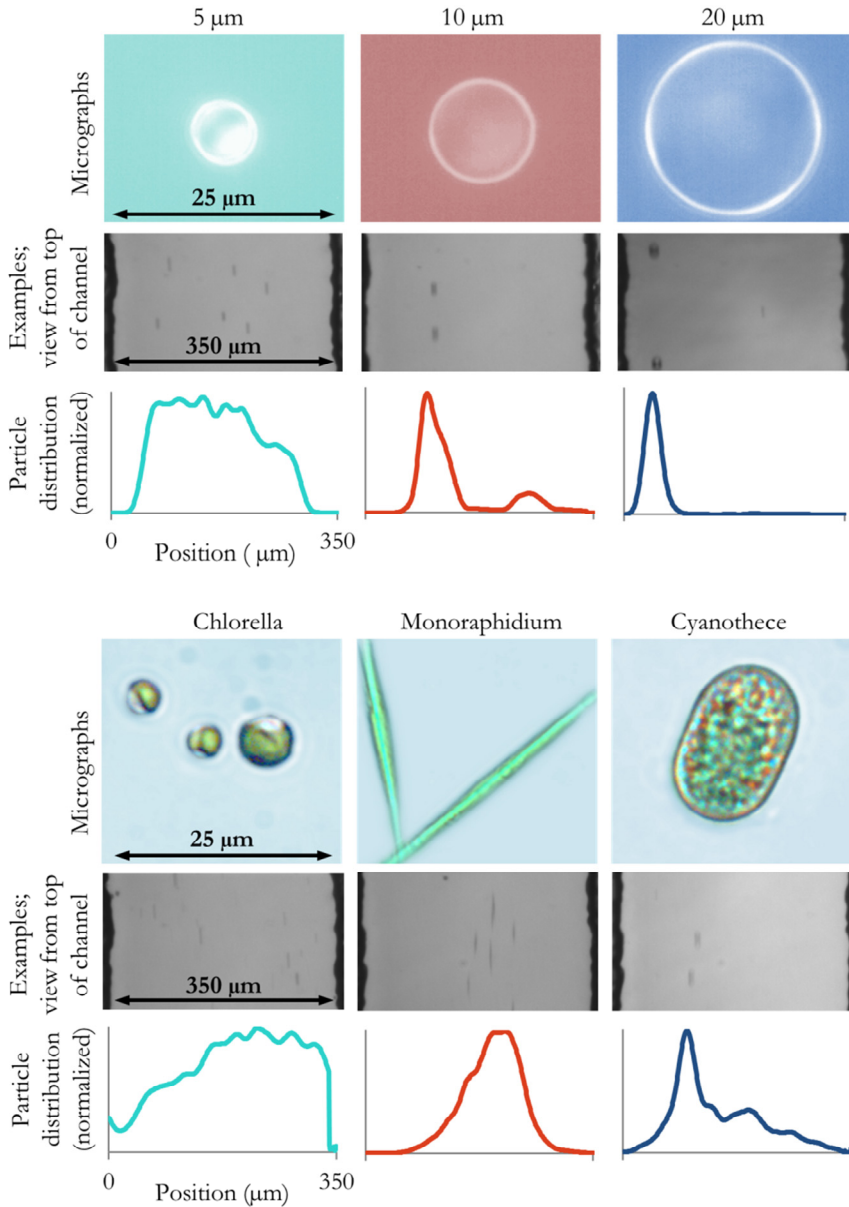


Figure 57. (Top rows) Micrographs of the three different sizes of microspheres and species of algae used in this study. (Middle rows) Examples of images captured at the end of the channel at 1.6 mL/min. (Bottom rows) Normalized distributions of the particles/algae across the channel cross-section at 1.6 mL/min, each combining the particles in 240 images.

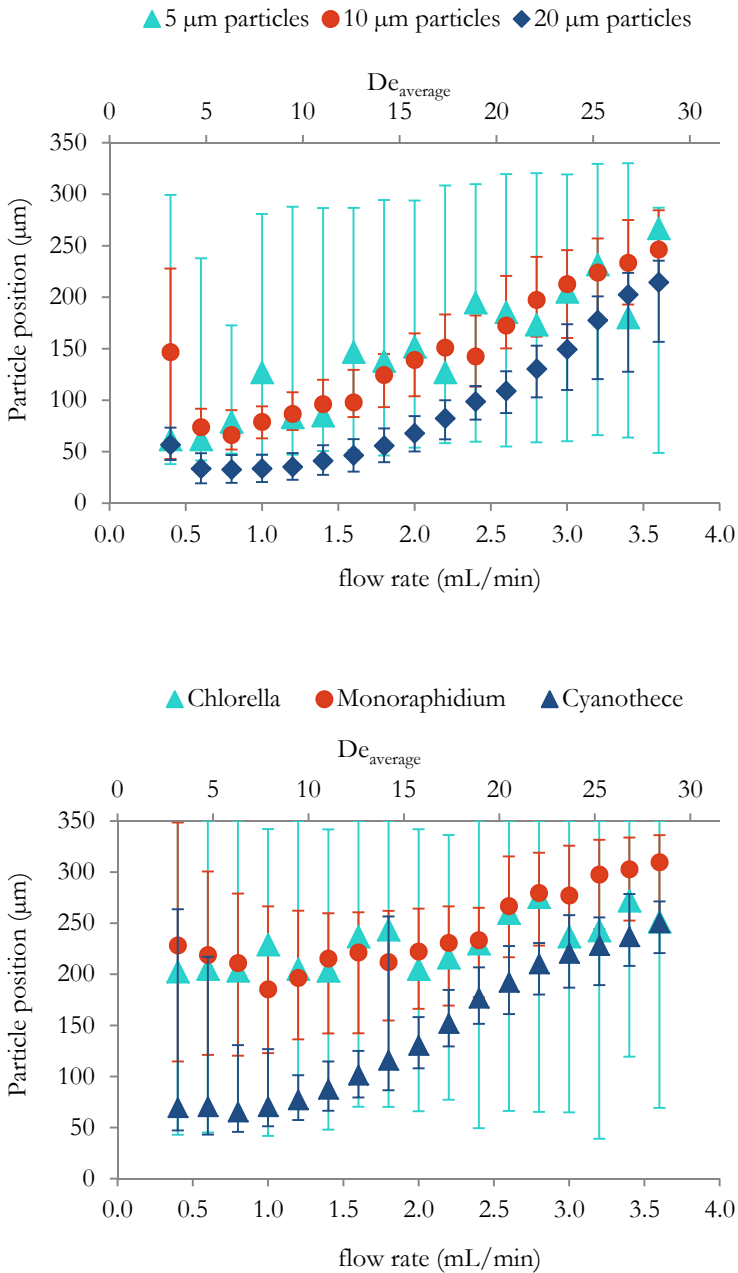


Figure 58. Position of the microspheres (top plot) and algae cells (bottom plot) as a function of the flow rate through the channel. The data points represent the peak position in the particle distribution, with the error bars representing its full-width half-maximum (FWHM) width.



spherical diameter to one another, but can still be separated because of their very different shapes. The *Cyanothece*, which are ellipsoids of 10-15  $\mu\text{m}$ , behave very similarly to the 10  $\mu\text{m}$  spheres. They are initially focused near the edge of the channel and the position of this focus moves towards and across the channel centre with increasing flow rate. The *Monoraphidium*, which have a high aspect ratio, tend to remain closer to the centre of the channel even at low flow speeds. The small cross-section of the *Monoraphidium* in the plane perpendicular to the flow direction suggests that the shear and lift forces from the fluid are very small compared to the Dean forces acting on the larger cross-section of the particles in the other directions.

### Separation efficiency

A separation efficiency  $\eta$  was defined for the separation of two species, and applied to the measurements of the particle positions in the channel. This value was defined by identifying the point  $x_{\text{sep}}$  in the channel width where a certain fraction  $\eta$  of one species would pass to the left of  $x_{\text{sep}}$  and the same fraction of the other species would pass to the right of  $x_{\text{sep}}$ . This separation efficiency was found for the separation of the 10 and 20  $\mu\text{m}$  spheres and of the *Monoraphidium* from the *Cyanothece* (Figure 59). The microspheres could be separated with an efficiency of  $>90\%$  for many of the flow rates tested, with the best results at 1.6 mL/min ( $\eta=96\%$ ). The *Monoraphidium* and *Cyanothece* separated the best at 3.2 mL/min, which yielded  $\eta=77\%$ .

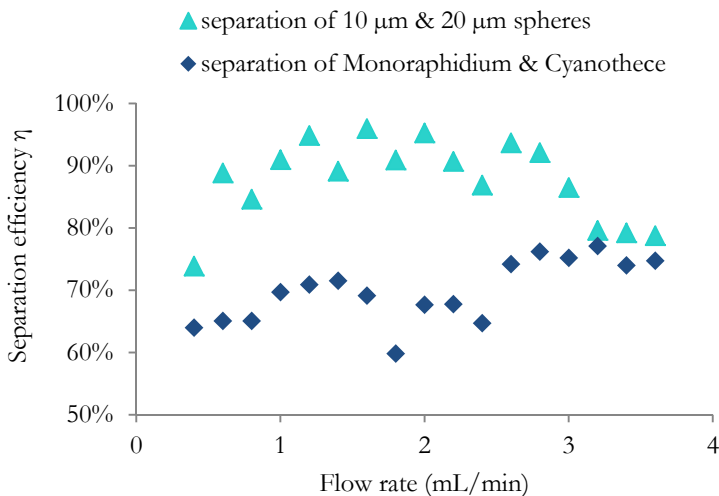


Figure 59. Separation efficiency of the 10 and 20  $\mu\text{m}$  microspheres and of two species of algae in the spiral microchannel.

The higher separation efficiency of the microspheres compared to the algae is likely due at least in part to the higher polydispersity of the algae. This can be seen in the coefficient of variation (the ratio of the standard deviation to the mean) of measurements taken from 20 cells or particles of each type, from optical microscope images. The *Monoraphidium* have a coefficient of variation of 0.25 in the length and 0.20 in the diameter. The *Cyanothece* have a coefficient of variation of 0.15 along the long axis and 0.09 in the short axis. In contrast, the coefficient of variation of the sizes of the 10 and 20  $\mu\text{m}$  spheres is 0.02 and 0.06, respectively.

## 4.5 Discussion and conclusions

In this chapter, we demonstrated that both optical and inertial microfluidic sorting techniques can offset particles positions in the cross-section of a flow. The optical gradient forces method can create a cross-streamline displacement of small particles. However, this approach has several drawbacks. First, the amount of displacement depends strongly on the initial velocity, which means that the particles should be focused in both dimensions of the channel cross-section for this technique to be useful as a reliable sorting mechanism. This is not an unexpected result, but since two-dimensional flow focusing is complicated, it was not used in this preliminary exploration. Second, the optical forces are rather weak (typically in the nN range) and strongly depend on the optical field gradient. A very optimally-focused laser beam is required to achieve this high gradient, along with low flow speeds. While feasible in a lab setting, this requirement makes this approach less attractive in a device intended for field work.

The performance of the optical system could be improved. A more focused beam would provide stronger gradients, particularly valuable for the 5  $\mu\text{m}$  particles which had a diameter smaller than the beam waist. The particle size was not optimal: the optical gradient force scales with the particle radius squared, while the drag force scales with the radius. The sorting would thus work better for larger particles, but larger particles will also be affected by the gravitational forces which scale as the radius cubed. Many of the algae specimen are both larger and of lower density than the microspheres tested here, but they also have a lower index of refraction, decreasing the optical gradient forces. The polystyrene has an index of refraction approximately 1.2 times that of water's, while the index of refraction of microalgae have been reported at 1.01 to 1.07 times that of water.<sup>116,117</sup>

Applegate *et al.* calculated the optical force that a 5 W laser in the same configuration would exert 100 pN on a 20  $\mu\text{m}$  diameter sphere of the same material as tested

here.<sup>112</sup> 100 pN is the same drag force as exerted on a 20  $\mu\text{m}$  particle in water moving at a velocity of 0.6 mm/s. For comparison, the slowest mean water velocity in the flow rate characterization experiments of Chapter 2 were at 1.7 mm/s. The best separation results found with the spiral microchannel had a mean water velocity of 760 mm/s.

Besides this much higher throughput rate, the fluidic approach has significantly lower instrumentation requirements: the only thing required is a pump and the appropriate choice of channel geometry. Its main drawback is the relative lack of flexibility. The optical system can be tuned, altered, and controlled to suit the desired sorting parameters; this feature may be desirable in a more complex device, particularly in a lab setting. The inertial system is restricted to changing the cut-off size of the focused particles by tuning the flow rate to match the desired size.

A further factor in favour of the fluidic sorting for this application is that of cost. The optical approach requires several components: a laser diode, diode power supply, a fan or other cooling system, and focusing lenses. Not only do these components require careful engineering to ensure that they retain their correct positions for focusing, but the number of components and their careful assembly make this approach more costly.

For potential use of this technology in a field-deployable sorting device, the separation of the particles would have to be exploited by either an in-situ measurement of the particle position or by separating the channel into multiple outlets.



# 5

Conclusions & outlook

The identification of algae species is a vital and challenging problem. The simple, robust optofluidic device and analytical methods presented in the 2<sup>nd</sup> and 3<sup>rd</sup> chapters yields data suitable for the classification of microspheres and algae. Besides classification, size-sensitive information can be extracted, which can be useful to phycologists studying species dynamics. Furthermore, the detection approach – that of a single laser source illuminating a single detector – is simple and requires a minimum number of components, and yet provides enough data to yield successful and useful results for the measurement and classification of algal cells.

The device presented has many inherent advantages compared to traditional microfluidic devices. Its monolithic nature renders it robust against mechanical failure, provides inherent alignment of the waveguide and the microchannel, and the material (glass) is chemically and thermally stable. The integrated, sub-surface curved waveguide provides a high signal-to-noise ratio. Creating a device with these properties is made possible by the use of a femtosecond laser for fabrication, through which the three-dimensional optical and mechanical structures of the device can be formed from a single piece of material.

Characterization experiments showed that the microfluidic nature of the device provides advantages that improve the system performance. Specifically, high aspect ratio particles are aligned to the axis of the flow by fluidic forces before they reach the sensor region, increasing repeatability in the measurements. Further characterization studies on the device's sensitivity to the flow rate and trigger levels set by the user were useful in the laboratory experiments, and can inform later decisions about the hardware used for a field-deployable device.

Simple optical models were created to study the interaction of the light transmitted by the waveguide with the passing algae and microspheres. The models show that the changes in the total light intensity correspond reasonably well to the data obtained from algae cells, particularly when using particle volume as a metric. However, while the more complex differential signals are similar to the measured signals, they lack higher-order features seen in the experiments. From this we can conclude that the ray-based model of the light refraction and absorption provides relevant information, but cannot fully describe the behaviour of the system during measurements. A complete model, including the micro- and nano-scale features within the algae and the wave nature of the light, may provide further insight into the formation of the optical intensity distributions.

A study of two pattern recognition approaches showed that neural networks consistently outperformed discriminant analysis for predicting the algae species from

the photodiode signals. The initial neural network results were already promising: for a mixture of river-collected detritus and lab-cultured *Cyanobeece*, the system had a success rate of over 90%. The samples from a mixture of three sizes of microspheres were correctly identified by size 85% of the time, and the cells in a mixture of five algae species were correctly identified at a rate of 78%.

The neural network results were improved by an optimization process; the most significant improvement resulting from this study was using a training algorithm that automatically optimizes the regularization parameter, preventing overtraining. This process resulted in an increase in the rate of algae identification; the cells from the five mixed species were, in the end, identified correctly for 91% of the samples. The worst results were found for the species *Chlorella*, which have a diameter only four times larger than the wavelength of the light. This suggests some room for improvement in future developments. First, a shorter wavelength of light could be used, and second, a smaller channel and narrower beam could be adapted. In the latter case, a pre-sorting step would be required to separate out the larger algae from the flow.

To explore options for size-sorting, two techniques were explored. Both optical forces and inertial microfluidic forces provide passive, size-sensitive sorting of small particles in a flow. The gradient forces from a high aspect ratio laser bar diode caused polystyrene microspheres to cross the streamlines of the flow. Simulations and results from the literature show that this effect is size-sensitive, and experimental results were obtained which demonstrated the effect of flow rate on the ability of 5  $\mu\text{m}$  particle to traverse the flow. However, this technique required extremely low flow rates and was highly sensitive to the positioning of the components, for the optical configuration used in our experiments. Better optical focusing would improve the results, although the flow rates shown in other setups in the literature are still very low even with better setups.

A second method, using high flow rates in a spiral-shaped channel, relied on inertial forces and secondary flows to sort the particles by shape and size. Both microspheres and algae could be sorted with this method; 10 and 20  $\mu\text{m}$  spheres could be separated with a separation efficiency of 96%. Two algae species with very similar volumes but very different shapes could be sorted into distinct streamlines with a separation efficiency of 77%.

A major point of comparison between these techniques is the throughput rate: the optical setup worked with flow velocities on the order of 10's of microns per second, while the fluidic separation worked at 100's of millimetres per second. The optical

setup could perform more complex and flexible sorting tasks which may be highly relevant in other applications. For the relatively low-complexity sorting done here, the inertial fluidic sorting system is more appropriate for a field-deployable device. This technique complements the device in the previous chapters, not only by providing a size-sensitive method for pre-sorting algae towards different detectors, but it may also serve as the foundation for a high-throughput morphology-sensitive algae monitor.

### **Device performance and potential field deployability**

The ultimate goal of this project was to combine optics and fluidics to identify the species of algae, using technology not only suitable for a lab but which could be adopted for use in the field. This means that the materials should be able to withstand a range of temperatures and harsh environmental conditions, the device should be adequately small and low-powered to work on a remote platform, and the analytical method should not require a high-performance computer on board. Further, the number of species and throughput rate of the device should be informed by the requirements of end-users and by data on typical algae species dynamics.

The material used, glass, is chemically and thermally robust, and can withstand harsher conditions than many materials commonly used in microfabrication. Portable systems with pre-defined neural networks implemented on microcontrollers have been demonstrated for other applications, so this approach should be technically feasible on a portable system.

However, various other aspects of the current device design would need to be modified to improve performance, specifically in the realm of fluid manipulation and sample handling. First, for a continuous flow-through device, a robust pump would be needed to create a constant flow rate, in a range suitable for microfluidics. To decrease the chances of the pump interfering with the sample, a pump could be attached at the exit of the device to create a negative pressure at the outlet of the microchannel, which is the opposite of the setup used in this work so far.

The two other main concerns are those of throughput rates and microchannel clogging. To sample as much water as possible, the device throughput rate would need to be increased as much as possible without loss of information. As it is used currently, the device's flow rate is limited by the need to take clear photos of the algae in the microchannel for separate, manual identification to confirm the device performance. Without this limitation, the flow rate could be significantly increased, as long as the collection rate of the photodiode data increased correspondingly. Even with the photodiode and data acquisition system presently used, the data collection



rate could be increased at least 20 fold if the in-situ images were not collected. The other aspect to throughput rate – that of data analysis – would depend on the eventual system.

For example, a requirement that at least 1000 cells should be sampled as a minimum, a sample with 100 cells/mL could be measured in 30 minutes at a flow rate of 333  $\mu\text{L}/\text{min}$ , and a sample at 10 cells/mL in 12 hours at 139  $\mu\text{L}/\text{min}$ . Note that these flow rates are significantly higher than those used in the identification system in Chapter 2 of this work, but also much lower than those used in the fluidic pre-sorting system in Chapter 4.

The potential for channel clogging would be significant in an uncontrolled, outdoor environment. An ideal system would be able to handle phytoplankton ranging in size from 1  $\mu\text{m}$  up to several hundred micrometers<sup>118</sup>, which could be accomplished by creating multiple parallel sensing channels of different sizes, with a rough size-based pre-sorting step upstream of the sensors.

A hybrid approach with a multi-tier pre-filtering step based on the inertial microfluidics of Chapter 4 could be a solution. As an example, the first sorting step could work as a filter to remove overly large particles. A second sorting step could split the particles into two size bins, which each group directed towards a detector more suitable for that size range. A last step could sort each group of particles by size and measure their location in the cross-section, as well as potentially serving as an up-concentrator for the particles.

In conclusion, the technology presented in this thesis provides a set of tools which, combined, are more powerful than the sum of their components. A single monolithic device – one with the ability to pre-sort algae cells by size and shape and classify the species with a powerful and adaptable analytical method – will offer new possibilities for algae monitoring to commercial sectors, regulatory bodies, and scientists seeking to understand the complex dynamics of these life forms without which life as we know it would not exist.

# References

1. P. McCormick and J. Cairns, "Algae as indicators of environmental change," *J. Appl. Phycol.* **6**(5-6), 509–526 (1994).
2. R. Brayner et al., "Micro-algal biosensors," *Anal. Bioanal. Chem.* **401**(2), 581–597 (2011).
3. I. Chorus and J. Bartram, *Toxic Cyanobacteria in Water: a Guide to Their Public Health Consequences, Monitoring and Management*, 1st ed., Taylor & Francis (1999).
4. W. W. Carmichael, "Health Effects of Toxin-Producing Cyanobacteria: 'The CyanoHABs,'" *Hum. Ecol. Risk Assess. Int. J.* **7**(5), 1393–1407 (2001).
5. D. Anderson, P. Glibert, and J. Burkholder, "Harmful algal blooms and eutrophication: Nutrient sources, composition, and consequences," *Estuaries* **25**(4B), 704–726 (2002).
6. E. Gantt, "Phycobilisomes: light-harvesting pigment complexes," *Bioscience* **25**(12), 781–788 (1975).
7. L. Barsanti and P. Gualtieri, *Algae: Anatomy, Biochemistry, and Biotechnology*, 1st ed., CRC Press (2005).
8. G. Benazzi, "Micro fluidic cytometry for analysis of marine microorganisms," PhD Thesis, School of Electronics and Computer Science, University of Southampton (2010).
9. C. S. French et al., "Fluorescence-Spectrum Curves of Chlorophylls, Pheophytins, Phycoerythrins, Phycocyanins and Hypericin.," *Plant Physiol.* **31**(5), 369–374 (1956).
10. V. T. Oi, A. N. Glazer, and L. Stryer, "Fluorescent phycobiliprotein conjugates for analyses of cells and molecules," *J. Cell Biol.* **93**(3), 981–986 (1982).
11. I. R. F. Ingrid Chorus, "Health risks caused by freshwater cyanobacteria in recreational waters," *J. Toxicol. Environ. Health Part B* **3**(4), 323–347 (2000).
12. E. Funari and E. Testai, "Human health risk assessment related to cyanotoxins exposure.," *Crit. Rev. Toxicol.* **38**(2), 97–125 (2008).
13. D. R. de Figueiredo et al., "Microcystin-producing blooms—a serious global public health issue," *Ecotoxicol. Environ. Saf.* **59**(2), 151–163 (2004).
14. K. Sellner, G. Doucette, and G. Kirkpatrick, "Harmful algal blooms: causes, impacts and detection," *J. Ind. Microbiol. Biotechnol.* **30**(7), 383–406 (2003).
15. European Parliament, "Directive 2006/7/EC of the European Parliament and of the Council of 15 February 2006 concerning the management of bathing water quality and repealing Directive 76/160/EEC," *Off. J. Eur. Union* **49**(37) (2006).
16. J. T. Carlton and J. B. Geller, "Ecological roulette - the global transport of nonindigenous marine organisms," *Science* **261**(5117), 78–82 (1993).

17. P. Hoagland and S. Scatasta, "The Economic Effects of Harmful Algal Blooms," in *Ecol. Harmful Algae*, P. D. E. Granéli and P. D. J. T. Turner, Eds., pp. 391–402, Springer Berlin Heidelberg (2006).
18. Center for Sponsored Coastal Ocean Research, "Economic Impacts of Harmful Algal Blooms (HABs)," U.S. National Ocean and Atmospheric Administration.
19. Y. Tan, J. Jin, and A. Zhou, "Economic Impacts of Harmful Algal Blooms in China," in *ICBBE 2011 5th Int. Conf. Bioinforma. Biomed. Eng.*, pp. 1–5 (2011).
20. "National Lakes Assessment Data," United States Environmental Protection Agency (2007).
21. "Algal Bloom Dynamics," Northwest Fisheries Science Center, National Oceanographic and Atmospheric Administration.  
[http://www.nwfsc.noaa.gov/hab/habs\\_toxins/phytoplankton/algal\\_dynamics.html](http://www.nwfsc.noaa.gov/hab/habs_toxins/phytoplankton/algal_dynamics.html).
22. Grace Analytical Lab, "LMMB023: Standard Operating Procedure for Phytoplankton Sample Collection and Preservation," in *Lake Mich. Mass Balance Methods Compend.* **1(4)**, US Environmental Protection Agency (1997).
23. S. U. Thiel, R. J. Wiltshire, and L. J. Davies, "Automated object recognition of blue-green algae for measuring water quality—A preliminary study," *Water Res.* **29(10)**, 2398–2404 (1995).
24. J. L. Pech-Pacheco and J. Alvarez-Borrego, "Optical-digital system applied to the identification of five phytoplankton species," *Mar. Biol.* **132(3)**, 357–365 (1998).
25. Q. Hu and C. Davis, "Accurate automatic quantification of taxa-specific plankton abundance using dual classification with correction," *Mar. Ecol. Prog. Ser.* **306**, 51–61 (2006).
26. K. V. Embleton, C. E. Gibson, and S. I. Heaney, "Automated counting of phytoplankton by pattern recognition: a comparison with a manual counting method," *J. Plankton Res.* **25(6)**, 669–681 (2003).
27. C. M. Yentsch et al., "Flow Cytometry and Cell Sorting: A Technique for Analysis and Sorting of Aquatic Particles," *Limnol. Oceanogr.* **28(6)**, 1275–1280 (1983).
28. T. P. A. Rutten, B. Sandee, and A. R. T. Hofman, "Phytoplankton monitoring by high performance flow cytometry: a successful approach?," *Cytom. Part J. Int. Soc. Anal. Cytol.* **64(1)**, 16–26 (2005).
29. L. Boddy et al., "Identification of 72 phytoplankton species by radial basis function neural network analysis of flow cytometric data," *Mar. Ecol. Prog. Ser.* **195**, 47–59 (2000).
30. A. Cunningham, "A low-cost, portable flow cytometer specifically designed for phytoplankton analysis," *J. Plankton Res.* **12(1)**, 149–160 (1990).
31. J. C. H. Peeters et al., "Optical plankton analyser: A flow cytometer for plankton analysis, I: Design considerations," *Cytometry* **10(5)**, 522–528 (1989).

32. G. B. J. Dubelaar et al., "Optical plankton analyser: A flow cytometer for plankton analysis, II: Specifications," *Cytometry* **10**(5), 529–539 (1989).
33. H. W. Balfourt et al., "Automatic identification of algae: neural network analysis of flow cytometric data," *J. Plankton Res.* **14**(4), 575–589 (1992).
34. J. W. Hofstraat et al., "Flow cytometric discrimination of phytoplankton classes by fluorescence emission and excitation properties," *J. Fluoresc.* **1**(4), 249–265 (1991).
35. S. K. Brahma et al., "A Resonance Raman Method for the Rapid Detection and Identification of Algae in Water," *Appl. Spectrosc.* **37**(1), 55–58 (1983).
36. Q. Wu et al., "Differentiation of Algae Clones on the Basis of Resonance Raman Spectra Excited by Visible Light," *Anal Chem* **70**(9), 1782–1787 (1998).
37. O. Samek et al., "Raman Microspectroscopy of Individual Algal Cells: Sensing Unsaturation of Storage Lipids in vivo," *Sensors* **10**(9), 8635–8651 (2010).
38. Y. Y. Huang et al., "Micro-Raman spectroscopy of algae: Composition analysis and fluorescence background behavior," *Biotechnol. Bioeng.* **105**(5), 889–898 (2010).
39. S. Vardy and P. Uwins, "Fourier Transform Infrared Microspectroscopy as a Tool to Differentiate *Nitzschia closterium* and *Nitzschia longissima*," *Appl. Spectrosc.* **56**(12), 1545–1548 (2002).
40. M. Kansiz et al., "Fourier Transform Infrared microspectroscopy and chemometrics as a tool for the discrimination of cyanobacterial strains," *Phytochemistry* **52**(3), 407–417 (1999).
41. D. Stramski, A. Bricaud, and A. Morel, "Modeling the Inherent Optical Properties of the Ocean Based on the Detailed Composition of the Planktonic Community," *Appl. Opt.* **40**(18), 2929–2945 (2001).
42. N. MODIS (Moderate Resolution Imaging Spectroradiometer), "Ocean Color Image Gallery."
43. T. Kutser et al., "Monitoring cyanobacterial blooms by satellite remote sensing," *Estuar. Coast. Shelf Sci.* **67**(1–2), 303–312 (2006).
44. P. D. Hunter et al., "Spectral discrimination of phytoplankton colour groups: The effect of suspended particulate matter and sensor spectral resolution," *Remote Sens. Environ.* **112**(4), 1527–1544 (2008).
45. G. M. Whitesides, "The origins and the future of microfluidics," *Nature* **442**(7101), 368–373 (2006).
46. D. Psaltis, S. R. Quake, and C. Yang, "Developing optofluidic technology through the fusion of microfluidics and optics," *Nature* **442**(7101), 381–386 (2006).
47. J. El-Ali, P. K. Sorger, and K. F. Jensen, "Cells on chips," *Nature* **442**(7101), 403–411 (2006).
48. J. Godin et al., "Microfluidics and photonics for Bio-System-on-a-Chip: a review of advancements in technology towards a microfluidic flow cytometry chip," *J. Biophotonics* **1**(5), 355–376 (2008).

49. P. Abgrall and A.-M. Gué, “Lab-on-chip technologies: making a microfluidic network and coupling it into a complete microsystem—a review,” *J. Micromechanics Microengineering* **17**(5), R15–R49 (2007).
50. D. Mark et al., “Microfluidic lab-on-a-chip platforms: requirements, characteristics and applications,” *Chem Soc Rev* **39**(3), 1153–1182.
51. C. Durrieu and C. Tran-Minh, “Optical Algal Biosensor using Alkaline Phosphatase for Determination of Heavy Metals,” *Ecotoxicol. Environ. Saf.* **51**(3), 206–209 (2002).
52. C. Chouteau et al., “Development of novel conductometric biosensors based on immobilised whole cell *Chlorella vulgaris* microalgae,” *Biosens. Bioelectron.* **19**(9), 1089–1096 (2004).
53. H. Guedri and C. Durrieu, “A self-assembled monolayers based conductometric algal whole cell biosensor for water monitoring,” *Microchim. Acta* **163**(3-4), 179–184 (2008).
54. R. E. Ionescu et al., “Amperometric Algal *Chlorella vulgaris* Cell Biosensors Based on Alginate and Polypyrrole-Alginate Gels,” *Electroanalysis* **18**(11), 1041–1046 (2006).
55. M. Chiao, K. B. Lam, and L. Lin, “Micromachined microbial and photosynthetic fuel cells,” *J. Micromechanics Microengineering* **16**(12), 2547–2553 (2006).
56. N. Samsonoff, M. D. Ooms, and D. Sinton, “A photosynthetic-plasmonic-voltaic cell: Excitation of photosynthetic bacteria and current collection through a plasmonic substrate,” *Appl. Phys. Lett.* **104**(4), 043704 (2014).
57. M. D. Ooms, L. Bajin, and D. Sinton, “Culturing photosynthetic bacteria through surface plasmon resonance,” *Appl. Phys. Lett.* **101**(25), 253701 (2012).
58. E. E. Jung et al., “Slab waveguide photobioreactors for microalgae based biofuel production,” *Lab. Chip* (2012).
59. S. C. Pierobon, M. D. Ooms, and D. Sinton, “Evanescent cultivation of photosynthetic bacteria on thin waveguides,” *J. Micromechanics Microengineering* **24**(4), 045017 (2014).
60. S. H. Au, S. C. C. Shih, and A. R. Wheeler, “Integrated microbioreactor for culture and analysis of bacteria, algae and yeast,” *Biomed. Microdevices* **13**(1), 41–50 (2011).
61. D. Kürsten et al., “Cultivation of *Chlorella vulgaris* in microfluid segments and microtoxicological determination of their sensitivity against CuCl<sub>2</sub> in the nanoliter range,” *Eng. Life Sci.* **11**(6), 580–587 (2011).
62. X. Cui et al., “Lensless high-resolution on-chip optofluidic microscopes for *Caenorhabditis elegans* and cell imaging,” *Proc. Natl. Acad. Sci.* **105**(31), 10670–10675 (2008).
63. B. R. Lutz, J. Chen, and D. T. Schwartz, “Hydrodynamic tweezers: 1. Noncontact trapping of single cells using steady streaming microeddies RID A-2101-2011,” *Anal. Chem.* **78**(15), 5429–5435 (2006).
64. C. Wu et al., “Ultrasonication on a microfluidic chip to lyse single and multiple *Pseudo-nitzschia* for marine biotoxin analysis,” *Biotechnol. J.* **6**(2), 150–155 (2011).

65. M.-N. Tsaloglou et al., “On-chip real-time nucleic acid sequence-based amplification for RNA detection and amplification,” *Anal. Methods* **3**(9), 2127–2133 (2011).
66. G. Benazzi et al., “Discrimination and analysis of phytoplankton using a microfluidic cytometer,” *IET Nanobiotechnol.* **1**, 94 (2007).
67. L. Matioli Machado et al., “Microfluidic biochip for phytoplankton cell counting,” in *2013 Symp. Microelectron. Technol. Devices SBMicro*, pp. 1–4 (2013).
68. N. Hashemi et al., “Optofluidic characterization of marine algae using a microflow cytometer,” *Biomicrofluidics* **5**(3), 032009–032009 – 9 (2011).
69. N. Hashemi et al., “Microflow Cytometer for optical analysis of phytoplankton,” *Biosens. Bioelectron.* **26**(11), 4263–4269 (2011).
70. K. M. Davis et al., “Writing waveguides in glass with a femtosecond laser,” *Opt. Lett.* **21**(21), 1729–1731 (1996).
71. A. Marcinkevicius et al., “Femtosecond laser-assisted three-dimensional microfabrication in silica,” *Opt. Lett.* **26**(5), 277–279 (2001).
72. Y. Liao et al., “Rapid prototyping of three-dimensional microfluidic mixers in glass by femtosecond laser direct writing,” *Lab. Chip* **12**(4), 746–749 (2012).
73. V. Tielen and Y. Bellouard, “Three-Dimensional Glass Monolithic Micro-Flexure Fabricated by Femtosecond Laser Exposure and Chemical Etching,” *Micromachines* **5**(3), 697–710 (2014).
74. G. G. Melpignano, A. Schaap, and Y. Bellouard, “Design and Fabrication of a Prototype Actuator for Fourier Transform Interferometry,” in *Prog. Optomechatronic Technol.*, R. Tutsch et al., Eds., pp. 97–105, Springer International Publishing (2014).
75. A. Schaap and Y. Bellouard, “Molding topologically-complex 3D polymer microstructures from femtosecond laser machined glass,” *Opt. Mater. Express* **3**(9), 1428–1437 (2013).
76. M. Kim et al., “Single cell detection using a glass-based optofluidic device fabricated by femtosecond laser pulses,” *Lab. Chip* **9**(2), 311 (2009).
77. A. Crespi et al., “Three-dimensional Mach-Zehnder interferometer in a microfluidic chip for spatially-resolved label-free detection,” *Lab. Chip* **10**(9), 1167–1173 (2010).
78. Y. Hanada et al., “Nano-aquarium for dynamic observation of living cells fabricated by femtosecond laser direct writing of photostructurable glass,” *Biomed. Microdevices* **10**(3), 403–410 (2008).
79. Y. Bellouard et al., “Towards a femtosecond laser micro-machined optofluidic device for distinguishing algae species,” in *Proc. SPIE* **7203** (2009).
80. Scandinavian Culture Collection of Algae & Protozoa, Z8, <http://www.sccap.dk/media/freshwater/7.asp>.

81. E. Marquis, N. Niquil, and C. Dupuy, "Does the study of microzooplankton community size structure effectively define their dynamics? Investigation in the Bay of Biscay (France)," *J. Plankton Res.* **33**(7), 1104–1118 (2011).
82. A. Morel and A. Bricaud, "Theoretical results concerning light absorption in a discrete medium, and application to specific absorption of phytoplankton," *Deep Sea Res. Part Oceanogr. Res. Pap.* **28**(11), 1375–1393 (1981).
83. A. Quirantes and S. Bernard, "Light scattering by marine algae: two-layer spherical and nonspherical models," *J. Quant. Spectrosc. Radiat. Transf.* **89**(1-4), 311–321 (2004).
84. A. K. Jain, R. P. . Duin, and J. Mao, "Statistical pattern recognition: a review," *IEEE Trans. Pattern Anal. Mach. Intell.* **22**(1), 4–37 (2000).
85. P. C. Mahalanobis, "On the generalised distance in statistics," *Proc. Natl. Inst. Sci. India* **2**(1), 49–55 (1936).
86. E. Garcia-Breijo et al., "A comparison study of pattern recognition algorithms implemented on a microcontroller for use in an electronic tongue for monitoring drinking waters," *Sens. Actuators Phys.* (2011).
87. G. Reibnegger et al., "Neural networks as a tool for utilizing laboratory information: comparison with linear discriminant analysis and with classification and regression trees," *Proc. Natl. Acad. Sci.* **88**(24), 11426–11430 (1991).
88. J. A. Sánchez Mesa, C. Galán, and C. Hervás, "The use of discriminant analysis and neural networks to forecast the severity of the Poaceae pollen season in a region with a typical Mediterranean climate," *Int. J. Biometeorol.* **49**(6), 355–362 (2005).
89. J. D. Olden and D. A. Jackson, "A comparison of statistical approaches for modelling fish species distributions," *Freshw. Biol.* **47**(10), 1976–1995 (2002).
90. C. S. Reynolds et al., "Towards a functional classification of the freshwater phytoplankton," *J. Plankton Res.* **24**(5), 417–428 (2002).
91. C. Kruk et al., "A morphological classification capturing functional variation in phytoplankton," *Freshw. Biol.* **55**(3), 614–627 (2010).
92. C. Kruk et al., "Phytoplankton community composition can be predicted best in terms of morphological groups," *Limnol. Oceanogr.* **56**(1), 110–118 (2011).
93. J. Padišák, L. O. Crossetti, and L. Naselli-Flores, "Use and misuse in the application of the phytoplankton functional classification: a critical review with updates," *Hydrobiologia* **621**(1), 1–19 (2009).
94. L. Naselli-Flores, J. Padišák, and M. Albay, "Shape and size in phytoplankton ecology: do they matter?," *Hydrobiologia* **578**(1), 157–161 (2007).
95. M. Huete-Ortega et al., "General patterns in the size scaling of phytoplankton abundance in coastal waters during a 10-year time series," *J. Plankton Res.* **32**(1), 1–14 (2010).
96. P. Cermeno and F. G. Figueiras, "Species richness and cell-size distribution: size structure of phytoplankton communities," *Mar. Ecol. Prog. Ser.* **357**, 79–85 (2008).

97. C. Kaiblinger et al., "Photosynthetic efficiency as a function of thermal stratification and phytoplankton size structure in an oligotrophic alpine lake," *Hydrobiologia* **578**(1), 29–36 (2007).
98. M. E. Baird and I. M. Suthers, "A size-resolved pelagic ecosystem model," *Ecol. Model.* **203**(3–4), 185–203 (2007).
99. K. S. Lee et al., "Assessment of cross-type optical particle separation system," *Microfluid. Nanofluidics* **13**(1), 9–17 (2012).
100. C. Helmbrecht, R. Niessner, and C. Haisch, "Photophoretic Velocimetry for Colloid Characterization and Separation in a Cross-Flow Setup," *Anal. Chem.* **79**(18), 7097–7103 (2007).
101. J.-P. Matas, J. F. Morris, and É. Guazzelli, "Lateral force on a rigid sphere in large-inertia laminar pipe flow," *J. Fluid Mech.* **621**, 59–67 (2009).
102. D. Di Carlo et al., "Continuous inertial focusing, ordering, and separation of particles in microchannels," *Proc. Natl. Acad. Sci. U. S. A.* **104**(48), 18892–18897 (2007).
103. S. A. Berger, L. Talbot, and L. S. Yao, "Flow in Curved Pipes," *Annu. Rev. Fluid Mech.* **15**(1), 461–512 (1983).
104. D. Di Carlo et al., "Equilibrium Separation and Filtration of Particles Using Differential Inertial Focusing," *Anal. Chem.* **80**(6), 2204–2211 (2008).
105. S. C. Hur et al., "Deformability-based cell classification and enrichment using inertial microfluidics," *Lab. Chip* **11**(5), 912–920 (2011).
106. M. Masaeli et al., "Continuous Inertial Focusing and Separation of Particles by Shape," *Phys. Rev. X* **2**(3), 031017 (2012).
107. A. A. S. Bhagat, S. S. Kuntaegowdanahalli, and I. Papautsky, "Continuous particle separation in spiral microchannels using dean flows and differential migration," *Lab. Chip* **8**(11), 1906–1914 (2008).
108. S. S. Kuntaegowdanahalli et al., "Inertial microfluidics for continuous particle separation in spiral microchannels," *Lab. Chip* **9**(20), 2973–2980 (2009).
109. N. Nivedita and I. Papautsky, "Continuous separation of blood cells in spiral microfluidic devices," *Biomicrofluidics* **7**(5), 054101 (2013).
110. C. Helmbrecht, R. Niessner, and C. Haisch, "Photophoretic velocimetry--a new way for the in situ determination of particle size distribution and refractive index of hydrocolloids," *The Analyst* **136**(9), 1987–1994 (2011).
111. R. W. Applegate et al., "Fiber-focused diode bar optical trapping for microfluidic flow manipulation," *Appl. Phys. Lett.* **92**(1), 013904–013904–3 (2008).
112. R. W. Applegate Jr. et al., "Particle size limits when using optical trapping and deflection of particles for sorting using diode laser bars," *Opt. Express* **17**(19), 16731–16738 (2009).
113. F. M. White, *Viscous fluid flow*, McGraw-Hill Higher Education, New York, NY (2006).



114. G. K. Batchelor, *An Introduction to Fluid Dynamics*, Cambridge University Press, Cambridge (2000).
115. A. Ashkin, "Forces of a single-beam gradient laser trap on a dielectric sphere in the ray optics regime," *Biophys. J.* **61**(2), 569–582 (1992).
116. E. Lee, R.-L. Heng, and L. Pilon, "Spectral optical properties of selected photosynthetic microalgae producing biofuels," *J. Quant. Spectrosc. Radiat. Transf.* **114**, 122–135 (2013).
117. A. Morel and A. Bricaud, "Inherent optical properties of algal cells, including picoplankton. Theoretical and experimental results," *Can. Bull. Fish. Aquat. Sci.* **214**, 521–229 (1986).
118. J. S. Erickson et al., "In Situ Phytoplankton Analysis: There's Plenty of Room at the Bottom," *Anal. Chem.* **84**(2), 839–850 (2012).

# Summary

The dynamics of algae species – the amount and concentrations of the species in a body of water – vary in response to changing environmental conditions. Factors such as temperature, light conditions, and intentional or unintentional interventions by humans can all affect the species dynamics, which makes algae a useful biomarker for changes occurring in the water. Monitoring the species dynamics can help identify and understand harmful algae blooms (HABs), which cost the European Union an estimated €600 million/year. These blooms can destroy aquaculture, and are particularly harmful if they consist of toxin-producing algae. The sampling and identification of algae in water are also required for ballast water monitoring and regulatory compliance. Despite all these application areas, the methods for monitoring algae are expensive and slow, which is the motivation for the work in this thesis.

This thesis presents lab-on-a-chip technologies designed to address this problem. The combination of optics and microfluidics on a single device creates a powerful and robust approach to algae species classification. The heart of the technology is a glass microchip fabricated with a femtosecond laser. This fabrication technique allows for the creation of a microchannel and a buried curved waveguide in a single piece of glass. A laser and photodetector respectively provide and detect light that is transmitted across the microchannel as water with algae is flown through the device. The photodetector signals are processed with a neural network, which is trained to do pattern recognition on algae samples. After an optimization of the neural network, it was capable of correctly identifying the species of ~90% of the algae cells in a mixture of five different species.

For implementation in a field-deployable device, issues of channel clogging and pre-sorting of the sample by size of cell must be addressed. To this end, we explore the use of both optical and fluidic forces for passive size-sorting. The first method relies on the gradient optical forces from a high aspect ratio laser bar diode, which causes entrained particles to cross the streamlines of the flow. With a combination of simulations and experiments we demonstrate that this approach is feasible and size-sensitive. The second method, using high flow rates in a spiral-shaped channel, relies on inertial forces and secondary flows to sort the particles by shape and size. Both microspheres and algae could be sorted with this method, with separation efficiencies of 96% (spheres) and 77% (algae). A major point of comparison between these

techniques is the throughput rate: the fluidic technique worked successfully with flow velocities several orders of magnitude higher than those used in the optical setup. The optical approach can perform more complex and flexible sorting tasks, but for the relatively low-complexity sorting done here, the inertial fluidic system is more appropriate for a field-deployable device.

In summary, the technology presented in this thesis provides a set of tools which, combined, can pre-sort algae cells by size and shape and classify the species with a powerful and adaptable analytical method.

# Samenvatting

De dynamica van algensoorten – de hoeveelheid en concentratie van soorten in een waterlichaam – varieert met de veranderende omstandigheden in de omgeving. Factoren als temperatuur, lichtomstandigheden, en opzettelijk of onopzettelijk menselijk gedrag kunnen de dynamica van algensoorten beïnvloeden. Algen zijn daarom een nuttige biomarker voor de veranderingen in een waterlichaam. Het monitoren van de populatiedynamica kan helpen om het ontstaan van schadelijke algenbloeien, die de Europese Unie een geschatte €600 miljoen per jaar kosten, te identificeren en te begrijpen. Deze bloeien kunnen de aquacultuur verwoesten en ze zijn vooral schadelijk als ze uit soorten bestaan die toxisch zijn. Ook voor het monitoren van ballastwater en het naleven van regelgeving zijn het bemonsteren en identificeren van algen in water verplicht. Ondanks deze vele toepassingen zijn de bestaande methoden voor het monitoren van algen duur en langzaam; dit is de motivatie van dit werk.

Dit proefschrift presenteert *lab-on-a-chip*-technologie die ontworpen is om dit probleem aan te pakken. De combinatie van optica en microfluidica in één apparaat leidt tot een krachtige en robuuste methode om algensoorten te identificeren. Het hart van de technologie wordt gevormd door een glazen microchip, gefabriceerd door een femtoseconde-laser. Met deze techniek kunnen, in één stuk glas, zowel een vloeistofkanaaltje als een gekromde lichtgeleider in dezelfde processtap worden gemaakt. Een laser produceert licht dat door de lichtgeleider naar het kanaaltje wordt geleid; het licht kruist het kanaaltje waarin water stroomt dat algen bevat, en daarna valt het licht op een fotodetector. De signalen van de fotodetector worden geanalyseerd door een neurale netwerk dat is getraind op patroonherkenning. Na een optimalisatie van het neurale netwerk konden 90% van de algen in een mengsel van 5 soorten correct worden geïdentificeerd.

Om dit alles in een draagbaar en praktisch inzetbaar apparaat uit te kunnen voeren, moeten problemen van het verstopping van kanalen en het voorsorteren van algen worden opgelost. Daarom hebben we de mogelijkheid onderzocht om optische of vloeistofkrachten te gebruiken voor het automatisch scheiden en sorteren van de algen. De eerste methode gebruikt de krachten die worden veroorzaakt door een optische gradiënt, om deeltjes of cellen te verplaatsen loodrecht op de stroomlijnen. Door middel van een combinatie van simulaties en experimenten hebben we aangetoond we aan dat deze benadering haalbaar is, en gevoelig is voor de afmeting

van de algen zodat de methode gebruikt kan worden om algen te scheiden en sorteren. In de tweede methode, die gebruik maakt van hoge vloeistofsnelheden in een spiraalvormig kanaal, worden de deeltjes gesorteerd op grootte en vorm door traagheidskrachten en secundaire vloeistofstromingen. Zowel micro-deeltjes als algen konden met deze methode gesorteerd worden, met scheidingsrendement van 96% (micro-deeltjes) en 77% (algen). Een belangrijk verschil tussen deze twee technieken is de doorvoersnelheid: de fluidische techniek werkt met vloeistofsnelheden die ordes van grootte hoger zijn dan die van de optische methode. De laatste methode kan wel complexere en flexibelere sorteertaken uitvoeren, maar in verband met de relatieve lage complexiteit van de toepassing is het op traagheid gebaseerde fluidische systeem geschikter voor implementatie in een draagbaar apparaat.

Samenvattend, bieden de in dit proefschrift gepresenteerde technieken gereedschappen die het, samen genomen, mogelijk maken om algen te sorteren op grootte en vorm, en waarmee verschillende algensoorten kunnen worden geclassificeerd door middel van een krachtige en flexibele analysemethode.

# Acknowledgements

First and foremost I would like to thank my supervisor, Yves Bellouard, who started this project, hired me, and provided advice throughout. Yves, your enthusiasm for doing hands-on work in the lab was always an inspiration. I really benefited from the big-picture thinking you brought to the project, along with your expertise and insights into optics, systems, materials, and many other fields. I appreciate how much you went out of your way to provide helpful advice not only on the research but also on things like career planning and intercultural experiences. Your generosity in giving me space to work and freedom to try new ideas made my PhD an enjoyable and valuable experience.

I would also like to express my appreciation of Jaap den Toonder, who “inherited” our previous research group and enthusiastically adopted us into his new Microsystems group. Jaap, the expertise you provided in microfluidics, your organization and attention to detail, and your willingness to help out whenever I asked were all invaluable. Thank you for making all the “old” students feel so at home in your new group and for being so willing listen to suggestions and ideas; I wish you all the best with the growing Microsystems group and the new lab!

I would like to also thank all of the members of my thesis committee for their time, feedback, and comments on this thesis. Thank you in particular to those who had to travel to Eindhoven for the defense. In particular, my thanks to Thomas Rohrlack who offered his expertise on algae throughout this project, and who provided many of the algae samples used in this work.

The Microsystems group (and the MNSE group before that) has been a fun and supportive environment in which to undertake this work. To the past and current grad students and postdocs in the group, I thank you for all the lunchtime discussions, the social events, the collaborations in the lab, the insightful questions during group meetings, and all that I have learned from you over the years. I also thank the group’s secretary Liesbeth van Ballegooij, who knows the ins and outs of every aspect of the university, and the lab manager Willie ter Elst, for the support and know-how they provided.

Lastly, to all my friends and family, thank you for your support, encouragement, and interest over the past years, and for indulging my new enthusiasm for algae!

# List of publications

**The work described in this thesis has resulted in the following publications:**

## Journal articles

A. Schaap & J. Dumon, "Sorting of algae cells by morphology in spiral microchannels using inertial microfluidics", *to be submitted*

A. Schaap, T. Rohrlack, and Y. Bellouard, "Lab on a chip technologies for algae detection: a review," *Journal of Biophotonics* **5**(8-9), 661–672 (2012).

A. Schaap, T. Rohrlack, and Y. Bellouard, "Optical classification of algae species with a glass lab-on-a-chip," *Lab. Chip* **12**(8), 1527–1532 (2012).

A. Schaap, Y. Bellouard, and T. Rohrlack, "Optofluidic lab-on-a-chip for rapid algae population screening," *Biomed. Opt. Express* **2**(3), 658–664 (2011).

## Conference presentations with published proceedings

A. Schaap, T. Rohrlack, and Y. Bellouard, "Optofluidic microdevice for algae classification: a comparison of results from discriminant analysis and neural network pattern recognition," in *Proceedings of SPIE* **8251** (2012).

## Invited talks

"Making integrated 3D microsystems with femtosecond lasers", *Mechanical Engineering Departmental Seminar, Boston University* (2014).

"An optofluidic glass microchip for phytoplankton sizing and identification", *Microfluidics and Microsensor Technology for Oceanography and Environmental Science Applications*. Southampton, UK (2013).

**The author has also contributed to the following publications which are outside of the scope of this thesis:**

## Journal articles

A. Schaap and Y. Bellouard, "Molding topologically-complex 3D polymer microstructures from femtosecond laser machined glass," *Opt. Mater. Express* **3**(9), 1428–1437 (2013).

A. Schaap, W. C. Chu, and B. Stoeber, "Transport of airborne particles in straight and curved microchannels," *Physics of Fluids* **24**(8), 083301 (2012).

S. Dutz et al., "A microfluidic spiral for size-dependent fractionation of magnetic microspheres," *Journal of Magnetism and Magnetic Materials* **324**(22), 3791–3798 (2012).

A. M. Schaap, W. C. Chu, and B. Stoeber, "Continuous Size-Separation of Airborne Particles in a Microchannel for Aerosol Monitoring," *IEEE Sensors Journal* **11**(11), 2790–2797 (2011).

Conference presentations with published proceedings

A. Schaap, W.C. Chu, M.I. Antonio, B. Stoeber, "Microchannel-based size detector for airborne particles," *IEEE Sensors Conference*, 2441–2446 (2010).

Patent

W.C. Chu, B. Stoeber, A. Schaap, "Methods and apparatus for detecting particles entrained in fluids", U.S. Application # 13/882,092, submitted 04-26-2013.



## About the author

Allison Schaap was born on September 21, 1984, in New Westminster, Canada. In 2008 she completed her bachelors degree in Engineering Physics at the University of British Columbia (Vancouver, Canada). In 2010 she received her masters degree in Mechanical Engineering from the same university. Her masters research took place in the group of Dr. Boris Stoeber where she was funded by a fellowship from the British Columbia Innovation Council. Her thesis, entitled “Transport and size-separation of airborne particles in a microchannel for continuous particle monitoring,” was a collaboration between the Mechanical Engineering and Environmental Health departments.

In November 2010 she started a PhD project under the supervision of Dr. Yves Bellouard at the Eindhoven University of Technology (the Netherlands), the results of which are presented in this dissertation. During her PhD, Allison received Best Student Oral Presentation awards at two conferences, was an invited speaker at two international venues, and received a Phase 1 Valorisation Grant from the funding agency STW.

